Modeling and Attenuation of Motion Artifacts in Capacitive ECG

Vinicius Grando Sirtoli

A Thesis
In the Department of
Electrical and Computer Engineering

Presented in Partial Fulfillment of the Requirements
For the Degree of
Doctor of Philosophy (Electrical & Computer Engineering)
at Concordia University
Montreal, Quebec, Canada

March 2024

Concordia University
School of Graduate Studies

This is to certify that the dissertation prepared

By: **Vinicius Grando Sirtoli**

Entitled: **Modeling and Attenuation of Motion Artifacts in Capacitive ECG**

and submitted in partial fulfillment of the requirements for the degree of

Doctor of Philosophy (Electrical & Computer Engineering)

complies with the regulations of this University and meets the accepted standards with respect to originality and quality.

Signed by the final examining committee:

_____ Chair
Dr. Todd Eavis

_____ External Examiner
Dr. Shahriar Mirabbasi

_____ External to Program
Dr. Gordon Roberts

_____ Examiner
Dr. Chunyan Wang

_____ Examiner
Dr. Yousef R. Shayan

_____ Co-Supervisor
Dr. Ghyslain Gagnon

_____ Supervisor
Dr. Glenn Cowan

Approved by _____
Dr. Y. R. Shayan, Chair
Department of Electrical and Computer Engineering

March 28, 2024

_____
Dr. Mourad Debbabi, Ph.D., P.Eng., Dean
Faculty of Engineering and Computer Science

Abstract

Modeling and Attenuation of Motion Artifacts in Capacitive ECG

Vinicius Grando Sirtoli, Ph.D.
Concordia University, 2024

To reduce the burden on the health system and democratize access to health care, current research is aimed at embedding medical devices in daily-life objects with autonomous diagnostic algorithms. In the case of popular tools such as the electrocardiogram (ECG), electroencephalogram (EEG), and electromyography (EMG), one of the scientific challenges is replacing the standard wet Ag/AgCl electrode. A strong candidate is the capacitive electrode, which can be seamlessly integrated into chairs, beds, car seats and wearable devices. This is a dry and active kind of electrode, fabricated on a rigid or flexible printed circuit board. Although in ideal conditions capacitive electrodes can provide high-quality biopotential measurements, they are prone to motion artifacts (MAs) because they do not stick to the patient's body. A MA is a large interference that can render the ExG analysis impossible. Often, it is much larger than the targeted signal and it can even saturate the analog front-end's input. MAs are often described as random or unpredictable events, however, in this dissertation they were modeled based on triboelectric nanogenerator theory. The proposed model uses information on displacement and speed to mimic the MA behavior. It also supports existing bibliography that MA comprises two main phenomena, a change in electrode capacitance (capacitance between electrode and patient) and generation of triboelectricity. The electrode capacitance variation can cause voltage division with the input capacitance (reduce signal to noise ratio), low cut-off frequency fluctuation (common-mode signals converted into differential artifacts) and modulation of DC voltages across the electrode capacitance (voltage spikes). To attenuate the effects of electrode capacitance variation, three topologies of capacitive electrode are proposed: i) a through-body negative feedback is applied to stabilize the electrode's gain; ii) the input resistance is boosted with a positive feedback so a series capacitance can be inserted; iii) a control system detects the electrode capacitance change and modifies the input resistance.

Acknowledgment

Although a few words will not accurately translate my gratitude, I will try my best to recognize the importance of everyone who helped me make this dream come true. First, I must thank my supervisor Glenn Cowan for changing my life. He believed in me even more than I did, and he gave me opportunities nobody else did. This was only possible because my co-supervisor, Ghyslain Gagnon, also accepted me in his project and allowed me to keep working with what motivates me the most. Honestly, Glenn and Ghyslain are great supervisors, but above all, they are amazing people.

I would like to also thank Concordia University, its staff, students, and professors for the support and knowledge provided. I really loved my time here, what a wonderful environment! A special mention should be given to Tadeusz Obuchowicz (Ted) for all the help provided with Cadence and VLSI design, as well as keeping the rock 'n' roll alive. Christian Guenole was also of fundamental importance, supporting with engineering tools and equipment.

From the many amazing colleagues, I must thank Sami Sattar for partnering in classes and helping me settle into the group, Anatoly Syutkin for the countless hours spent in the office and on the mountains; Laura Morelli for supporting my ideas and helping materialize them, Sara Granata for the immense help to finish my designs and experimentation and Di Zhang for guiding me through the layout and tapeout process.

Dedication

I dedicate this dissertation to my family and friends, especially my grandparents Luiz and Iria, for understanding my decision to study abroad. Dad and Mom, now I recognize the importance of discipline. Gabriel and Daiane, my borrowed-family, thank you for always looking out for me. Luna, Valentina, and Stella, thanks for endless joy and embarking in this adventure with me. Yet, this journey started more than a decade ago and would not have been completed without the person who gave a rebellious boy direction and purpose, my best friend and wife, Mariana.

Contents

List of Figures

List of Tables

List of Abbreviations

- CVD - Cardiovascular Disease
- WHO - World Health Organization
- AHA - American Heart Association
- ECG - Electrocardiogram
- ADC - Analog-to-Digital Converter
- cECG - Capacitive Electrocardiogram
- PCB - Printed Circuit Board
- MA - Motion Artifact
- TENG - Triboelectric Nanogenerator
- AFE - Analog Front-End
- NIC - Negative Impedance Converter
- TECD - Triboelectric Charge Density
- CMRR - Common-mode rejection ratio
- PSD - Power Spectral Density
- RMS - Root Mean Square
- DRL - Driven Right-Leg
- GUI - Graphical User Interface
- PR - Pseudo-Resistor

- VGA - Variable Gain Amplifier
- HPF - High-Pass Filter
- LPF - Low-Pass Filter
- THD - Total Harmonic Distortion
- Opamp - Operational Amplifier

Chapter 1

Introduction

1.1 The Electrocardiogram

Cardiovascular diseases (CVDs) are the number one cause of death globally according to the World Health Organization (WHO) [1]. The American Heart Association (AHA) estimates that 19 million people died from CVD worldwide in 2020, accounting for 37% of deaths in people less than 70 years old [2]. At the individual level, for prevention of heart attacks and strokes, interventions need to be targeted at those with high cardiovascular risks. Hence, a crucial part of this strategy is the early detection in patients who are at risk due to factors such as hypertension, diabetes and hyperlipidemia [3].

The electrocardiogram (ECG) is one of the most important diagnostic tools in modern medicine [4]. It allows physicians to monitor, in a non-invasive and safe manner, the cardiac activity of people within all age groups. The ECG is widely applied to detect arrhythmia (abnormal heart rhythm), coronary artery disease (damaged/blocked artery), and heart attack [5]. The ECG itself does not provide any treatment to the patient. It is only a way of displaying the heart's health.

The standard ECG measurement requires electrodes connected to the patient's skin, with each being attached to a medical-grade device. The combinations of signals from different electrodes are referred to as leads. The leads can be unipolar or bipolar and are displayed on a monitor for medical interpretation. The 3-lead ECG requires 3 measurement electrodes and one reference electrode, while the 12-lead ECG uses 9 measurement electrodes and a reference one. There are pre-defined positions on the body for each electrode as shown in Fig. 1.1. Thus, the ECG preparation requires a trained professional. The standard clinical ECG uses 12 leads.

Leads I, II and III (or "limb leads") are bipolar. This means that they are obtained by combining the signals from electrodes LA, RA and LL. The electrode RL is used as a

reference and not as a lead. The augmented limb leads are unipolar, and thus they use the signal of one limb electrode and a reference point with zero potential. The precordial/chest leads (V1-V6) are also unipolar and provide assessment of the heart's electrical activity from another plane of view. Having multiple leads aids in identifying/confirming pathologies.

The choice and placement of leads depends on the targeted application [6]. For example, telemetry monitors often use a three-electrodes system, where two are measuring electrodes and one is a reference. The measuring electrodes can be placed on the human body to obtain the leads needed. In this dissertation, the three-electrodes technique is the chosen method due to its simplicity.

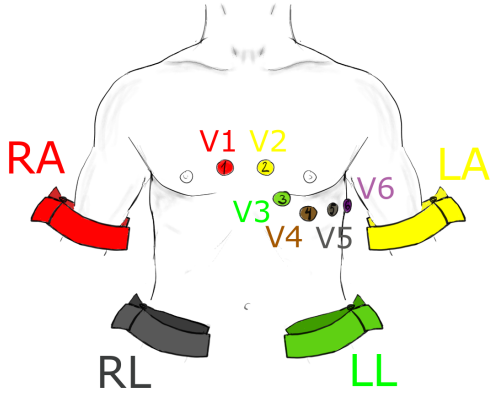

Figure 1.1: Electrode placement for an ECG

An ECG waveform can be seen in Figure 1.2. Different leads will render unique waveforms, but the main characteristics are present in most of them. The shape of the P-wave, QRS-complex, and T-wave are normally the characteristics assessed by physicians when reading an ECG. Each one of the PQRST waves are related to a physical phenomenon occurring during the heartbeat [7]:

- P-wave: This is the first little bump; it is related to the atrial depolarization (atria contraction). It precedes the QRS complex and should keep the same form with time.
- PQ/PR-interval: Time interval from the start of the P-wave to the start of the QRS-complex. It should have a constant duration between heart beats and should align with the baseline.
- QRS-complex: It is the area of the larger peaks, and represents ventricle depolarization. It is measured from the start of the Q-wave to the end of the S-wave. It does not look the same for all leads.

- T-wave: After the QRS-complex, there is a small bump called the T-wave, which is caused by the ventricle's relaxation. It is normally asymmetric, and its height or polarity can indicate pathological findings.
- ST-segment: Delay between depolarization (cells contract) and repolarization (cells relax) of the heart's ventricle. It comprises the region where the S-wave ends and the T-wave starts. It should be flat and overlapping with the baseline. An abnormal ST-segment is common indicator of diseases.
- QT-interval: It accounts for the time interval from the start of the QRS-complex to the end of the T-wave. It represents the time needed by the ventricle to depolarize and repolarize.

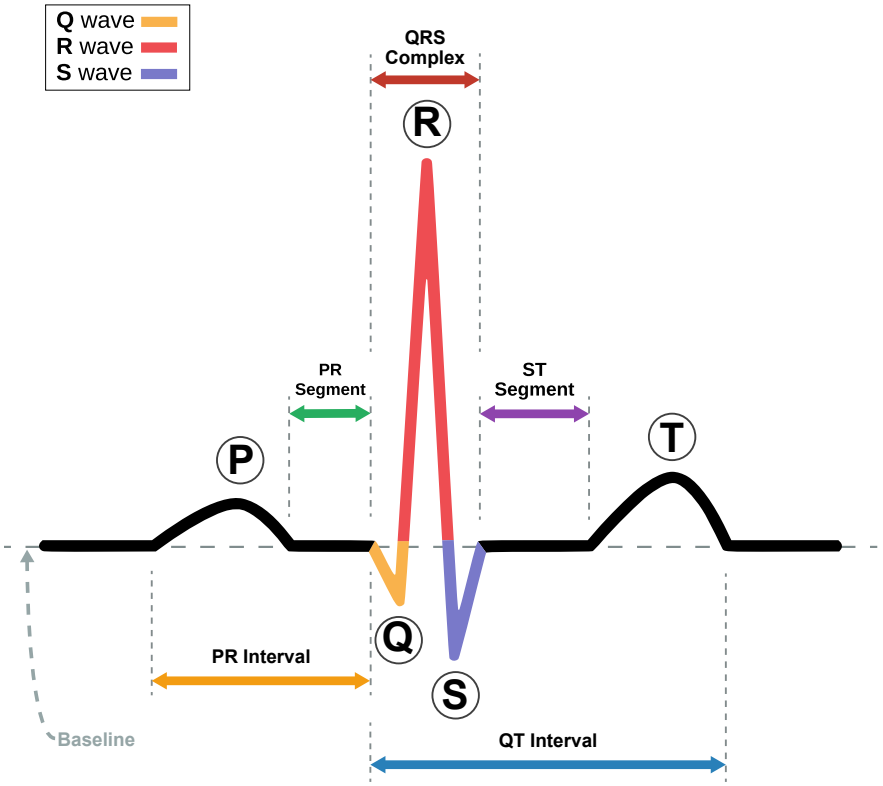

Figure 1.2: Example of an ECG waveform and its main characteristics

From an instrumentation point of view, the measuring device must present high gain and low-noise to cope with the ECG's low amplitude, typically in the order of 1 mV [8]. The bandwidth needed varies from one application to another, yet the low cut-off frequency can

be as low as tenths of mHz and the high cut-off frequency is in the range of hundreds of Hz. A guideline for standardization of the ECG was created by a committee of specialists [9]. Some of their recommendations are:

- A low cut-off frequency of 0.5 Hz is a regular choice because it complies with a minimum heart rate of 30 beats/min and filters out artifacts from respiration. However, this cut-off frequency can introduce distortion on the T-waves and the ST-segment due to phase nonlinearities when amplitude versus frequency response varies abruptly. Therefore, the AHA recommends a low cut-off frequency of 0.05 Hz, although it does not filter breathing artifacts.

- The QRS fundamental frequencies lie between 1 Hz and 30 Hz; and this is the band where distortion should be avoided the most. Thus, a flat gain over this frequency range, a low cut-off frequency of 0.67 Hz and a high cut-off frequency of 150 Hz is usually accepted.

- A high cut-off frequency between 50 Hz and 100 Hz is also accepted by many electrocardiographers, as it allows visual diagnostics of routine recordings. However, most devices aim for cut-off frequencies above 100 Hz.

- If only the R-wave is necessary, such as for heartbeat detection, a high cut-off frequency of 40 Hz is enough [10].

The digitization of the signal is also a matter of concern, yet the current technology easily achieves analog-to-digital converters (ADCs) with 12 or 16 bits of resolution and with sampling frequencies higher than 500 Sa/s.

1.2 Capacitive Electrodes

Telemedicine applications will most likely play a major role in reducing CVD-related mortality. We can therefore expect a tremendous increase in the usage of remote medical applications, with doctors ultimately diagnosing the disease with the help of machine learning algorithms. However, the widespread adoption of telemedicine involves providing patients with sensors that can work remotely, without the assistance of a specially trained technician. A major challenge consists of developing sensors that provide the same degree of confidence as conventional medical-grade instruments.

For instance, many consumer heart rate monitoring sensors, either stand-alone or included in smart devices, are currently being marketed. Although the use of these devices

for sports-related activities or limited medical monitoring has been demonstrated as viable, much remains to be done to produce sensors that offer a reliable, accurate and diagnostically useful ECG signal that can be used for medical purposes. This is especially the case when the designed system must provide the same diagnostic value as a hospital-grade 12-lead system.

Although the conventional Ag/AgCl electrode provides high quality and reliable biopotential readings, it requires the application of an electrically conductive gel, which dries out over long-term monitoring (reducing the signal quality) or leads to discomfort and skin irritation [11]. Moreover, the increased ion conductivity between skin and electrode creates a half-cell potential in wet electrodes (offsets the signal), which does not happen in non-contact electrodes [12]. Therefore, capacitive sensing is increasingly seen as one viable alternative to monitor biopotentials [13]. It allows for the acquisition of cardiac biopotentials using dry electrodes, either in direct contact with the skin or with a layer of air, hair or cloth. It thus gives the option of monitoring patients in the absence of a qualified technician. Further, capacitive sensors can easily be integrated into wearables or objects of daily use such as chairs [14], [15], beds [16], [17] or car seats [18], [19], giving this technology an obvious advantage over conventional wet electrodes. The acquisition of an ECG using capacitive electrodes is commonly referred as capacitive ECG or cECG.

Electrodes can be divided into two categories, passive or active, which relate to the presence or absence of electronic components. The standard wet Ag/AgCl electrode is an example of a passive electrode, yet many other types of passive electrodes have been proposed. However, dry electrodes usually present very high coupling impedance, with capacitances ranging from units of pF to tenths of nF and resistances in the order of GΩ, depending on the insulator material and the existence of air gaps [8]. Active electrodes are used to solve this issue. A commonly reported way of designing active electrodes is to mount an amplifier on the same substrate as the sensing element. This way, the amplifier's high input impedance avoids voltage division with the coupling impedance, while the amplifier's low output impedance protects the signal from picking up noise when driven through cables. Figure 1.3 shows one possible stack-up of a capacitive electrode.

In the example stack-up, four layers are present, where the copper and insulator can be related to a printed circuit board (PCB). The copper represents a conductive sensing area and is the standard conductor used in PCBs. The insulator forces a capacitive interface and can be implemented by the PCB's solder mask. The presence of cloth (e.g. cotton) and air gaps (I-C and C-S gaps in Fig. 1.3) depends on the system and operating conditions. Hence, the skin and copper can be considered as the plates of a parallel plate capacitor, while the other layers act as dielectrics. Strictly speaking, some authors may not consider a system with copper-cloth-skin as capacitive because most fabrics present a significant

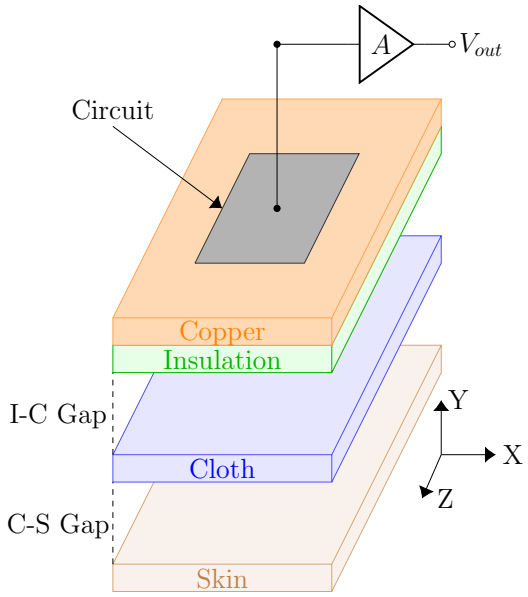

Figure 1.3: Stack-up of a capacitive electrode

resistive component. Therefore, a purely capacitive sensor must have an insulating layer.

1.3 Motion Artifacts

To supply the desired measurement confidence, a major challenge that capacitive sensing has to achieve is the mitigation of motion artifacts (MAs). These artifacts come from the relative motion of the electrode against the skin and impact the quality of the recorded signal. Although MAs impact all types of electrodes, they are more severe in the case of contactless dry electrodes, as these are unattached and more prone to movement [20], [21]. The MA signal can be hundreds of times greater than the proper ECG signal [8] and could saturate the amplifier's input [22]. Additionally, MAs occur in a wide range of frequencies that can overlap with ECG frequencies, thus preventing mitigation through simple filtering techniques.

In practice, MAs can have many causes. For example, they can be related to changes of position on a chair/bed or be caused by breathing. In the case of wearables, MAs can be related to daily activities such as walking, sports-related movements or driving. Regardless of the initial cause, slow and short-reach movements, such as breathing, result in what is known as baseline wander or drift (see Fig. 1.4). In this case, it is possible to distinguish what is typically the most central and visible feature of an ECG, the QRS complex. However, the signal is shifted from the baseline by a low-frequency noise of comparable or higher amplitude than the ECG amplitude itself.

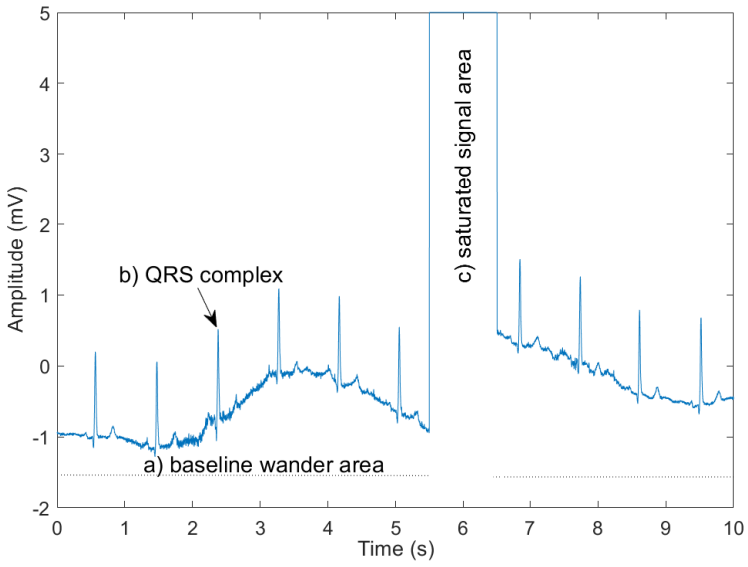

Figure 1.4: Example of a capacitive ECG waveform with artifacts. a) baseline wander causes an elevation of the cECG baseline; b) the QRS complex wave; c) signal is saturated due to a large MA

Larger amplitude movements can saturate the signal and make signal detection impossible, as depicted in region c) of Fig. 1.4. This situation is worsened by the system's need of a large interval of time to recover from such an artifact because of the amplifier's high input impedance. MAs are sometimes considered as unpredictable phenomena, and current knowledge cannot satisfactorily explain, model, or eliminate them.

A combination of approaches might be needed when trying to rid an ECG of MAs. MA suppression techniques have been proposed through material selection, analog electronics and digital signal processing. Carefully evaluating the materials to be used is of high importance. For example, the mechanical properties of the materials influence the geometry of the sensor/skin interface. Analog solutions have the advantage of reducing MAs without impacting the processing time; however, they involve adding electronic components that translate into added cost and size for the analog front-end. Digital signal processing and artificial intelligence are the trending solutions to MAs; however, they require powerful computing units, and the digitized signal must not be saturated or highly attenuated.

1.4 Proposed Research and Objectives

While MAs remain a poorly understood problem, it is generally accepted that they stem from two main sources: capacitance variation and triboelectric voltages. The first occurs as a

result of relative movements of the electrode with respect to the skin that induce variations in the dielectric layer width (air gap, Y-direction in Fig. 1.3). The triboelectric voltage occurs because of the separation of two surfaces previously in contact, which takes place in the Y-direction (formation of an air gap) and also in the X and Z-directions (as defined in Fig. 1.3) from movements such as rubbing and sliding [12].

The modeling of MAs in current literature is limited and the subject is generally treated either as an unpredictable event [23] or modeled based on statistics rather than physics [21]. A common choice of model used to represent MAs is a time-varying capacitance in series with a voltage source [10], [24] (or parallel to a current source [25], [26]). A mathematical function describing the triboelectric generator was finally proposed by Li *et al* in [12], but it has not yet been verified against real motion artifacts.

The equations developed in [12] to describe MAs are similar to the ones presented in [27] for triboelectric nanogenerators (TENGs), which are thoroughly studied and well-modeled devices, suggesting a close relationship between the two physical phenomena. TENGs are energy-harvesting devices able to generate electricity from the repetitive contact and separation (or rubbing) of different objects. They usually consist of two metallic electrodes separated by one or more dielectric layers. Then, equivalently to capacitive electrodes, TENGs comprise contact electrification and varying capacitances.

In Chapter 3, an improved model for MAs in capacitive biopotential measurement is proposed, which includes both the effects of varying capacitance and triboelectric voltages for transverse motion (e.g. electrode losing contact with the body) and for longitudinal motion (e.g. electrode sliding over the body). Numerical simulations show the generated triboelectric voltage and the capacitance change separately, as well as the resulting artifact in a simplified capacitive electrode. The simulation results are finally compared to practical measurements of MAs in a capacitive electrode.

In a simplified manner, the electrode's coupling capacitance C_e and the electrode's input resistance R_{in} form a high-pass RC filter with a low cut-off frequency given by $1/2\pi C_e R_{in}$. Therefore, as C_e changes, due to different layers of clothing, pressure, and MA, so does the cut-off frequency. Assuming that C_e ranges from 1 nF and 1 pF, the required input resistance can be as high as 3.2 TΩ for diagnostic ECG.

The constraint of ultra-high input resistance is not easy to comply with and adds other challenges. In discrete designs, ultra-high resistors exist and can properly bias the amplifier's input. However, they are expensive and inaccurate. The bootstrapped bias circuit can boost the bias resistance and has been widely reported. In integrated designs, pseudo-resistors provide ultra-high resistances, and if needed, they can be included within a bootstrapped bias circuit. However, the bootstrapped bias circuit cannot compensate for the operational

amplifier's input resistance and the short-channel gate leakage in short-channel transistors.

According to [28], low-frequency common-mode signals lead to artifacts many times larger than the ECG signal for electrodes with mismatched low cut-off frequencies (e.g. 0.25 Hz and 0.4 Hz). A common design strategy in capacitive electrodes is selecting the input resistance according to the minimum C_e expected to ensure enough bandwidth. Then, each channel (or the differential signal) passes through a high-pass filter to remove artifacts in the extra/excessive frequency band. However, in this design technique, the input node possesses a slow time constant when the electrode capacitance is high. For example, if C_e is 1 nF and R_{in} is 320 GΩ, the time constant τ is 320 s. To quickly discharge the input node, two options are available: adding a controlled switch to the input node (adds an extra I/O) or diode-based circuits (clipping for signals greater than the forward voltage). In this dissertation, three manners of stabilizing the electrode's low cut-off frequency are proposed.

In Chapter 4, a MA suppression technique based on negative feedback is developed to compensate for the effects of electrode capacitance changes. Looking at the input node as a voltage divider between the electrode impedance and the input impedance, one can realize that it is a time-varying gain; and in electronics, negative feedback is known to stabilize gains. The proposed technique consists of applying a large gain to the measured signal and feeding it back through another set of electrodes. Two topologies are assessed, a single-ended version and a differential version. The simulations show that both the mid-band gain and the low cut-off frequencies become less dependent on the electrode capacitance.

Chapter 5 presents the design of an analog front-end (AFE) for capacitive electrodes with optimized cut-off frequency stability. The input resistance is boosted by a negative impedance converter (NIC). The design is demonstrated in TSMC 65nm technology to compensate for the gate leakage and verified through discrete design. The boosted input resistance allows the inclusion of a small capacitor (C_s) in series with C_e to reduce the fluctuations of the low cut-off frequency. Furthermore, the bootstrapped bias circuit was modified to reduce the MA detection/clipping range and to improve linearity.

Lastly, an all-analog integrated front-end that compensates for cut-off frequency fluctuations is designed in Chapter 6. It comprises an ultra-low input capacitance buffer with automatic control of the input resistance. The work of Chi [29] introduced the bootstrapped buffer, which allows values of C_e as low as 1 pF. Here, this buffer's bias circuit is replaced with a controllable pseudo-resistor, and a control loop is added. The circuit tracks capacitance variation and adjusts the input resistance to stabilize the low cut-off frequency and minimize the discharging time. The design focuses on an ECG system with a low cut-off frequency of 0.5 Hz and C_e between 1 pF and 100 pF. The circuit is designed in TSMC 65nm technology and the results are obtained through Spectre simulation of a (C+CC) layout

extraction and experimental measurements.

1.5 Dissertation Structure and Publications

This dissertation is expected to lead to 4 journal publications and a conference paper, and each of the following chapters relates to one of the articles. This introduction uses fragments from all of them, while Chapter 2 (State of the Art) reviews the relevant aspects of MA and capacitive ECG, and is mostly composed of paper "B". As mentioned previously, Chapter 3 proposes an MA model based on TENG models (paper "C"); Chapter 4 applies negative feedback for MA compensation (paper "A"); Chapter 5 designs an electrode with boosted input resistance, fast-discharging loop and series capacitance for cut-off frequency stabilization (Paper "D"), Chapter 6 demonstrates an integrated circuit with low input capacitance and adaptive input resistance that automatically corrects the low cut-off frequency (Paper "E"). In addition to the core chapters, Appendix A shows the implementation and performance of boosting circuits reviewed in Chapter 2. Appendix B describes the development of the ECG acquisition board, which is used in Chapters 5 and 6. Papers "A" to "E" are summarized in the list below following a chronological submission order.

- **A** - V. Sirtoli, G. Gagnon, G. Cowan, "Motion Artifact Mitigation Using Negative Feedback in Capacitively-Coupled ECG", **published in** *2020 18th IEEE International New Circuits and Systems Conference (NEWCAS)*, IEEE 2020, pp 323-326.

- **B** - V. Sirtoli, M. Liamini, L.T. Lins, M. Lessard-Tremblay, G. Cowan, R. Zednik, and G. Gagnon, "Removal of Motion Artifacts in Capacitive Electrocardiogram Acquisition: A Review", **published in** *IEEE Transactions on Biomedical Circuits and Systems*, April 26$^{\text{th}}$, 2023, pp 394-412.

- **C** - V. Sirtoli, L. Morelli, R. Zednik, G. Cowan, and G. Gagnon, "Motion Artifact Modeling of Capacitive Electrodes Based on Triboelectric Nanogenerators", **accepted in** *IEEE Transaction on Instrumentation and Measurements.*

- **D** - V. Sirtoli, S. Granata, G. Gagnon, and G. Cowan, "Input Resistance Boosting for Capacitive Biosignal Acquisition Electrodes", **published in** *IEEE Sensors*, December 19$^{\text{th}}$, 2023, pp 3004-3014.

- **E** - V. Sirtoli, S. Granata, G. Gagnon, and G. Cowan, "A Capacitive Electrode with Low Cut-off Frequency Stabilization for Biopotential Acquisition", in preparation.

Chapter 2

State of the Art

2.1 Skin-Electrode Interface

To understand the process of reading a biopotential with a capacitive electrode, one must be aware of the phenomena taking place at the contact interface layer. As with most dry electrodes, capacitive electrodes present a high coupling impedance, that is, the impedance seen from the human skin to the sensing element on the electrode. Fig. 1.3 showed the stack-up of layers that are normally present in a capacitive electrode. Further, each one of these layers contributes to the overall coupling impedance. Next, the most important layers and their impedance models are discussed.

2.1.1 Body Impedance

Although often ignored, there is an impedance from the ECG signal source (heart) to the section of skin with which the electrode is in contact. It has been modeled as a resistor in series with a voltage source (ECG signal), whereas this resistor corresponds to the resistance from soft internal tissues and contact resistance [30], [31]. The resistor value is dependent on the distance from the ECG source to the section of skin, in other words, the closer the electrode is to the source, the smaller the resistor is. The model for a complete and a simplified source impedance can be seen in Fig. 2.1.

Yoshiwaki *et al* [30] used the impedance voltage division principle to estimate the value of the equivalent source resistance. By controlling the AFE's input resistance they found the resistor value that attenuated the signal by 50%, meaning that this controllable resistor and the body internal resistance are equally valued. The reported range of resistance was from 2.88 kΩ to 4.12 kΩ. However, it is not clear whether the contact impedance between electrode and skin was accounted for. Sakaue *et al* [31] included the contact impedance in

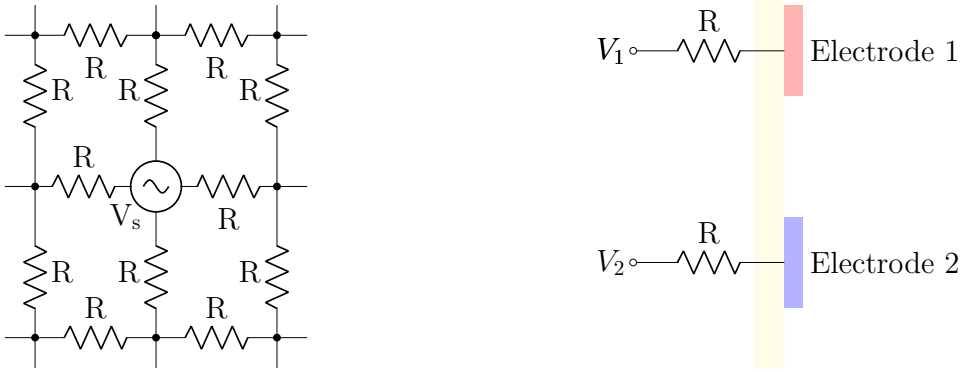

(a) Resistive internal body model

(b) Simplified source resistance seen from the skin

Figure 2.1: Model for the internal body resistance, where V_s is the biosignal generator and the different points in the human body are separated by a resistor R (a) and a simplified model (single source resistance) seen from the human skin (b) [31]. All resistor are represented with R, however, the actual resistance of each resistor may differ.

their analysis, which was 1 kΩ, and also prepared the skin. The measured values of internal body resistance ranged from 0.2 kΩ to 1 kΩ, depending on the electrode position and moment of QRS wave.

Additionally, the skin impedance can be modeled into multiple sections: sweat, *stratum corneum* and dermis [32], as shown in Fig. 2.2. The component values are extracted by fitting the contact impedance's response curves to different inputs into the model's governing equation. In [32], the range of measured values was: 0.64 kΩ< R_{1+3} <12 kΩ, 4.94 kΩ< R_2 <2500 kΩ, and 0.01 µF< C_2 <21.88 µF. Therefore, the total impedance seen from the source to the electrode can vary from hundreds of ohms to millions of ohms depending on skin preparation.

The DC voltage source in Fig. 2.2 is the consequence of a double layer potential. This phenomenon derives from the oxidation and reduction between a metal and an electrolyte. In other words, the ionic current in the body is transformed into an electron current in the electronic circuit [33]. Usually it is not present in cECG, which is one of the advantages of cECG compared to the traditional ECG system.

2.1.2 Modeling the Coupling Impedance

Figure 2.2 models the electrode as a single layer, however, this may not be accurate for capacitive electrodes. A common approach is to model each layer of a different material by a capacitor in parallel with a resistor [20]. Thus, the total coupling impedance (Z_{eq}) is their

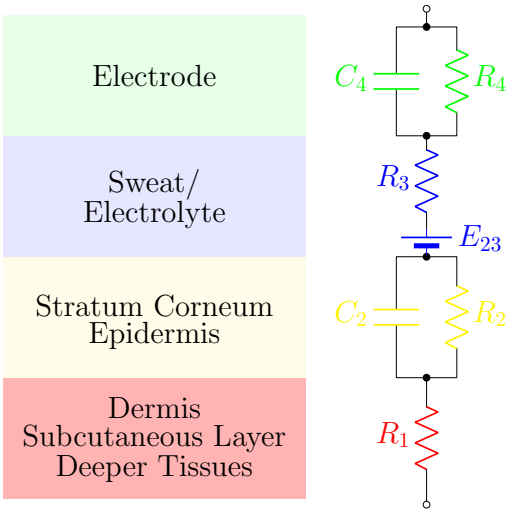

Figure 2.2: Source impedance model by Baba e Burke [32].

series combination as described by (2.1) [13].

$$Z_{eq}(j\omega) = R + \sum_{layer=1}^{n} R_x || \frac{1}{j\omega C_x} \tag{2.1}$$

where, R is the resistance of the conductive path (negligible) and R_x and C_x are the resistance and capacitance of each of the n layers. In cECG, the coupling impedance is often dominated by the insulator, clothing and air. Table 2.1 summarizes values of coupling capacitance/impedance found in the literature.

[Ref]	Elements	Value
[34]	C_e	tens of pF
[35]	C_e	0.5 to 8 pF (0 to 20 Hz)
[36]	C_e	2.4 to 19.4 pF (0 to 25 mm air gap, area $\approx$ 78.5 cm^2)
[37]	C_e	110 pF (5 Hz, area $\approx$ 33mm x 33mm)
[38]	$R_{clo}//C_{clo} + R_{ins}//C_{ins}$	Variable//113 pF + 3.1 TΩ//3.2 nF
[39]	C_e	0.1 to 10 pF (0.1 to 100 Hz)
[14]	C_e	92 pF
[40]	C_e	20 pF
[8]	C_e	10 pF to 200 nF
[41]	C_e	4 to 29 pF (0.5 to 3.5 mm, area = 12.7 cm^2)
[42]	$R_{ins}//C_{ins} + C_{air}$	200 MΩ//20 pF + 1pF to 1nF

Table 2.1: Values of coupling impedance reported in the literature. C_e is the single electrode capacitance, R_{clo} and C_{clo} are the clothing's resistance and capacitance, R_{ins} and C_{ins} are the insulator's resistance and capacitance, C_{air} is the capacitance introduced by the air

The values reported in Table 2.1 consider different layers and compositions of electrodes. When a single capacitance is reported, it was named as electrode capacitance C_e. Some reported the impedance of more layers such as the clothing's resistance and capacitance (R_{clo} and C_{clo}) and the insulator's resistance and capacitance (R_{ins} and C_{ins}). The capacitance imposed by air gaps C_{air} was also reported. In general, when the electrode is dominantly capacitive, C_e lies between 1 pF and 100 pF. However, if the resistive part of the coupling impedance is relevant, it can introduce large amounts of noise [43].

2.1.3 Materials and Geometry of Capacitive Electrodes

If the capacitive electrode is modeled as a single capacitor, the resulting C_e is described by (2.2). Where ε is the dielectric constant, A is the electrode area in meters and d is the dielectric thickness in meters.

$$C = \varepsilon \frac{A}{d} \tag{2.2}$$

2.1.3.1 Electrode Area

Increasing the electrode's area A leads to a higher electrode capacitance which eases the ultra-high input impedance constraints for the AFE. However, large electrode area reduces the resolution and is more likely to pick power line interference [28]. Smaller electrodes suffer less from relative capacitance changes because the probability of being affected by a motion is smaller, however, they demand higher AFE's input impedance and thus may present insufficient bandwidth [44].

2.1.3.2 Dielectric Thickness

The dielectric thickness and the electrode capacitance are inversely proportional. Therefore, thinner dielectrics lead to higher electrode capacitances. However, thin dielectrics have worse insulation and patient safety standards may not be met, requiring extra circuitry [28]. When the clothing is used as the dielectric, the coupling impedance presents a significant resistive component that is related to the textile's width. Hence, the clothing's thickness is directly linked to noise.

2.1.3.3 Environmental Influences

The pressure on the cloth was another matter of investigation in the work of Ueno *et al* [44], however, little influence was observed. The pressure is mostly related to keeping the

electrode still and to eliminating air gaps. Yet, in some applications, excessive pressure may change the dielectric's thickness.

Humidity is an important factor when the insulator is a fabric, wherein humid cotton for example, performs better than when dried [45]. A commonly observed effect of moisture is the improvement in cECG quality with time, because as sweat builds-up it moistens the clothing. Moisture is so important that a cECG system with closed-loop control of moisture has been proposed [26].

2.1.3.4 Choice of Material

The choice of dielectric and substrate in which the electrode is built may be the most important design parameter. Besides the dielectric performance of the insulator layer and addition of noise due to the resistive component, the electrode's mechanical properties also determine how the electrode conforms to the body. Currently, a lot of effort is being applied to the research of flexible materials that can provide high quality ECG signals while adapting its geometry as the patient moves [46]. Moreover, how the insulating layer is applied and cut also changes the electrode's flexibility and hence its performance [47].

2.2 Motion Artifacts (MAs)

The term "motion artifact" refers to any error in a biopotential measurement caused by the patient's movement. In cECG, when a movement occurs, two important mechanisms take place: electrode capacitance variation and generation of triboelectric voltages [48]. Although the capacitance variation mechanisms are straightforward, the generation of triboelectricity is not, and understanding this phenomenon may be key to solving it.

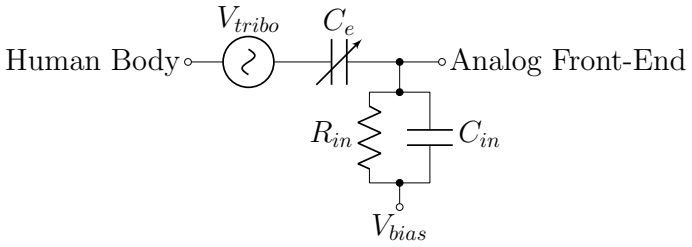

Figure 2.3: Node connecting the human body to the Analog Front-End, where C_e is the electrode capacitance, V_{tribo} is the triboelectric voltage source, C_{in} and R_{in} are the input capacitance and resistance, and V_{bias} is the bias voltage.

The electrode coupled capacitance forms a voltage divider with the sensor's input capacitance, as shown in Fig. 2.3. Also, changes in the electrode capacitance can introduce spikes

and baseline fluctuations. That is, the amplifier's bias voltage, the accumulated charges on the skin's and electrode's surfaces, and the skin's potential create a DC voltage drop across the electrode capacitance [35], leading to artifacts caused by voltage modulation when C_e varies ($Q = CV$). This phenomenon is also known as microphonics.

Yet, MA cannot be entirely explained by electrode capacitance variations alone and triboelectricity should also be accounted for. In Fig. 2.3, triboelectricity is represented as a voltage source in series with the signal path. Triboelectricity is the formation of a relative electrostatic charge between two materials that are rubbing against each other. When two materials are in contact, the charges at the contact layer will interact and redistribute [27] (Fig. 2.4b). At the moment these two surfaces split, they remain charged, creating an electrostatic voltage (Fig. 2.4c). The faster the splitting time, the larger the resulting potential, because only a small number of electrons can move back to the original surface [25]. Although both metals and insulator can store charges, in metals, charges can move easily, which allows them to discharge faster than in insulators [12]. Thus, both the choice of material and the dynamics of the surface's movement are contributing factors in the generation of triboelectricity.

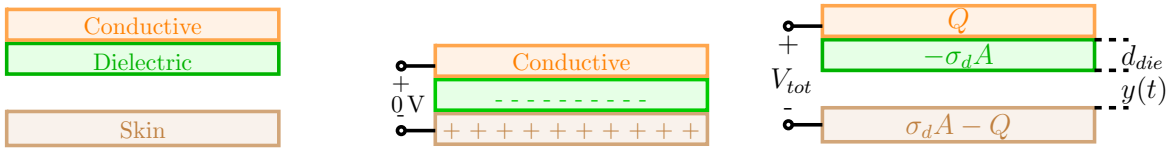

(a) Uncontacted (b) Contact (c) Separated surfaces

Figure 2.4: Tribocharging process. a) Uncontacted surfaces; b) Dielectric and skin have the same charge density with opposite sign during contact; c) The resulting amount of charge in each surface after the surfaces split

The triboelectric series consists of a list that empirically ranks materials by their tendency to exchange electrons through contact/friction [49]. This property is called charge affinity and is measured in nC/J in the metric system. It represents the amount of charge transferred from one surface to another per energy spent to split those surfaces apart. In addition to charge affinity, the triboelectric charge density (TECD) resulting from the interaction of two materials depends on humidity, surface roughness, temperature, stress and other mechanical properties [50], [51]. Because of the complexity involved in the triboelectric effect's mechanics, accurate sensing and prediction of surfaces' TECDs is not straightforward; thus, the difference between calculated and measured surface potential are typically two orders of magnitude [25]. Recently, TECD values for different materials were published [51]. The triboelectric series and TECD list are given in Table 2.2. Unfortunately, the TECDs of a few critically important materials for cECG, such as oily and dry skin, remains unavailable.

Table 2.2: Example of triboelectric series [52] and triboelectric charge density (TECD) values [51].

Material (Abbreviation)	Affinity [nC/J]	TECD [$\mu C/m^2$]
Oily skin	+45	
Dry skin	+30	
Wood	+7	-14
Cotton	+5	
Polyimide film (Kapton)	-70	-93
Polystyrene	-70	-103
Clear polyvinyl chloride (PVC)	-100	-117

2.3 Modeling of Errors in cECG Instruments

A simplified schematic of a cECG system is shown in Fig. 2.5. The desired signal is represented as V_{ecg}, the voltage difference between two points of the human body generated by cardiac activity. From the heart to surface of the skin, the internal organs present bioimpedance, represented by Z_{b_p} and Z_{b_n}, and the skin bioimpedance that connect the two measuring points is named as Z_{skin} [53]. For simplicity, most models ignore the bioimpedance because their values tend to be very small compared to the electrode impedance and the amplifiers' input impedance. Hence, Z_{b_n} and Z_{b_p} can be replaced by a short-circuit and Z_{skin} by an open-circuit. The voltage source V_{cm_b} models other voltages that are present in the human body and are detectable throughout the whole body.

The electrode is modeled by a variable capacitor (C_{e_p} or C_{e_n}) in series with a voltage source (V_{oc_p} or V_{oc_n}). As the patient moves away from the electrode, the air layer thickness increases, thus the overall electrode capacitance decreases. Note that the electrode is assumed to be mainly capacitive. More accurate modeling should introduce a resistor in parallel with C_e. The voltage sources V_{oc_n} and V_{oc_p} represent the triboelectric potential difference generated by the separation of two insulating materials [12], [25].

The electronic part comprises two buffers, with input impedance Z_{in_p} and Z_{in_n}, which are the parallel combination of a resistor and a capacitor. The output is given by the difference of V_{out_p} and V_{out_n}.

The body is also coupled to the main supply V_{line} (60 Hz) by the capacitor C_{lb} and to the earth ground by C_{bg}. The earth ground is separated from the electronic ground by an isolation capacitor C_{iso} [54], [55].

From Fig. 2.5 most sources of errors in cECG can be identified. Some of them are common to cECG, standard ECG, and general biopotential measurements, thus analysis and solutions from these topics may also be mentioned here.

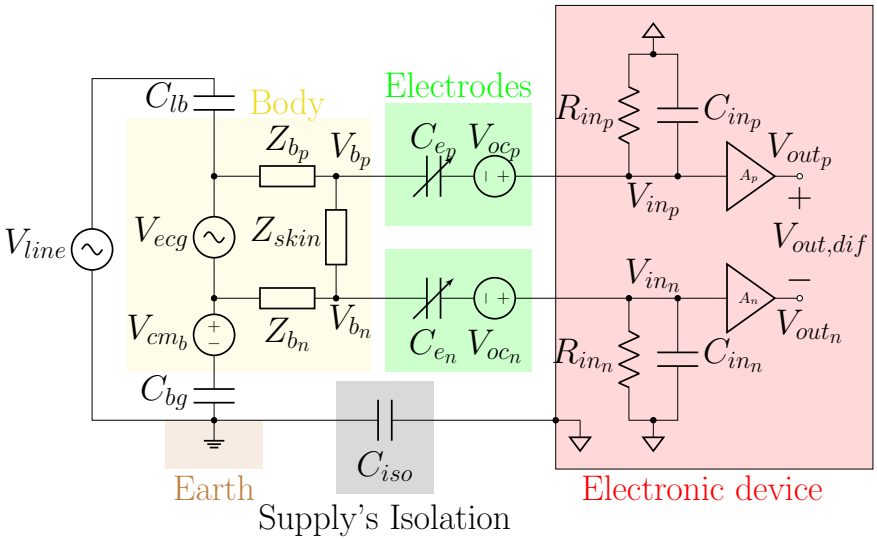

Figure 2.5: Circuit model of a cECG system

2.3.1 Common-Mode Voltage

The common-mode voltage appears equally in both V_{out_p} and V_{out_n} and it is computed by (2.3), wherein the reference voltage (0 V) is the circuit ground. The buffer gain is assumed to be ideal ($A_n = A_p = 1$), hence $V_{in_n} = V_{out_n}$ and $V_{in_p} = V_{out_p}$. An ideal differential measurement would solve the problem, however, the common-mode rejection ratio (CMRR) of non-ideal differential amplifiers is not infinite. Moreover, mismatches between electrodes further decrease the overall CMRR.

$$V_{cm} = \frac{V_{out_n} + V_{out_p}}{2} \tag{2.3}$$

In practical applications, the common-mode rejection ratio (CMRR) should be approximately 100-120 dB, otherwise, the common-mode voltages can appear in the output as a differential signal overlapped with the biosignal [56]. Hence, the actual output is approximately a linear sum of the desired differential voltage V_{ecg} with the common-mode voltage. This artifact may get even more harmful, as its amplitude may be high enough to saturate the output [57].

There are many sources of common-mode voltage in biopotential acquisition, for example, V_{cm_b} comprises all other voltage sources in the human body, such as the electrodermal voltage [10] and the breathing signal. However, the most significant is the power-line-induced voltage. The capacitances C_{lb} and C_{bg} form a closed loop with V_{line} [56]. Ignoring the bioimpedance and taking the whole body as a single node, the common-mode voltage in the human body

due to V_{line} (V_{cm_l}) is calculated as (2.4).

$$V_{cm_l} = V_{line}\frac{sC_{lb}}{sC_{lb} + sC_{bg}} \tag{2.4}$$

As an example, a simple calculation allows us to estimate the common-mode voltage due to the power line. Considering the body as a homogeneous conductor, V_{line} as a sinusoid with amplitude of 120 V at 60 Hz, C_{lb} of 2 pF and one capacitance to ground (C_{bg}) of 200 pF, then the voltage at the body due to power line interference is approximately 1.2 V ($110\frac{2\text{pF}}{200\text{pF}+2\text{pF}}$) while the ECG amplitude is 1 mV. In that case, $V_{cm,l}$ must be attenuated by at least 80 dB to render the R-wave visible.

2.3.2 MAs Effects on cECG

In a recent study, the performance of cECG was evaluated in three cases: motion-free, short motion and large motion. The results showed that even a small movement can reduce the signal-to-noise ratio (SNR) by 15 dB or generate non-linear saturation effects [58]. MAs can be global, affecting all electrodes, or local where only a single electrode contains the artifact. Local MAs are the ones that cause most of the issues since global MAs appear similarly in multiple electrodes and are suppressed by differential measurement.

From Fig. 2.5, the triboelectric voltage (V_{oc}) adds to V_{b_x} as it is in series with the signal path (going into the amplifier). This voltage is considered almost random [25], [50]; it varies from electrode to electrode and relies on many parameters that are difficult to track and compensate for: contact area characteristics (area, angle, pressure), speed of separation, charge density of the material, distance from body to electrode and surface roughness.

The capacitance between the skin and an electrode may present a DC potential, which arises from multiple sources: amplifier's input bias, skin's DC potential and triboelectricity (static charges) on the body surface and in the capacitive sensor [35]. Therefore, the variation of this capacitance due to a given motion will modulate the DC voltage, summing it to the ECG signal [35]. Numerical simulations of a time-domain single electrode model showed that capacitance variations in the presence of a static common-mode voltage as low as 10 mV led to an unreadable ECG waveform [59].

Consequently, another issue with MAs is the settling time. It is well-known that the time constant (τ) is tied to the low frequency cut-off ($f_c = 1/2\pi\tau$), defined by the RC high-pass filter (hence $\tau = C_{e_{n,p}}R_{in_{n,p}}$). The very high impedances on the input node make the discharging of triboelectric voltages slow [24], thus a high amplitude artifact will likely cause a large amount of ECG data to be missed during the discharging period. Reducing the

input resistance may lead to insufficient bandwidth when the electrode capacitance decreases, meaning that an important part of the ECG spectrum is filtered.

Errors also arise because of the limited input impedance (Z_{in}). The voltage at the amplifier's inputs (V_{in_x}) is given by:

$$V_{in_x} = V_{b_x} \frac{Z_{in_x}}{Z_{in_x} + Z_{e_x}} \tag{2.5}$$

where Z_{e_x} is the electrode impedance and x stands for p or n as shown in Fig. 2.5. For now, we assume $R_{in} \approx \infty$. The average value of C_e is in the range of tens of pF when the patient has good contact with the electrode and C_{in} is a few pF. Hence, when the electrode coupling is strong, it is safe to assume $V_{in_x} = V_{b_x}$. However, if the patient's body gets farther from the electrode, the capacitance C_e drops. Assuming that both electrode capacitances change equally as a result of a given movement, and that $Z_{e_x} = Z_{in_x}$, then $V_{in_x} = V_{b_x}/2$. This result shows that in extreme cases, when the electrode capacitance is equal to (or even smaller than) the input capacitance, the signal amplitude at the buffer input drops by half (or more).

Moreover, the MA causes common mode to differential conversion [60]. If a common mode signal $V_{cm_{in}}$ (such as V_{line} or V_{cm_b}) is applied directly to both electrodes so that $V_{cm_{in}} = V_{b_n} = V_{b_p}$, and the positive branch has good contact ($Z_{e_p} = Z_e$) and the negative branch is badly coupled ($Z_{e_n} = Z_e + \Delta Z_e$), the voltages at the input nodes are $V_{in_p} = V_{cm_{in}} Z_{in}/(Z_{in} + Z_e)$ and $V_{in_n} = V_{cm_{in}} Z_{in}/(Z_{in} + Z_e + \Delta Z_e)$. Hence the differential measurement of the two channels contains a term ΔZ_e that distorts the measured signal. Mismatches between the two channels in a differential measurement of biopotentials can drive the common-mode rejection ratio (CMRR) below acceptable levels [61]. This artifact is aggravated in frequencies around the cut-off frequency, where the effect of mismatch is larger.

To display the impact of unmatched cut-off frequencies between electrodes, the data from two ECG channels was measured simultaneously, using capacitive electrodes with a cut-off frequency much lower than 0.5 Hz under heavy breathing. The unfiltered difference between the 2 channels is displayed in Fig. 2.6 labeled as "Original". Although the ECG waveform is recognizable, it suffers from a phenomenon called baseline wander, which is the change in the baseline of the signal.

The ECG waveform, under matched and slightly unmatched low cut-off frequencies, is demonstrated by applying digital high-pass filters to each channel. In Fig. 2.6, the matched signal was constructed with both electrodes' cut-off frequencies at 0.5 Hz, while the unmatched waveform came from an electrode with a cut-off frequency of 0.5 Hz and the

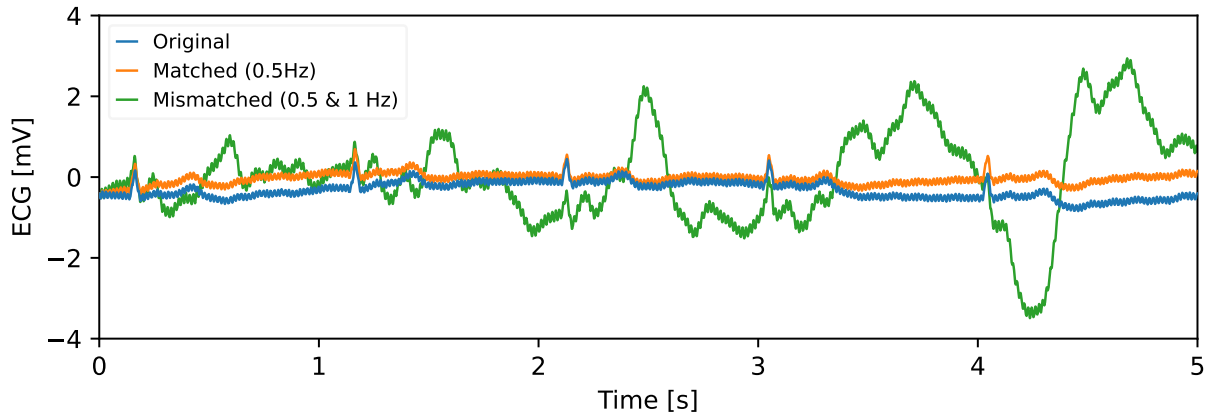

Figure 2.6: ECG with different cut-off frequencies under strong artifacts

other with a cut-off frequency of 1 Hz. This simulation shows that matched electrode cut-off frequencies can remove the baseline wander, while unmatched cut-off frequencies can lead to unreadable ECG.

2.3.3 Bias Current

Another issue in the design of ultra-high input impedance electrodes is the need for a path for the input biasing current. DC currents are usually not allowed in the human body, nevertheless, C_e blocks this current from going into the body, thus a path to ground is required. In other words, if a path to ground is not provided, C_e will integrate the biasing current from the operational amplifier, building up a voltage that may saturate the input [62].

Typical values of commercial devices are input impedance in the region of TΩ and bias currents of about tens of fA [13]. Castro *et al* [41] gives two examples of commercial amplifiers that can be used in the reading of cECG, the LTC6240 with a 10 GΩ resistance to ground and the INA116 with floating inputs. However, both solutions suffer from drawbacks, the floating input may saturate due to MA; while introducing a resistor in parallel with R_{in} reduces the overall input impedance [13].

2.3.4 Noise

The buffer is a common choice for a first-stage amplifier; thus it is of interest to evaluate the noise performance of this circuit. Two main sources of noise are added to the circuit by the operational amplifier, voltage noise (e_n) and current noise (i_n) as shown in Fig. 2.7 [63]. Here, e_n and i_n are noise power spectral densities (PSD) given in $\mathrm{V}/\sqrt{\mathrm{Hz}}$ and are

uncorrelated variables. In this analysis, the model was simplified to a single electrode, and C_e is connected directly to the circuit's ground. Moreover, the buffer gain is defined as unitary over the whole bandwidth.

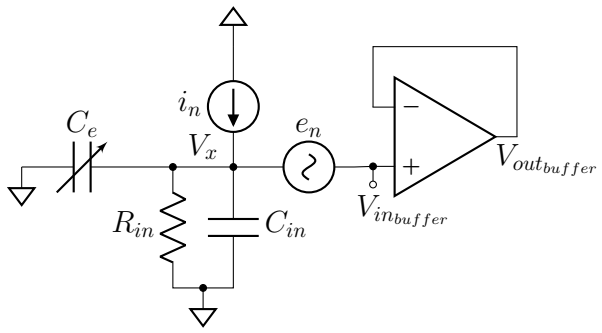

Figure 2.7: Buffer noise model

The voltage noise transfer functions NTF_{buf_v} is straightforward, since there is no current going into the amplifier's input, the current through e_n is null and V_x is 0 V (i_n is excluded for now), thus the gain is unity. The current noise transfer function, NTF_{buf_i}, is not as simple. By setting e_n to 0 V, the current leaving i_n flows into the equivalent impedance between C_{in}, C_e and R_{in}, then NTF_{buf_i} is computed with (2.6).

$$NTF_{buf_i} = \frac{R_{in}}{1 + s(C_e + C_{in})R_{in}} \tag{2.6}$$

The resulting noise is calculated as the integral of the PSD times the squared magnitude of the noise transfer function. The integration variable is the frequency and it is limited by a low (LF) and a high (HF) frequency. Equation (2.7) shows the output noise contribution from e_n ($V^2_{buf_e}$) while (2.8) refers to the contribution of i_n ($V^2_{buf_i}$).

$$V^2_{buf_e} = e_n^2(HF - LF) \tag{2.7}$$

$$V^2_{buf_i} = \frac{i_n^2 R_{in}}{(C_e + C_{in})}\left\{\tan^{-1}[HF(C_e + C_{in})R_{in}] - \tan^{-1}[LF(C_e + C_{in})R_{in}]\right\} \tag{2.8}$$

The root mean square (RMS) output noise voltage is given by the square root of the sum of $V^2_{buf_i}$ and $V^2_{buf_e}$ as defined by (2.9).

$$V_{buf_{nrms}} = \sqrt{V^2_{buf_i} + V^2_{buf_e}} \tag{2.9}$$

As an example, one can replace commercial values of e_n and i_n to estimate the noise of a cECG system. The operational amplifier chosen here is the LTC6240, also used in [41], [48]. From the datasheet, the input noise voltage from 0.1 to 10 Hz is $550\,\mathrm{nV_{pp}}$, for higher frequencies the input noise voltage density $7\,\mathrm{nV}/\sqrt{\mathrm{Hz}}$ and the input noise current density is $0.56\,\mathrm{fA}/\sqrt{\mathrm{Hz}}$. The integration bandwidth ranges from 0 (LF) to 1 kHz (HF). From the LTC6240 datasheet we can also find R_{in} and C_{in}, 1 TΩ and 3 pF respectively, while C_e is taken from the worst-case scenario, 1 pF. The calculated output RMS noise is 0.34 mV.

By performing a noise analysis using LTspice of the circuit shown in Fig. 2.7, where the operational amplifier is the LTC6240, the result from equation (2.9) is verified. The bandwidth of integration in the noise analysis was from 1 nHz to 1 kHz, and the output noise voltage was 0.22 mV (RMS value). The noise analyses, by equation and simulation, led to similar results 0.34 mV and 0.22 mV. The error between these results can be accounted to the simplifications made in the equations, the buffer gain was unitary for all frequencies and the input capacitance used was just the common-mode one. Yet, the RMS output noise shows us that when the electrode is badly coupled to the patient body, the noise levels can be as high as the ECG signal amplitude.

The noise model for other circuits used in cECG, such as the instrumentation amplifier, the transconductance amplifier, or the charge amplifier are provided in [13]. In [64], the authors achieved a biopotential electrode with a noise level of $2\,\mu\mathrm{V}/\sqrt{\mathrm{Hz}}$ at 1 Hz. Moreover they state that for usual heart diagnostics, a 30:1 relation of signal to noise is sufficient.

2.3.4.1 Walk Around Artifact

Another issue associated with the use of ultra-high bias resistances is the artifact picked up when motion happens close to the patient being monitored, which is named here the "walk-around artifact". Objects and humans other than the patient also have charges on their surfaces, and hence couple through the air with the electrode's input node. Fig. 2.8a models this artifact, where C_e and R_{in} are the same as in Fig. 2.7 and C_{se} is the capacitance coupling a secondary person to the electrode. Moreover, V_s is the signal generated by the second person's motion, and V_{WA} is the resulting component measured by the electrode.

By assuming a relatively small C_{se} value of 1 pF, and changing R_{in} and C_e, Fig. 2.8b shows the frequency response at node V_{WA} for a unity V_s. The frequency response presents a high-pass behavior, where the pass-band amplitude depends mostly on the value of C_e. Thus, electrodes poorly coupled to the patient are more prone to pick up surrounding noise. This is very problematic, especially in the case of 60 Hz interference. However, the value of $R_{b,f}$ sets the low cut-off frequency, which is approximately the same as f_l because C_{se} is small. Therefore, walk-around artifacts in frequencies around the motion and respiration

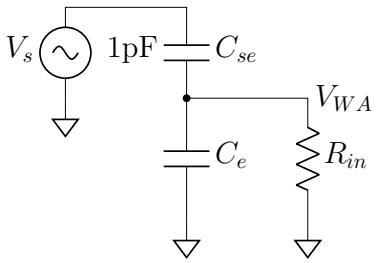

(a) Walk around artifact model

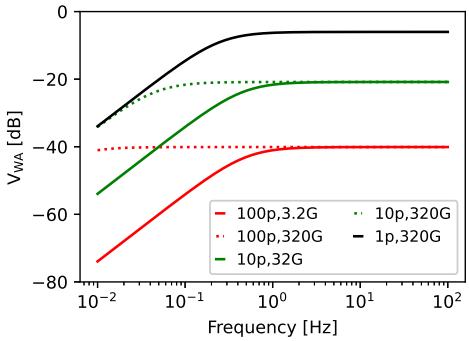

(b) Frequency response of the walk around artifact, legend in the format of (C_e,R_{in})

Figure 2.8: The walk around artifact

ratio (≈200 mHz) can be attenuated by accurately setting R_{in}.

2.4 Analog Boosting Circuits

A broad variety of circuits are used in biopotential capacitive sensing to improve the measurement of ECG signals. MA suppression circuits should boost the input impedance to deal with capacitance changes while providing a quick discharge path to remove triboelectric charges on the input node. However, circuits that reduce MAs by indirect means are also considered in this section. For example, in Fig. 2.5 there are two clear sources of common-mode signals in the body: V_{cm_b} and V_{line}. Moreover, V_{oc_p} and V_{oc_n} might also impose common-mode potential in the inputs. Thus, by applying common-mode attenuation techniques, errors due to MA effects such as common-mode to differential conversion of triboelectricity can be compensated for.

2.4.1 Input Impedance Boosting With Positive Feedback

Neutralization (Fig. 2.9) and Bootstrapping (Fig. 2.10) are two different input impedance boosting techniques. While similar in some aspects, these two techniques differ sufficiently to be analyzed separately.

The neutralization circuit creates a negative capacitance in parallel with an undesired capacitance. If these two capacitances have the same absolute value with different signs (+C and -C), they cancel each other out. Meanwhile, bootstrapping works by feeding the signal applied to one terminal of a capacitor to the other terminal; thus, the voltage drop across

the capacitor is zero and no current flows.

The similarity of these techniques comes from both having a capacitor in a positive feedback loop, which improves the input impedance of the amplifier. The difference is that neutralization combines a gain that differs from unity with an external capacitor while bootstrapping employs a unitary gain without an extra capacitor. Partial bootstrapping can also be used to increase the amplifier's input resistance while still properly biasing the input (Fig. 2.12).

2.4.1.1 Neutralization

In Fig. 2.9, the front-end input node (V_x) is connected to the opamp's input capacitance and, possibly, capacitances from a biasing circuit and from the printed circuit board (PCB). A well-explored solution is the use of neutralization circuits, which mimics the current flowing through C_{in} [62], as shown in Fig. 2.9.

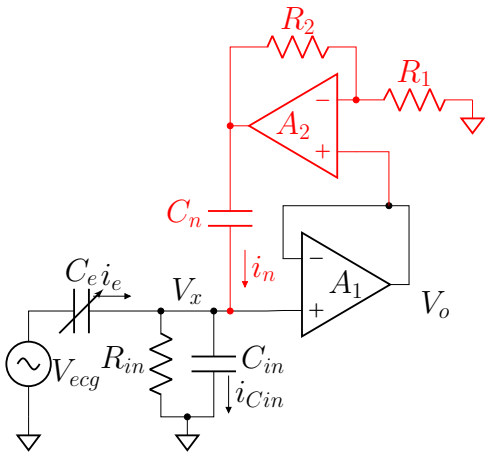

Figure 2.9: Capacitance neutralization circuit

Because the mid-band gain is given by the capacitive voltage divider, we can ignore R_{in} for this analysis. The nodal equation at node V_x can be written as: $i_e + i_{Cin} + i_n = 0$. Thus, the sum of the currents from C_e and C_{in} and from the neutralization circuit must be zero. If $|i_{Cin}| = |i_n|$, and one is arriving at the input node and the other is leaving it, then $i_e = 0$ to satisfy the nodal equation. Hence, if there is no current flowing from the body to the circuit (through the electrode), there is no voltage drop over C_e, and the voltage at the input node is equal to V_{ecg}. By deriving the circuit transfer function (2.10) in terms of impedances (Z_{in}, Z_e and Z_n are the impedances of C_{in}, C_e and C_n, respectively) and a constant gain $A_n = 1 + R_2/R_1$, we can explore this solution further.

$$\frac{V_x}{V_{ecg}} = \frac{Z_{in}Z_n}{Z_{in}Z_n + Z_e(Z_{in} + Z_n - A_nZ_{in})} \tag{2.10}$$

To cancel the effect of Z_e, the term that multiplies it must be zero. Therefore, when $Z_{in} + Z_n = A_nZ_{in}$ the transfer function is reduced to unity. To accomplish this condition, it is necessary to set a gain in the non-inverting amplifier of $1 + Z_n/Z_{in} = A_n$ or an impedance $Z_n = (A_n - 1)Z_{in}$, these equalities are known as "neutralization conditions".

Taking into account a finite value for R_{in}, the neutralization condition is adapted so that only C_{in} is neutralized. Note that a resistive path to ground is required to bias the amplifier's input. Therefore, the capacitance neutralization condition is (2.11) and the gain from the cardiac source (V_{ecg}) to the input of the amplifier (V_x) are given by equation (2.12).

$$C_{in} = C_n(A_n - 1) \tag{2.11}$$

$$\frac{V_x}{V_{ecg}} = \frac{s}{s + \frac{1}{C_eR_{in}}} \tag{2.12}$$

The non-inverting amplifier provides a gain $A_n = 1 + R_2/R_1$, where $R_2/R_1 = \delta$. If $Z_n = 1/sC_n$ and $Z_{in} = 1/sC_{in}$, then $C_n = C_{in}/\delta$ and by adjusting δ and/or C_n the capacitance of C_{in} can be neutralized [62]. To overcome the inaccuracy of resistors, Chi *et al*, used a potentiometer in parallel with R_1 and R_2 that allows fine-tuning. They also inserted a large capacitor in series with R_1 to select the gain bandwidth (block DC gain) [65].

It should be noted that the voltage follower might not be necessary, because the potential at node V_x can also be measured from the inverting input of A_2; thus, the non-inverted input of A_2 can be connected directly to V_x and A_1 eliminated [65].

Although the neutralization technique adds positive feedback, it will not oscillate while $C_e + C'_{in} > 0$, where C'_{in} is the resulting input capacitance (after addition of neutralization) [65]. The neutralization also increases noise; but when the electrode presents a large coupling capacitance to the body, other sources of noise will dominate, such as the bias circuit (presented later in this section) [8]. Considering the current (i_n) and voltage (e_n) noise sources in the opamp's input, the gains from these sources to the output are $1/sC_e$ and $1 + [(C_{in} + C_n)/C_e]$, respectively [65].

2.4.1.2 Bootstrapping

The bootstrapping circuit works by feeding back V_x (see Fig. 2.10), which is on the upper terminal of $C_{in_{AMP}}$, to the other terminal of this capacitor [29]. Because the buffer is used to isolate V_x, its output can be wired to $C_{in_{AMP}}$. Once this positive feedback is established, the voltage drop across, and hence the current through, $C_{in_{AMP}}$ are zero.

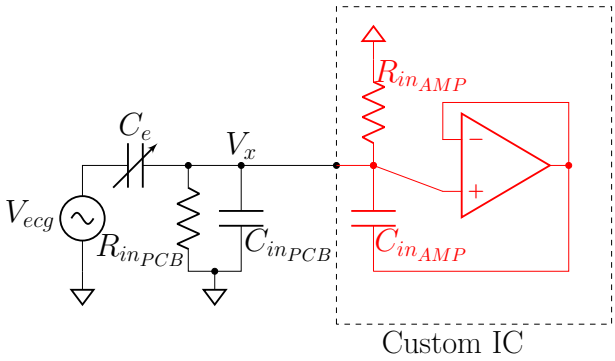

Figure 2.10: Bootstrapping circuit

This can be best illustrated mathematically by applying Miller's theorem, which states that a feedback impedance ($Z_{f_{Miller}}$) across an amplifier with gain k can be split into two grounded impedances, one connected to the amplifier input ($Z_{in_{Miller}}$) and the other to the amplifier output ($Z_{out_{Miller}}$). The value of the resulting input Miller impedance is given by (2.13).

$$Z_{in_{Miller}} = \frac{Z_{f_{Miller}}}{1-k} \tag{2.13}$$

If the gain k is one, then $Z_{in_{Miller}} = \infty$. Applying this to the case of Fig. 2.10, the impedance from the capacitor in the feedback reflected to the opamp's input must be ∞, thus the resulting input capacitance is zero. In this way, the input capacitance of an operational amplifier ($C_{in_{amp}}$) can be canceled.

Bootstrapping better suits the transistor-level designs because $C_{in_{AMP}}$ is not accessible on commercial integrated circuits (ICs), albeit it can still be done with off-the-shelf components by driving the circuit ground [66]. In custom ICs, however, the designer has access to the gate-to-source capacitance C_{gs}, gate-to-body capacitance C_{gb} and gate-to-drain capacitance C_{gd} (dominant components of $C_{in_{AMP}}$) [29].

The leakage capacitance in the PCB can also be bootstrapped by using the guarding/shielding technique. Fig. 2.11 shows a combination of a circuit schematic and layout to explain the guarding technique. Similarly, the bootstrapping technique can be used to

reduce the stray capacitances in coaxial cables, where the inner wire contains the signal and the outer conductor is driven by the buffer's output.

The gray box represents the IC of an operational amplifier, which has two input nodes and one output. In order to create a voltage follower, a trace in the PCB (orange solid lines) connects the inverting input to the output. Moreover, the non-inverting input is also connected to the electrode by a PCB trace. If there were no guarding in the input pin, a stray capacitor would be formed between this trace and the ground, increasing the input capacitance. By surrounding the input pin with PCB lines (orange dotted line) containing a replica of the input signal (V_o), the capacitance (C_{guard}) formed in the input node is between two almost identical signals; thus, it should be negligible [14], [62]. Meanwhile, the ground planes and routes form a capacitor with the guard ring (C_{leak}) that does not affect the signal quality.

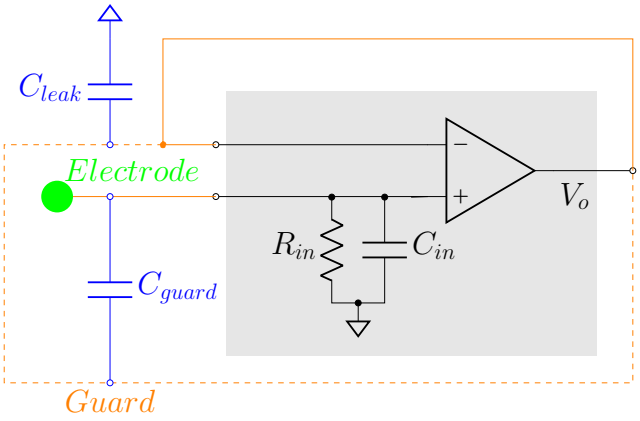

Figure 2.11: Method of guarding the input pin

It is clear that the guarding method creates positive feedback in the circuit through C_{guard}; however, it should not lead to instability in well-compensated operational amplifiers [62]. The drawback of the guarding is the increment in the contribution of the amplifier input-referred voltage noise, which now sees a gain of C_{guard}/C_e to the output [62].

2.4.1.3 Input Biasing

The input biasing circuit affects the input resistance. Ideally, the bias circuit should provide a low-impedance path for DC, very low-frequency signals, and large MA (triboelectricity), while imposing an ultra-high impedance within the ECG bandwidth. Note that when C_e drops due to a MA, the low cut-off frequency increases. Thus, R_{in} should be large enough to set the desired low cut-off frequency even when C_e is minimum. On the other hand, increasing R_{in} lengthens the discharging time. One way of complying with this is to apply the bootstrap technique in the biasing circuit shown in Fig. 2.12a.

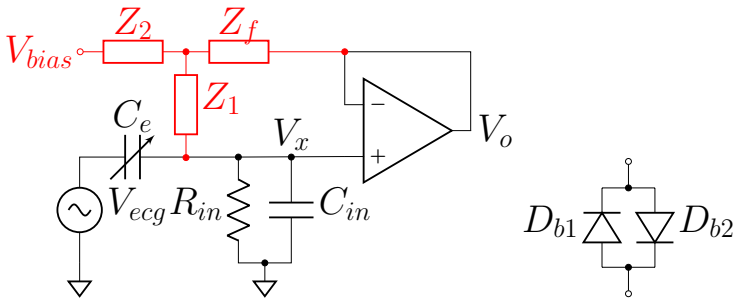

(a) Bootstrapped bias

(b) Counter-Diodes

Figure 2.12: Input stage biasing schematics

The resulting input impedance of the bootstrapped bias circuit is (2.14).

$$Z_{in,bb} = Z_1 + Z_2 + \frac{Z_1 Z_2}{Z_f} \tag{2.14}$$

The most common implementation uses Z_1 and Z_2 as resistors and Z_f as a capacitor [67]. At DC, the capacitor is open and the impedance to ground is just two resistances in series ($R_1 + R_2$). Within the band of interest, the capacitor is a short-circuit and the voltage drop across the first bias resistor (R_1) is almost zero, which is seen from the input node as an ultra-high resistance. In the IC design of Chi *et al.* [29], two PMOS diode-connected transistors were used as R_1 and R_2 (this kind of element is also known as a pseudo-resistor).

An alternative to resistors in the bootstrapped bias is to use the diode's reverse leakage current [39], [65], [68], which adds temperature compensation, protection and clamping. The circuit in Fig. 2.12b shows a counter-diode connection that can replace R_1. When the electrode is well coupled to the body, it is expected that D_{b1} and D_{b2} are off, hence presenting high resistance. It is necessary that the leakage current of the reverse biased diodes is high enough to sink the bias current flowing out of the amplifier input. In the presence of an interference that causes large voltages at V_x, the diodes conduct and discharges the node quickly.

As seen in (2.14), the input impedance is $R_1 + R_2$ for low frequencies and $2\pi f C_f R_1 R_2$ for higher frequencies [69]. That means $Z_{in,bb}$ is directly proportional to the frequency, which is an inductive behavior [70]. The combination of this inductive behavior with the electrode capacitance may lead to resonance and even oscillation.

Recently a modification was proposed where the feedback capacitor is replaced by a resistor (R_f) and R_2 by a varistor R_v [69]. Then, the frequency-dependent term created by the capacitor is replaced by $R_1 R_v / R_f$, and R_v has a large value for small signals and a low

resistance in the presence of large voltages. In this manner, Z_{in} quickly discharges when large MAs occur while showing high input impedance in normal operation. This biasing schematic can also be implemented with resistors only [70], but this would lead back to the issues of R_b such as noise and lack of protection against large and low-frequency artifacts.

2.4.2 Channel-Mismatch Using a Reference Signal

This technique was recently proposed in [60] for ECG, but could be adapted for cECG. A known common-mode voltage V_{ref} is injected into the system. While the measured ECG should not contain V_{ref} (an ideal differential measurement eliminates it), because of voltage division between the electrode's impedance and the amplifier's input impedance, as well as the amplifier's gain inaccuracy, each channel may apply a different overall gain to V_{ref}. Consequently, by taking the difference between two channels and by measuring the amplitude of V_{ref}, the gain mismatch can be deduced. To assess the real gain of each channel, one can compare the amplitude of the recovered V_{ref} to the amplitude of the injected V_{ref}. This leads to multiple options for gain correction or CMRR optimization.

2.4.3 Series Negative-Impedance

The voltage division created by C_{in} and C_e (see Fig. 2.3 and (2.5)) due to small electrode capacitance can be solved by increasing the input impedance as discussed earlier or by decreasing the electrode's apparent coupling impedance. To compensate for the electrode's impedance, a negative impedance circuit was placed in series with it [71]. With a negative version of the electrode's impedance in series, they sum and null each other.

In [71], the apparent impedance from the negative impedance sensor was $-200\,\mathrm{M\Omega}$ (resistive) and the estimated electrode capacitance was 510 pF. The preliminary use of the negative impedance capacitive sensor showed an improvement in SNR of approximately 6 dB, from 23.9 dB to 30.2 dB. Although series negative-impedance compensation is a promising technique, that work was limited by the lack of consideration of the parasitic effects in the negative impedance circuit, and the negative impedance being fixed. Hence, it could not adapt to changes in the electrode capacitance in the event of MAs.

2.4.4 Discharging Switch

As discussed before, MAs generate triboelectricity which occurs as a result of the accumulation of charges in the contact surfaces (skin-electrodes). Those charges cannot move quickly in dielectric materials; thus, the discharge in such a surface is slow.

To diminish the recovery time from a MA that saturates the input, some systems possess a switch connected to the input node [72], [73]. As the system detects the saturation event, it closes the switch, thus providing a low-impedance path to ground. Later, the switch is reopened and the high-impedance input is re-established. During the discharge process, the overall input impedance is low and the signal quality is reduced; however, the amount of information lost is smaller than when waiting for the node to discharge through R_{in} (τ).

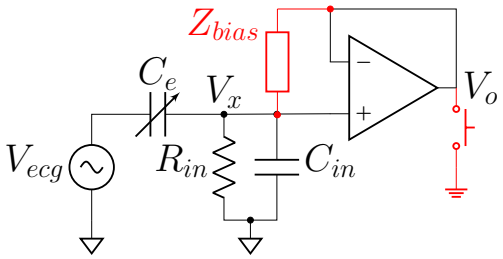

Figure 2.13: High-input impedance buffer with discharging switch

The addition of a switch to the input node may reduce the input impedance. To avoid this, the circuit of Fig. 2.13 was proposed by [74], where Z_{bias} is a resistor or counter-diodes. In normal operation, Z_{bias} is bootstrapped, thus the input impedance is not affected. When a large artifact is sensed, the switch is closed, providing a low-impedance path to ground, and the non-inverting input discharges through Z_{bias} and the switch [74].

2.4.5 Through-Body Feedback

This technique, shown in Fig. 2.14, takes the signal from a voltage follower output in a single channel of the cECG and feeds it back to the human body [75]. This method relies on the feedback path having low impedance to avoid voltage division with the body-to-ground impedance. In [75], a simple wire was used to connect the output to the body. Hence, a unity gain positive feedback is formed, bootstrapping the human body and the input node. As a result, the voltage in a point of the human body and in the input node are the same; and no current flows through the electrode, avoiding voltage drop.

2.4.6 MA Removal with Capacitance Measurement

This MA removal method is not an all-analog solution, yet the compensation itself takes place in the analog domain. It was identified by [76] that when a movement happens, the variation of C_e is correlated with the large voltage artifacts. To optimize the analog-to-digital converter's dynamic range and reduce its resolution and power consumption, a system was proposed that measures electrode impedance and generates a signal similar to the large

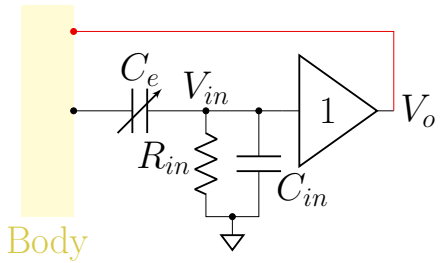

Figure 2.14: Feedback proposed by [75]

MA voltage artifact [73], [77]. A simplified block diagram is depicted in Fig. 2.15, where "C_e *meas*" estimates the electrode capacitance.

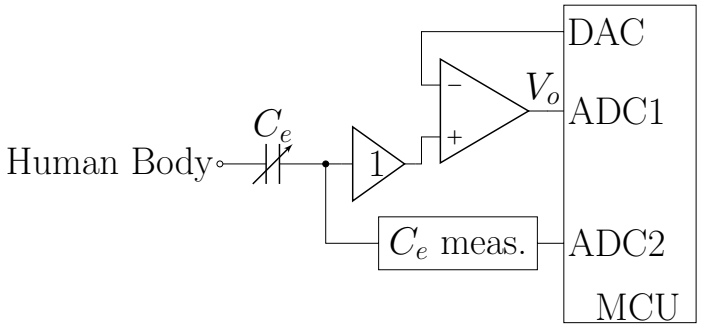

Figure 2.15: MA removal with electrode capacitance measurement

To accomplish that, the measured cECG signal in a single channel is applied to the non-inverting input of an instrumentation amplifier. Both the electrode impedance and cECG are measured and sent to a microcontroller, where a least mean squares algorithm creates a signal similar to the voltage artifact. Lastly, this correction signal is fed back to the instrumentation amplifier, removing a large portion of the MA [73].

2.4.7 Common-Mode Cancellation

Common-mode cancellation circuits are essential in biopotential acquisition to eliminate interference such as the power line induction (e.g. 60 Hz). Moreover, by reducing these undesired common-mode signals, MAs can also be suppressed indirectly. Therefore, reviewing the most popular topologies for common-mode interference reduction is necessary.

2.4.7.1 Low Impedance Path

The simplest technique to reduce interference from V_{line} is to provide a low impedance path to ground [55]. It is implemented by applying an electrode to the right leg with an impedance to ground. Hence, the overall impedance between body and ground is reduced,

increasing the voltage division computed by (2.4). For cECG, a capacitive electrode must be used, thus the low-impedance path is modeled as a capacitor to ground in parallel with C_{bg} and C_{iso}. This simple technique improves 60 Hz suppression, yet it is not as effective as the active techniques presented next.

2.4.7.2 Driven Right-Leg

The driven right-leg (DRL) is a well-known circuit in biopotential measurement that reduces the common-mode voltage by feeding back into the body an amplified and inverted version of the common-mode signal. Figure 2.16 shows an electrical model for a cECG system considering the parameters that affect the common-mode voltage in the body and the DRL circuit (in red lines). Its working principle also relies on reducing the impedance from body to ground and thus making the voltage division seen by V_{line} greater, attenuating the common-mode voltage picked by the electrodes [78]. This circuit is very popular for standard ECG acquisition devices.

In cECG it can be harder to implement because the feedback electrode also possesses a high coupling impedance. That makes the feedback loop difficult to stabilize. Moreover, it needs a swing compatible with the common-mode levels present in cECG, which are greater than in ECG) [8]. However, the DRL can reach stable operation by dominant pole compensation at a cost of fixed CMRR [56] and it may show similar performance to the DRL circuit with wet electrodes [13].

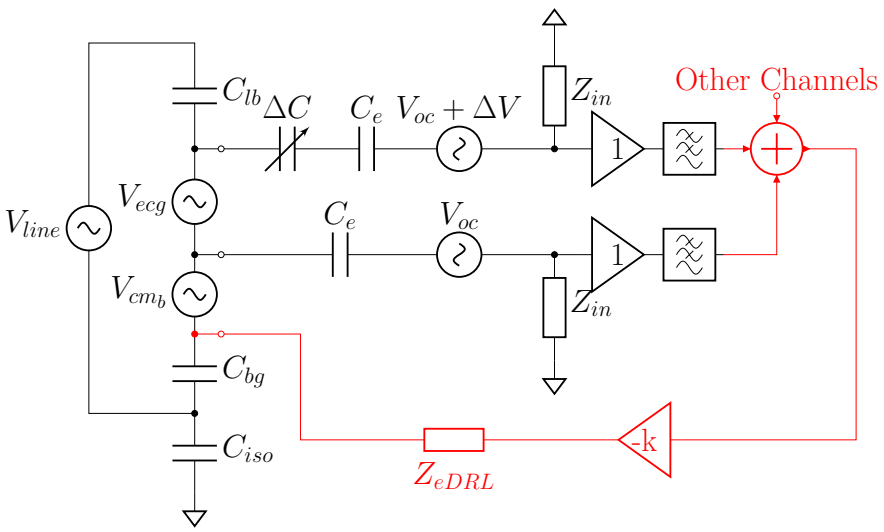

Figure 2.16: DRL

Different from the DRL presented in Fig. 2.16, Guermandi *et al* [79] use the common-mode voltage from a measuring electrode to drive the circuit common (circuit ground/com-

mon is different from real ground - earth). They claim that this circuit eliminates the need for the feedback electrode and it also increases the overall CMRR, because it does not suffer from the same severe instability issues.

2.4.7.3 Common-Mode Shunt-Feedback

The common mode shunt-feedback works by applying a current source to the input node, which sinks the common mode current arriving at that node. This technique is less common than the DRL, thus it still does not have a standard terminology, and may be referred to differently in other works.

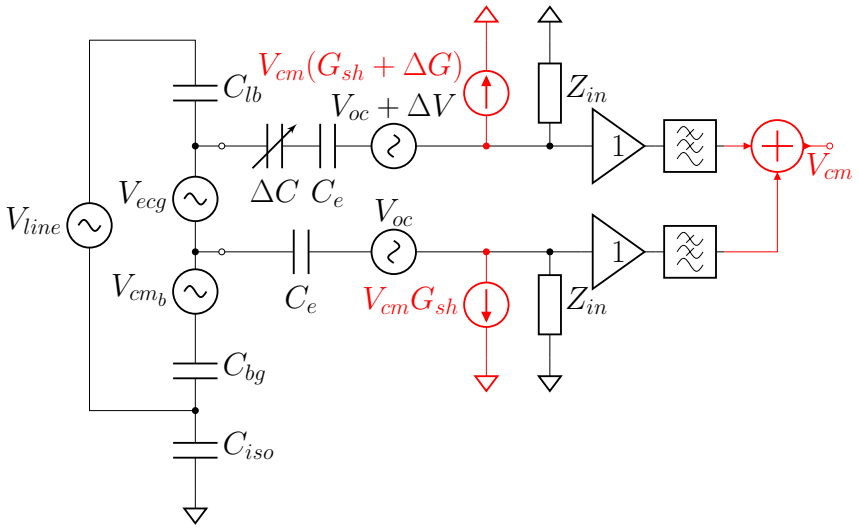

Figure 2.17: Common-mode shunt-feedback

Figure 2.17 shows the schematic of the common-mode shunt feedback. The voltage controlled current source in the top electrode branch has an additional source of error, the gain mismatch ΔG. Another drawback of this topology would be the output impedance of such current sources, because they are in parallel with Z_{in}. These impedances would also present mismatch, but this effect is already modeled by ΔC. In [80] these mismatches were modeled and it was found that they mainly affect a DC reference for common-mode (which in this case is 0) and they proposed a solution by modulating the current sources.

2.4.7.4 Feed-Forward CM Cancellation

The feed-forward common-mode cancellation has a few variations, yet its working principle is based on sensing the common-mode voltage just after the coupling interface and actuating at the amplifier input node. This technique shows improved performance in relation to feedback techniques regarding simplicity, CMRR bandwidth and stability [22], [61].

One group uses as feed-forward the subtraction principle of instrumentation amplifiers, then the signal from the electrode is applied to one input and the common-mode in the other input [22], [61]. Thus, only the differential input is amplified. However, this technique is not that effective as source impedance increases, because of the attenuation of the CM feed-forward signal.

Another possibility of feed-forward common-mode elimination was developed in [81]. In this case, the common-mode is sensed just after the electrode and fed in a forward node at the input of a chopper amplifier. Yet, this technique also fails in capacitive bio-potential measurements because the common-mode sensing circuit would create a low impedance path before the amplifier's input, reducing the signal amplitude.

2.4.7.5 Summary of Boosting Techniques

Method	Benefits	Drawback	Recommended Application
Capacitance neutralization	Compensation for amp. and PCB capacitances	Fine tuning δ (accurate resistors)	Applications with low electrode capacitance
Bootstraping and Shielding	Reduces input cap., simplicity to implement	Fixed compensation, Difficult with discrete components	All PCBs, integrated amplifiers
Bootstrapped bias	Improves input resistance	Inductive behavior and oscillation	Applications with very low cut-off frequency
Channel mismatch with reference signal	Equalizes channel gains	Adds leakage to the input node	Application with high electrode capacitance
Series negative impedance	Decreases overall coupling capacitance	Preliminary results, fixed compensation	Applications with low capacitance changes
Switch	Fast discharging	Information losses during discharge	Applications with high amounts of MA
MA removal with capacitance meas.	Compensates voltage spikes from capacitance changes and triboelectricity	Requires ADC, INA and microcontroller	Applications without power and area constraints
Common-mode feedback	Indirectly remove MA, Reduces common mode interference	Requires multiple channels	All

Table 2.3: Summary of boosting circuits, benefits, drawbacks and preferred applications

Table 2.3 summarizes some of the reviewed boosting circuits. In addition, Appendix A shows the importance of the bootstrapping and neutralization circuits in avoiding voltage division with the input capacitance, as well as the dependence of the low cut-off frequency on the electrode capacitance value.

Chapter 3

MA Model

TENGs are energy-harvesting devices able to generate electricity from the repetitive contact and separation (or rubbing) of different objects. They usually consist of two metallic electrodes separated by one or more dielectric layers. Similarly to MAs in capacitive electrodes, TENGs' working principle is based on contact electrification and varying capacitances.

In this work, TENG models will be used as a starting point to introduce an improved MA model for biopotential acquisition with capacitive electrodes. The first step is to revisit the equations for longitudinal (electrode sliding over the skin) and transverse (electrode creates an air gap with the skin) motions [27], [51], [82], [83]. The text of this chapter is based on our original paper that is under review, which was presented in the Introduction as "Paper C".

3.1 Development

Fig. 3.1 represents a movement at the electrode-skin interface: d_{die} is the thickness of the dielectric, l and w are the length and width of the electrode and σ_c is the charge density on the electrode surface. Before the motion, the skin and the dielectric are in contact and they exchange charges reaching equilibrium. Thus, the contact surfaces of the skin and dielectric present opposite charge density. Once the two surfaces are separated, charges on the skin will be able to move and the total charge on the skin is given by $Q_{skin} = \sigma_c wl$.

Once a longitudinal motion of length $x(t)$ or a transversal motion of height $y(t)$ takes place, the dielectric maintains the same charge density, but a charge Q in the skin flows back to the electrode. Hence, the total charge on the skin becomes $\sigma_c wl - Q$. Albeit the return path from the skin to the electrode is not shown in Fig. 3.1 and Fig. 3.2, it generally consists of the earth's ground and the circuit's ground, which are separated by the supply's isolation

impedance as shown in Fig. 3.3. Note that at this stage, the derivation only requires that a return path exists but the exact path is not needed.

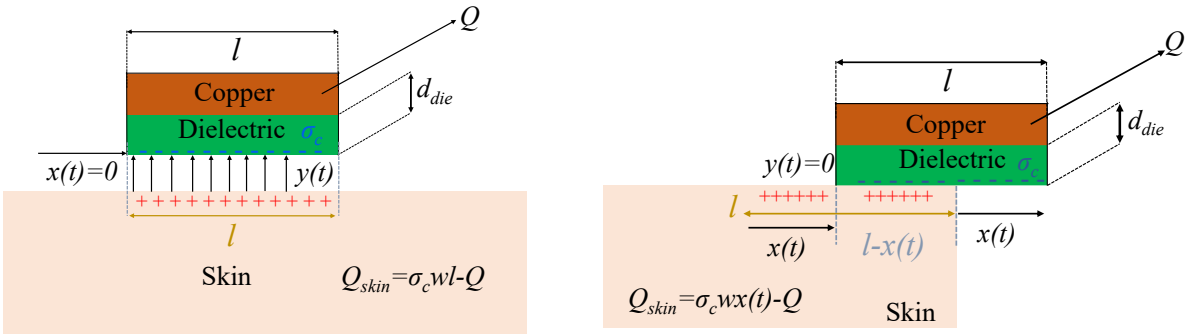

(a) Representation of a transverse MA (b) Representation of a longitudinal MA

Figure 3.1: Electrode motion in a) transverse and b) longitudinal directions

Assuming there is no charge injection, the sum of all charges is zero. Note that based on TENG models, only a portion of the skin with length l is electrified during the contact. Further, the edge effect is neglected and the electric field is considered uniform and perpendicular to each surface. Then, the total voltage between two surfaces can be modeled as: $V_m = E_m d_m$, where $E_m = {}^{\sigma_m}/_{\varepsilon_m}$ and $\sigma_m = {}^{Q_m}/_{S_m}$, m refers to the material being assessed, V_m is the voltage drop between the material m and a reference (e.g. m is the skin, reference is the copper), E_m is the electric field, d_m is the distance, ε_m is the permittivity of m and σ_m is the charge density (charge Q_m over area S_m) on the surface of m.

The identity $V = -{}^{Q}/_{C_e(t)} + V_{tribo}$, allows the extraction of a lumped model comprising a time-varying capacitor (C_e) and a voltage source (V_{tribo}), which are shown in Fig. 3.3. These two values can be obtained with the short and open-circuit tests: the short-circuit test assumes that the voltage drop between skin and copper is 0, leading to C_e, while the open-circuit test assumes no current flow and hence the total voltage is given by V_{tribo}.

3.1.1 Transverse and Longitudinal Models

Artifacts due to motion in the y direction only (transverse MA, shown in Fig. 3.1a) correspond to the electrode's copper voltage (relative to ground) due to the electric field from each interface [50], [82]:

$$V = \frac{1}{wl\varepsilon_0}\left\{-Q\left[\frac{d_{die}}{\varepsilon_{r_{die}}} + \frac{y(t)}{\varepsilon_{r_{air}}}\right] + \sigma_c wl\left[\frac{y(t)}{\varepsilon_{r_{air}}}\right]\right\} \tag{3.1}$$

where ε_0, $\varepsilon_{r_{air}}$ and $\varepsilon_{r_{die}}$ are, respectively, the vacuum permittivity, the relative permittivity of air and the relative permittivity of the dielectric layer, w and l are the width and length of the electrode, σ_c is the charge density on the electrode surface, Q is the amount of charge transferred from the skin to the electrode during the motion and $y(t)$ the height of the y motion.

The skin-air interface (surface of the skin) has a charge density of $\sigma_c - Q/S$, where the skin's electrified area is $S = wl$, with the electric field passing through air and dielectric. The air-dielectric interface (bottom surface of the dielectric) has a charge density of $-\sigma_c$ whereas the electric field is within the dielectric. Thus, finding expressions for V_{skin} (voltage due to skin's charges) and V_{die} (voltage due to the dielectric's charges), and summing them, leads to (3.1).

The open-circuit test considers that a flow-back path for Q is nonexistent (skin and electrode perfectly isolated), thus $Q = 0$, while the short-circuit evaluation connects the skin and the copper through a short circuit, thus $V = 0$. From these two steps, the equations for V_{tribo} and C_e can be deduced:

$$V_{tribo} = \frac{\sigma_c y(t)}{\varepsilon_0 \varepsilon_{r_{air}}} \tag{3.2}$$

$$C_e = \frac{Q}{V_{tribo}} = wl\varepsilon_0 \left[\frac{\varepsilon_{r_{air}} \varepsilon_{r_{die}}}{y(t)\varepsilon_{r_{die}} + d_{die}\varepsilon_{r_{air}}} \right] \tag{3.3}$$

For the longitudinal motion (x direction only) shown in Fig. 3.1b, the example of a sliding-mode TENG [27] is considered. Therefore, $y(t) = 0$ and $x(t) \neq 0$.

When the electrode slides, at the overlapped region, the dielectric and the skin have opposite charge densities. Further, the dielectric's charge density is constant throughout its area. If the copper has a charge Q, then the skin has an amount of free charge $\sigma_c w x(t) - Q$. The region of interest is where the skin and the electrode overlap, thus the area is given by $w(l - x(t))$.

The resulting equation describing the electrode's copper voltage, in the case of a longitudinal movement, can be modeled as:

$$V = \frac{\sigma_c x(t) w - Q}{\varepsilon_0 \varepsilon_{die} w[l - x(t)]} d_{die} \tag{3.4}$$

From this equation, a capacitance and a voltage source can be derived (lumped model) [27]. Note that the larger the horizontal movement $x(t)$ is, the more charge is available on the skin surface, while the overlapped area becomes smaller. The limit of the model is given by

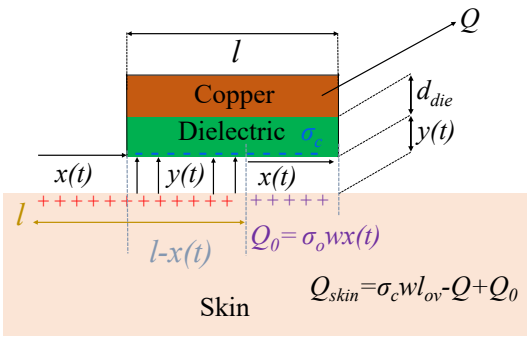

Figure 3.2: Representation of a motion artifact in 2 directions and contact-chargeable extended skin

the case of $x(t)$ approaches the length of the electrode l, for which V tends to infinity: this limitation is caused by the fact that the model only considers perpendicular electric fields within the electrode surface and no fringe electric field is accounted for.

3.1.2 Proposed Model

The model represented in Fig. 3.2 considers motions in two directions and new parts of the skin. It is derived by accounting for electric fields perpendicular to the surfaces only. Finding the skin charges (3.5) is the first step to derive the proposed model's general equation (3.6). The resulting charge on the skin depends on whether the motion ceases contact with the skin or not. To include the possibility of the two different cases in the model, a binary contact variable k_{co} was introduced: $k_{co} = 1$ when dielectric and skin are in contact and $k_{co} = 0$ when an air gap is formed. Another variable added to aid in the derivation is $l_{ov}(t) = l - x_a(t)$, the length where dielectric and skin overlap.

Previous TENG-based models consider only the case in which the electrode slides into an empty area. That is not always true for cExG, as the body area is very large, thus often the electrode slides into a new section of skin (shown in Fig. 3.2). To include this case and complete the MA model, the skin's length is extended, whereas it may have some stored charges Q_0. While the electrode and the skin are in contact, both show a charge density of $\pm\sigma_c$, while the copper is discharged and the remaining part of the skin has an amount of charge Q_0, assumed to be uniformly distributed with charge density σ_0. This assumption will be further confirmed in the experimental validation in the results section.

When the electrode moves away from the skin, with a vertical motion of $y(t)$ and horizontal motion $x(t)$, the charges on the skin will rearrange to reach the equilibrium, and some charges Q flow back to the copper. Therefore, the total charge on the skin is given $Q_{skin} = \sigma_c w l - Q + Q_0$, and the area where skin and electrode overlap is always l.

The role of $x(t)$ is different from the longitudinal-only MA. To model both effects, sliding over the air and the skin, two variables are required: $x_s(t)$ (distance over the skin) and $x_a(t)$ (distance over the air). By using the new variable, k_{co} (existence or absence of contact) and $l_{ov}(t)$ (length of the electrode and skin overlap), one can rewrite:

$$Q_{skin} = \sigma_c w(l - l_{ov}(t)k_{co}) - Q + \sigma_0 w x_s(t) \tag{3.5}$$

If the electrode moves and there is still some contact area, then the first term in (3.5) becomes $\sigma_c w x_a(t)$. However, if the electrode loses contact, the first term in (3.5) is $\sigma_c w l$. The skin's charge density is found by observing that the charges are within an area of $w l_{ov}(t)$. The air-dielectric interface will contribute only if $y(t) \neq 0$ and $k_{co} = 0$ and the amount of charge is proportional to the overlap area. Further, by calculating the electric field from the skin and dielectric to the copper, the model with additional skin area and charges is derived:

$$V = \frac{1}{\varepsilon_0 w l_{ov}(t)} \left\{ [-Q + \sigma_0 w x_s(t)] \left[\frac{d_{die}}{\varepsilon_{r_{die}}} + \frac{y(t)}{\varepsilon_{r_{air}}} \right] + \sigma_c w \left[\frac{d_{die}(l - l_{ov}(t))}{\varepsilon_{r_{die}}} + \frac{y(t)(l - l_{ov}(t)k_{co})}{\varepsilon_{r_{air}}} \right] \right\} \tag{3.6}$$

The next step is to extract the parameters V_{tribo} and C_e from the identity as done before. Thus, by applying the open and short circuit tests to (3.6), $C_e(t)$ and $V_{tribo}(t)$ are obtained. In (3.6), k_{co} becomes redundant because it is multiplied by $y(t)$. Thus, in (3.7), $y(t)(l - l_{ov}(t)k_{co})$ is substituted by $y(t)l$. Similarly, $l - l_{ov}(t)$ is replaced by $x_a(t)$.

The capacitance expression (3.8) is verified through simple parallel plate capacitor theory. The plate area is the constant width (w) times the length of skin-electrode overlaps ($l_{ov}(t)$), whereas the dielectric/air separates the two plates. Thus, if $x_a(t) = 0$ (no motion over the air) the capacitance changes only due to $y(t)$.

$$V_{tribo}(t) = \frac{\sigma_0 x_s(t)}{\varepsilon_0 l_{ov}(t)} \left[\frac{d_{die}}{\varepsilon_{r_{die}}} + \frac{y(t)}{\varepsilon_{r_{air}}} \right] + \frac{\sigma_c}{\varepsilon_0 l_{ov}(t)} \left[\frac{d_{die} x_a(t)}{\varepsilon_{r_{die}}} + \frac{y(t) l}{\varepsilon_{r_{air}}} \right] \tag{3.7}$$

$$C_e(t) = \frac{\varepsilon_0 w l_{ov}(t)}{[d_{die}/\varepsilon_{r_{die}}] + [y(t)/\varepsilon_{r_{air}}]} \tag{3.8}$$

The proposed V_{tribo} model (3.7) adds a fundamental feature, increased skin length. For example, in (3.4), if $x(t) = l$ (thus $l_{ov} = 0$), then $V \to \infty$. Physically, $l_{ov}(t) = 0$ means that the parallel plate capacitor does not exist anymore. When $\sigma_0 w x_s(t)$ is introduced, a

new source of triboelectricity is established, which is proportional to the motion's length. In the case of a motion of distance x_s over the skin, σ_o is replaced by σ_c to represent the contact electrification of the new area, while still accounting for charges from the previously electrified area.

3.1.3 Circuit Model

Fig. 3.3 describes the components of a simplified biopotential acquisition with a capacitive electrode. V_{bio} is the body's potential to be measured on the skin's surface, its lower terminal is connected to the Earth (0 V). The proposed MA model is included as a variable capacitor (C_e) defined by (3.8) and a triboelectric voltage source (V_{tribo}) defined by (3.7). The circuit is composed of an operational amplifier (U1) connected in a buffer configuration. R_{in} is the electrode's input resistance and is connected to the circuit ground, which is not necessarily 0 V.

Fig. 3.3 assumes that the input capacitance is much smaller than C_e, hence, it can be disregarded. In practice, this was achieved by using the capacitance neutralization circuit and bootstrapping. Moreover, the model considers the capacitive component of the electrode to be dominant compared to the skin impedance. The electrode employed in this work uses the PCB's solder mask as the dielectric and it directly contacts the skin. To include clothing as a dielectric, both its capacitive and resistive parts should be accounted for. The aforementioned return path between body and electrode is established by R_{in}, the supply's isolation impedance Z_{iso}, and many other elements that are unique to each implementation and are not accounted for in this model.

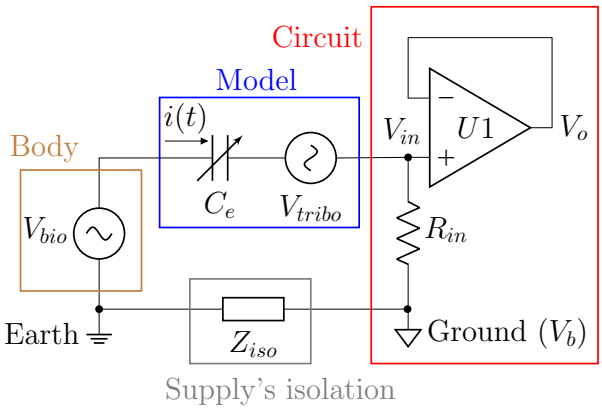

Figure 3.3: Simplified capacitive electrode with motion artifact model

From the circuit model of Fig. 3.3 the exclusion of edge effects is justified. Although fringe fields are significant for large transverse motion ($y(t) \approx l$), the voltage spike decays

quickly because C_e is small. Then, the most concerning part of a large transverse motion is the voltage division between C_e and the amplifier's input capacitance. However, many techniques exist to reduce the input capacitance, and in a proper design, significant voltage division should not take place. Therefore, including the edge effect substantially increases complexity for a small gain of accuracy. In longitudinal motion, the distance between plates is d_{die} (35 µm) and it is much smaller than l (≈3 cm), thus fringe fields are negligible.

To evaluate only the influence of an MA in V_o, V_{bio} is neglected. Furthermore, it is assumed that Z_{iso} is a short circuit, which is achieved in practice by connecting a low-impedance electrode from the ground to the human body. Thus, the voltage drop across C_e and V_{tribo} is equal to the voltage drop across R_{in} and the ground voltage (V_b):

$$-\frac{Q}{C_e(t)} + V_{tribo}(t) = V_b + i(t)R_{in} \tag{3.9}$$

Knowing that the current is $dQ(t)/dt$ and differentiating (3.9), one obtains:

$$i(t) + R_{in}\left[C_e(t)\frac{di(t)}{dt} + i(t)\frac{dC_e(t)}{dt}\right] = C_e(t)\frac{d[V_{tribo}(t) - V_b]}{dt} + [V_{tribo}(t) - V_b]\frac{dC_e(t)}{dt} \tag{3.10}$$

3.1.4 Simulation and Experiment Setup

Equations 3.7 and 3.8 were numerically simulated by substituting known constants with their respective values. The permittivity of vacuum (ε_0) is 8.854×10^{-12} F/m, the relative dielectric constant of air ($\varepsilon_{r_{air}}$) is 1. The relative dielectric constant of the solder mask ($\varepsilon_{r_{die}}$) is 3.5 and its thickness (d_{die}) is 35 µm. The electrode is a square with a side length of 2.97 cm. Equally sized arrays describe the y , x_a, and x_s motions as a function of time. It is assumed that σ_o=σ_c when the electrode slides over the skin, whereas σ_c is estimated with the following equation:

$$\sigma_c = (\eta_{skin} - \eta_{die}) * \gamma \tag{3.11}$$

where η is the charge affinity obtained from the triboelectric series [52] in C/J, while γ is the energy (or work, W) necessary to separate the contacting surfaces over the electrode's area ($w * l$) given in J/m^2.

In transverse motion, the work is related to adhesion energy, and in longitudinal motion, the work is given by the friction of the skin and electrode. Capacitive electrodes are used in a

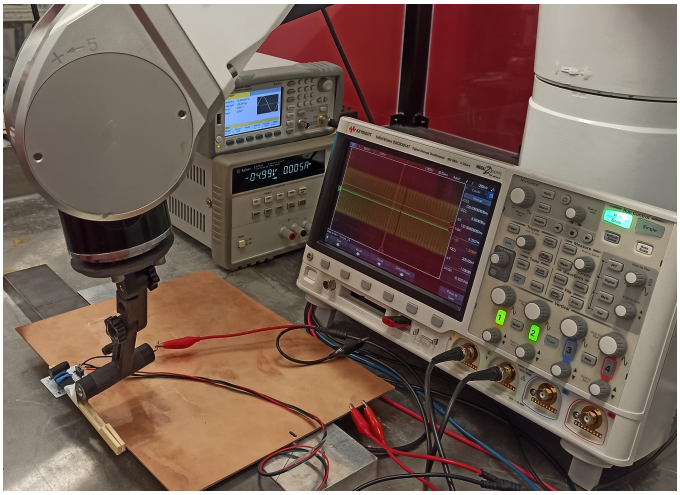

Figure 3.4: Picture of the measuring setup, where the robot arm moves the electrode.

wide range of applications, and the motion characteristics are unique to each case. Adhesion energy of human skin is reported as dozens of $\mathrm{mJ/m^2}$ (adhesion force is in decimals of mN) [84] while the friction force is in the range of hundreds of mN [85]. Hence, although accurate modeling is complicated, the numerical simulation can be performed with a fixed value of W and here 50 mJ was used. This value is a rough estimation accounting for reported friction force, displacement, and contact area. The charge affinities of dry skin and of solder mask (epoxy) are 30 nC/J and -32 nC/J respectively.

The measurement of MA was performed with a simple capacitive electrode, the electrode dimensions are the same as those used for simulation, and the measured input resistance is 2.2 GΩ. The test setup employed a bare copper board covered with a layer of box sealing tape. This tape has a comparable charge affinity to oily skin according to the triboelectric series [52]. A 10 Hz signal was injected into the copper board to serve as a reference signal. A robot arm (Stäubli TX2-90L) was used to move the electrode and the instrumentation was placed next to it as shown in Fig. 3.4.

3.2 Results

3.2.1 Simulations

Figure 3.5 displays the computation of the electrode capacitance (3.8) and the triboelectric voltage (3.7) responses to different types of motion. The movements' lengths were logarithmically varied between 0.1 mm and 4 cm with 10 samples per decade. Figures 3.5a and 3.5b show the electrode capacitance and resulting triboelectric voltage, respectively.

While changes in C_e have a significant influence on the acquired signal, they are solely

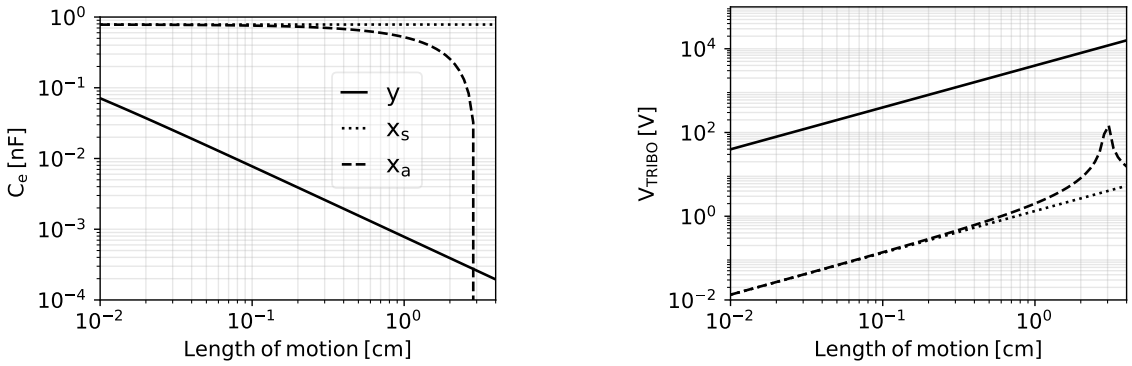

(a) Capacitance as a function of motion

(b) Triboelectric voltage as a function of motion

Figure 3.5: Computation of the electrode capacitance (3.8) (a) and the triboelectric voltage (3.7) (b) for 3 types of unidirectional motion

dependent on the geometrical configuration of the electrode, thus easily predictable and not sufficient to describe the overall behavior of the resulting MAs. The triboelectric voltage is the most complex factor in MAs. That is, V_{tribo} is a function of charge density, hence, it relies on the dynamics of the work W necessary to separate the two surfaces initially in contact. The resulting MAs visible in the recorded signal are a trade-off between the growth ratio of V_{tribo} and the discharge time of the varying C_e as described in (3.10). Thus it is important to know the individual behavior of C_e and V_{tribo}.

The capacitance analysis (Fig. 3.5a) is straightforward. For a horizontal motion x_s along the skin, the electrode remains constant at 780 pF because the capacitor's area and dielectric thickness do not change. A motion over the air x_a begins to cause considerable capacitance change when the electrode's area not overlapping with the skin is large. In other words, x_a must be at least 10% of the electrode's size to change the capacitance significantly. Once x_a is greater than the electrode's side length (≈ 3 cm), the plates are not parallel anymore and the resulting capacitance is equal to zero. The perpendicular motion y leads to more severe capacitance changes: if an air gap as small as 0.1 mm is created, the electrode capacitance drops from approximately 780 pF to 71 pF, and a y motion of 1 cm leads to a capacitance of 0.78 pF.

The results in Fig. 3.5b are based on the assumption that all motion required 50 mJ to start. Although on a logarithmic scale V_{tribo} is linear for movements y and x_s, the physics behind the generation of these artifacts is different. A movement in y direction causes an increase in voltage because of the increased distance between the charged plates ($V = E * d$). Differently, a movement in x_s does not vary the distance between plates, but causes more area on the skin to be electrified, thus changing the overall charge on the skin. Finally, a

motion in x_a leads to a partial loss of contact area causing an increase in charge density in the portion of the area still in contact with the skin, which induces a sharp increase in triboelectric voltage.

The proposed MA model suggests that for the same amount of work, transverse motion generates more triboelectricity than longitudinal motion. However, in practice, a longitudinal motion likely requires more work than a transverse motion. For example, consider the case of a cECG mattress where the person is lying down with the back over the electrodes. A longitudinal motion (sliding the back to a new position) involves the whole weight of the torso pressuring the electrodes, thus, there is a high friction force acting against the motion. On the other hand, a transverse motion revolves around losing contact with the electrode, thus the work done over the electrode is mostly due to the adhesion energy, a smaller force.

The results shown in Fig. 3.5 are the computation of (3.7) and (3.8) only. However, in a biopotential acquisition, these two effects merge and appear as voltage artifacts, which are predicted by simulating (3.10). Yet, Fig. 3.5 shows how each type of motion affects the electrode capacitance and the triboelectric voltage, which serves to explain the MA dynamics. The subsequent results (Fig. 3.6 to Fig. 3.10) display the simulated/measured MA created by movements taking place at 1 s. Note that for motion over the air, x_a, a motion length of 4 cm is larger than the electrode's side (≈3 cm), thus the electrode does not work, and results cannot be obtained.

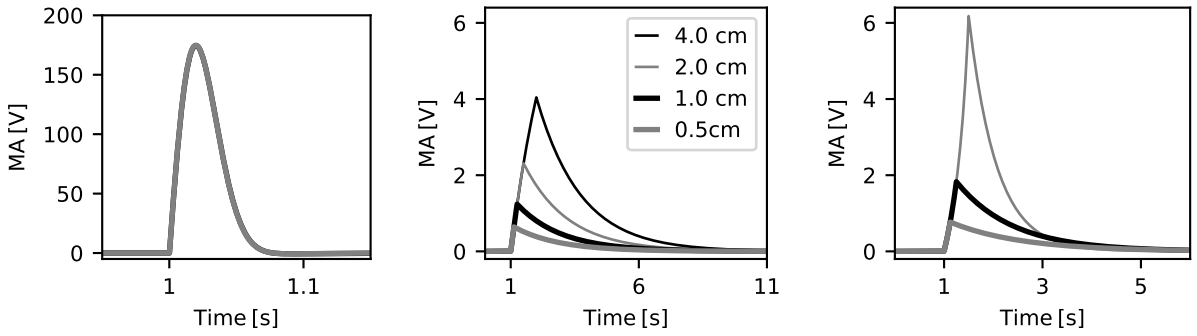

(a) y motion (b) x_s motion (c) x_a motion

Figure 3.6: Numerical solution of (3.10) for three types of motion with constant speed, but different traveled distances

Fig. 3.6 shows the simulated MAs generated over time for three lengths of motion at constant speed (4 cm/s): 0.5 cm, 1 cm, 2 cm and 4 cm. The MA generated by a y motion (Fig. 3.6a) is the same regardless of the traveled distance. For all four simulated lengths of y, the peak voltage, rising time, and falling time matched. To explain this behavior it must be taken into consideration that, while the traveled distance defines the value of C_e and V_{tribo},

it is the motion's speed that determines how fast the transition from initial to final values happens. In all cases, V_{tribo} should be above 10 kV according to Fig. 3.5b, however, the large decrease in electrode capacitance with only a few mm of motion drastically reduces the time constant. Thus, the node discharges within 0.1 s, which is faster than the time needed to complete the movements, resulting in the same amplitude of MAs for all y.

In the case of longitudinal motions, the simulated waveforms for the electrode sliding over the skin (x_s) and the electrode sliding from the skin over to the air (x_a) appear to be similar. Nevertheless, important differences are present: for a traveled distance of 2 cm, the MA's amplitude caused by a motion x_a (Fig. 3.6c) is more than twice the amplitude of the MA generated from a motion x_s (Fig. 3.6b); meanwhile, for shorter movements, the amplitudes for x_s and x_a types of MAs are closer. These observations agree with Fig. 3.5b: as the traveled distance of x_a approaches the electrode's length, the triboelectric voltage spikes.

Fig. 3.6b and Fig. 3.6c also differ in time constants. In Fig. 3.6b, all curves present a 1.7 s time constant (discharge by 63%), while in Fig. 3.6c the time constants are 0.50 s (2 cm), 1.1 s (1 cm), and 1.4 s (0.5 cm). This can be explained by the fact that, for x_s motions, the parallel plate capacitor area does not change whilst, in the case of x_a motions, the capacitance decreases as the traveled distance increases, leading to a significant decline in time constant. Similarly, the rising slope for x_a MAs becomes steeper with time.

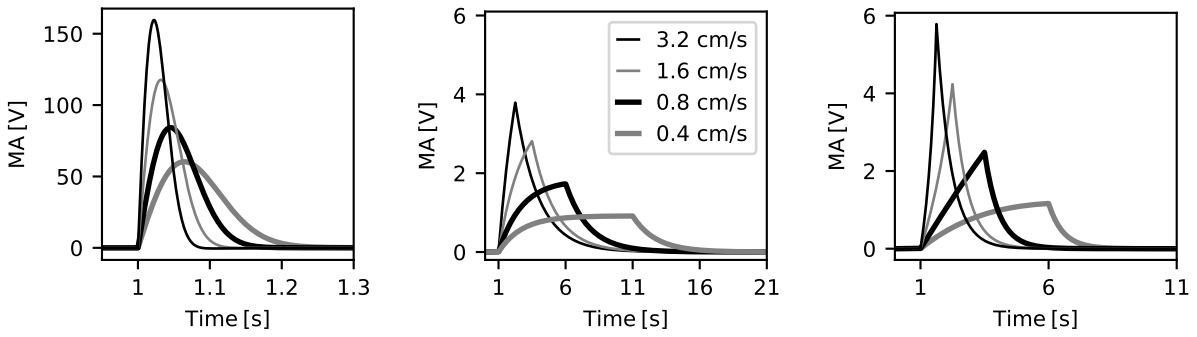

(a) y motion (b) x_s motion (c) x_a motion

Figure 3.7: Numerical solution of (3.10) for three types of motion with different speeds, but constants traveled distances

Fig. 3.7 shows MAs for speeds ranging from 0.4 to 3.2 cm/s over constant distances. The traveled distances were 4 cm for y and x_s motions and 2 cm for x_a motion. In the MAs displayed in Fig. 3.7a, the trade-off between the growth ratio of V_{tribo} and the discharge time imposed by C_e is illustrated. That is, faster motions lead to higher peaks because

the traveled distance is higher, however, the time constant decreases faster and the MA's duration is shorter.

From the longitudinal MA simulation, due to the overlap area reduction, x_a motion (Fig. 3.7c) leads to slightly higher peaks and lower settling times compared to x_s motion (Fig. 3.7b). In Fig. 3.7b, the time constant is fixed. Thus, the discharge ratio is constant and the peak depends on the speed of motion which defines how fast the triboelectric voltage rises. Meanwhile, in Fig. 3.7c, the time constant also changes, meaning that faster movements lead to higher and narrower peaks.

3.2.2 Measurements

The measurements on a test setup followed the same principle as the simulations. Hence, the measurements in Fig. 3.8 had a constant speed for different lengths of motion and Fig. 3.9 accounted for different speeds with the same traveled distance. The motions happen at 1 s. The limitation of our experiment is that the robot arm does not comprise a pressure sensor and the speed is displayed as a percentage of the maximum speed. The estimated maximum speed (100%) of the robot's arm is 16.7 cm/s.

In Fig. 3.8 and Fig. 3.9, the objective is to verify the behavioral dependency on traveled distance and speed according to the model equations, not overall accuracy. Further, speed, force, and charge affinity do not match, thus the MA amplitude is different between simulation and measurement. Direct comparison between predicted and measured MA is made in Fig. 3.10.

The electrode's working status is monitored with a reference signal injected on the copper board (see Fig. 3.4), hence a 10 Hz sinusoid is overlapped with the MA. In Fig. 3.9b and Fig. 3.9c the reference signal was filtered out for better visibility. Moreover, the electrode's amplifier is supplied with ± 5 V, thus it saturates for strong MA.

Fig. 3.8a displays the measured MA for y motion, and the results are as expected from simulations. The curves overlapped because the rate of capacitance change is the same, and the system discharges before reaching the end value of capacitance and triboelectric voltage. The flat top indicates that the triboelectric voltage saturated the operational amplifier's input.

Fig. 3.8b shows that x_s motion also led to an MA response behavior that matches the simulation. The two cases with larger traveled distances saturated the amplifier, whereas for 1.0 cm the peak reached the edge of saturation. For the shortest motion, 0.5 cm, the peak was of 4 V. Hence, the measured responses showed larger MA for longer lengths of motion and equivalent settling times.

Similarly, the x_a MA response shown in Fig. 3.8c followed the simulated curves. The MA peak in the x_a case is larger than in x_s, observed as the saturated 0.5 cm. Moreover, longer motions led to shorter discharging times because the capacitance is reduced and so is the time constant.

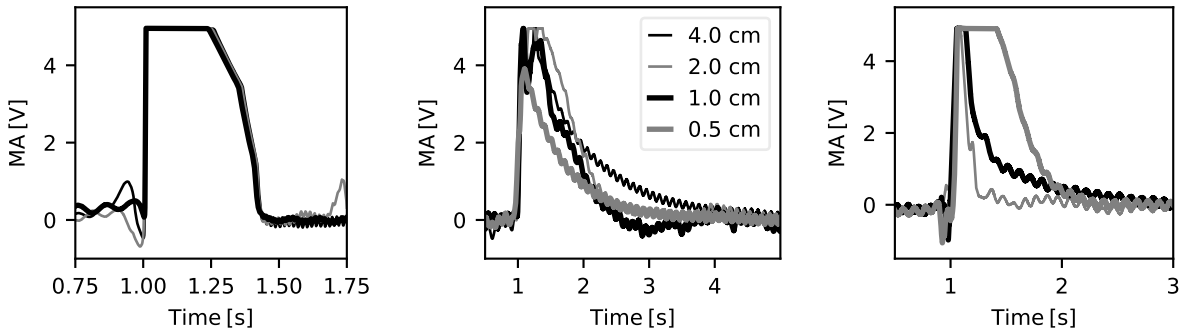

(a) y motion (b) x_s motion (c) x_a motion

Figure 3.8: Measured MA on a test setup with constant speed and different motion's length

The next measurement is to verify the effect of the speed. Compared to the previous measurement, the contact pressure was reduced to demonstrate non-saturated artifacts. Similarly to the simulation, 4 speeds were tested. Yet, given the robot constraints, the speed for each sample could not be exactly doubled. The results are shown in Fig. 3.9.

The measured y MA shows that as speed increases the amplitude rises while the spike becomes narrower. This behavior follows the trend observed in the simulations presented in Fig. 3.7a. One can also notice that the reference signal's amplitude decreases quicker with faster motion, whereas for the 25 % speed curve the reference signal is unreadable after 1 s, yet still recognizable for the 2% trace. That happens due to C_e entering the range of C_{in} earlier during faster MA. Compared to Fig. 3.8a, the amplitude of MA in Fig. 3.9a decreased due to the smaller contact pressure.

Regarding the two types of longitudinal motion, the measured MA response behavior matched the predictions of the simulations: faster motions lead to higher peaks in both x_s and x_a movements, while slower motions translate in slower rising times. In both Figs. 3.9b and 3.9c one can see more peaks and valleys (transition from positive to negative) than in other measurements. The reason for this noise is the lower pressure between the electrode and the copper boards, which allows more vibration that creates micro y motions and oscillation of speed.

For safety reasons, the same experiment could not be reproduced on real human skin with the use of a robot arm. Thus, to provide a direct comparison between the model

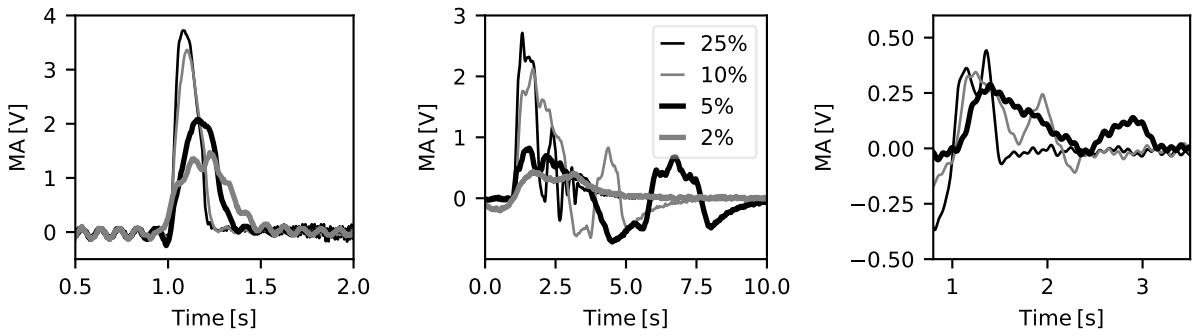

(a) y motion (b) x_s motion (c) x_a motion

Figure 3.9: Measured MA on a test setup with different speeds and constant motion's length

and real measurements on the skin, the motion was performed by hand and a slow-motion camera and a ruler were used to track motion. To remove the influence of V_b from (3.10) and therefore bypass Z_{iso} in Fig. 3.3, the body has to be grounded. Hence, the circuit's ground was connected to the subject's right hand with an Ag/AgCl electrode. For a floating body, one should find the capacitance between the earth and the circuit's ground. In other words, the supply's isolation impedance must be known. Moreover, because we cannot measure the separation energy W (within σ_c), and it is a common variable in (3.7), one can scale it to fit the measurement.

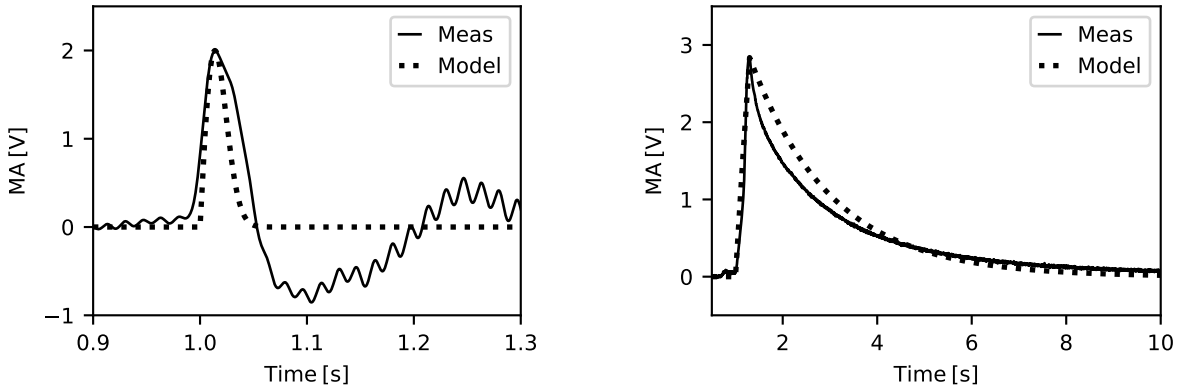

(a) y motion (b) x_s motion

Figure 3.10: MA measured *in vivo* on human skin

Fig. 3.10 shows the comparison between the model and *in-vivo* measurements. The first thing to observe in Fig. 3.10a is the presence of a small 60 Hz component (between 0.9 s and 1 s) even though the body was grounded with the circuit's ground. At 1 s, a y motion took place. The displacement was of 3.5 cm in 0.4 s, and the model used constant speed.

The contact energy W is adjusted to match the peak's amplitude, and the resulting value is 0.34 mJ.

The measured spike length was 0.063 s and the amplitude was 1.99 V, while the predicted spike length was 0.04 s and the amplitude was 1.98 V. After the spike, the model returns to the baseline while the measured MA bounces negatively before returning to an average value of 0 V. Remark that the 60 Hz noise increases until the motion is completed. This is an important phenomenon in y MA, where the 60 Hz is not coupling through the body but through the air directly into the capacitive electrode's input node.

In Fig. 3.10b, an x_s motion with 2.0 cm of length in a 0.3 s interval happened at 1 s. The contact energy was set to 57 mJ so the peaks match at 2.9 V. The measured MA decreased slightly faster than the simulated model right after the peak, and the time constant (63% decrease) was 2.6 s for the measured MA and 3.0 s for the simulated data. The shorter time constant in the measured MA can be explained by subtle changes in the electrode capacitance during the motion.

3.3 Discussion

The simulations of (3.7) and (3.8), considering a fixed 50 mJ contact energy, allowed us to understand the changes in the electrode capacitance and the generation of triboelectricity for three different types of motion. In a transverse (y) motion, C_e and V_{tribo} change linearly in log scale. For longitudinal over-skin motion (x_s), C_e remains constant while V_{tribo} increases linearly in a logarithmic scale. The behavior of MA due to over-air longitudinal motion (x_a) is similar to x_s MA until the over-air length becomes 10% of the electrode's side length. Then C_e and V_{tribo} vary drastically. For the same amount of energy, y is the one type of motion that leads to more V_{tribo}, while x_s is the one with the least V_{tribo}.

The numerical solution of (3.10) showed that the drop in C_e even for the smallest y movement greatly reduces the discharge time. Thus, in most cases, MAs will not reach the same amplitude as V_{tribo} because it discharges before the motion is finished. As the speed of motion increases, so does the peak amplitude, however, the MA duration is shortened. Longitudinal motions have similar waveforms, but the x_a case leads to higher peaks and faster discharging times compared to the x_s case.

The measured MA on a test setup followed the behavior observed in simulations. That is, constant speed motion led to overlapping curves in y motion; stable time constant and increasing peaks with traveled distance in x_s; higher peaks in x_a (compared to x_s) and motion-dependent time constants. The measurements with varying speeds showed that increased speed led to higher and narrower peaks in y MA. While in x_a and x_s motion, the

amplitude and the rise time changed. The constant speed measurements had a higher contact pressure which led to higher MA, while the lower contact pressure in the varying speed measurements allowed the electrode to vibrate and create more peaks in the MA. In some experiments, the measured response showed saturation. This can be simulated by setting a clipping value in (3.10) or avoided by using an operational amplifier that tolerates higher supply voltages.

In-vivo measurements were directly compared with the model's predictions by knowing the total time and traveled distance, and then assuming constant speed. The variable W, related to the energy required to break the inertia or separate the electrode from the skin was scaled so that the MA's peak amplitude matched. The overall behaviors matched for both y and x_s types of motion, but the rising and falling times showed some differences. One reason for the discrepancy in y motion is the initial voltage drop over C_e. Although V_b is ground, the operational amplifier's input presents an offset and the skin naturally contains a DC potential.

Another source of error in the model's simulation is the skin's mechanical properties (viscoelasticity). During initial contact, the pressure stretches and compresses the skin. In the first moments of a y motion, the pressure reduces and the skin goes back to the original state. In this interval, there was motion and change in the skin's charge density, but no air gap. Thus the model will not compute these into MA. Similarly, when an x_s motion happens, the skin is pulled along the motion, and the electrode-skin contact area may change at the microscopic level. The slow oscillation after the y motion is likely caused by hand vibrations when stopping the motion.

The current model assumes that the initial contact and transverse motion are uniform within the electrode's area, which may not be true in practice. To include heterogeneous transverse motion, $y(t)$ should be described as a two-dimensional array, one dimension for time and the other related to a position on the electrode. However, the challenge is to verify such a model as it would require tracking $y(t)$ in multiple points of the electrode. Moreover, our model considers only the PCB's solder mask as the fixed dielectric, while some electrodes can use the clothing as the dielectric, and others may have multiple layers of dielectric. Therefore, the specific dielectric layers of each implementation must be accounted for during the development of the model, yet the working principles are still the same.

Instrumentation uncertainties from the oscilloscope resolution (1 mV per division) and the robot's arm position repeatability (0.035 mm) are negligible compared to the distance traveled (cm range) and MA voltages (V range). The most significant uncertainty is from the ruler used to track the motions on *in-vivo* measurements, where the smallest resolution was 0.1 cm added to the parallax. Moreover, the motion's speed during the *in-vivo* measure-

ment was estimated with a video recording, which requires a human decision of when the movement started and stopped. Also, the lack of information on the initial contact pressure compromises repeatability.

Chapter 4

Through-Body Negative Feedback

As discussed in Chapters 2 and 3, MAs are partially caused by the fluctuation of the electrode capacitance. The change in the current passing through the input node or the voltage division created with the input capacitance can be seen as a gain variation. In electronics, negative feedback is known for desensitizing gains, thus it is a possible technique for reducing MA.

Therefore, in this chapter a through-body negative feedback is proposed for ECG. To establish a feedback, the electrode impedance must be within a closed-loop system. That means, the signal measured by the electrode must be processed and fed back to the body by a second electrode. First, applying negative feedback for each electrode (single-ended) is evaluated. Then, a differential feedback is proposed, where the difference between two channels is fed back.

4.1 Single-Ended Feedback

4.1.1 Development

Figure 4.1 shows a simplified model of the proposed feedback system (cECGf). The feedback branch comprises a series impedance Z_s, a feedback electrode Z_{ef} and a body impedance between the two electrodes Z_{b2}. The other elements are common to the cECG and the cECGf. In the human body, there is a voltage source V_{ecg} (voltage from the heart), and a body impedance from this node to the electrode position Z_{b1}. The body is connected to the measuring device through an electrode with coupling impedance Z_e. This interface includes the skin, the patient's clothing, a layer of insulating material, a layer of conductive material and possibly air gaps. In the electronics side, an amplifier with gain A contains non-ideal elements such as an input impedance Z_{in}, voltage noise (e_n) and current noise (i_n)

sources.

The earth voltage, referred to here as real ground, is not the same as the circuit ground (also known as common). In fact, it is mandatory to include an isolation impedance Z_{iso} (made by the power supply circuit) to guarantee negligible leakage currents through the patient's body, ensuring the patient's safety. It is also relevant that the body is naturally separated from the earth by a small capacitance Z_{bg}.

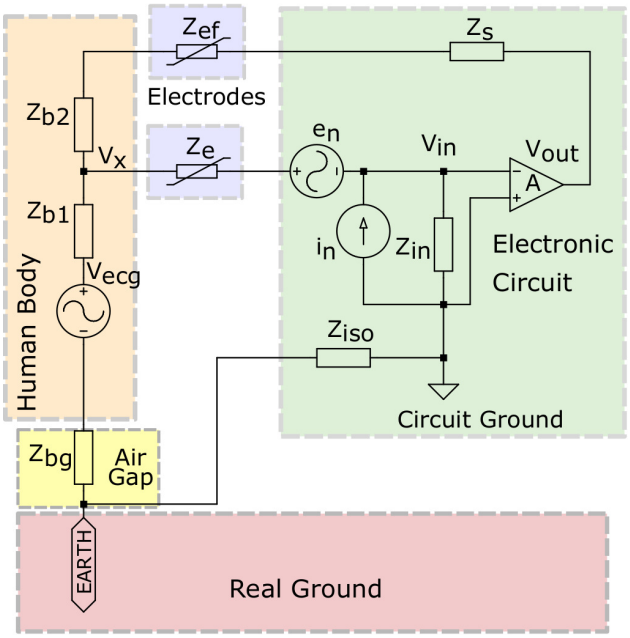

Figure 4.1: Electrical model of a cECG electrode connected to the human body and grounding

In order to simplify the system's transfer function, series elements were converted to single elements. Moreover, to obtain a transfer function that can be easily compared to simulation models, the 0V node was chosen to be the circuit ground. Therefore, Z_{iso}, Z_{bg} and Z_{b1} were condensed into the body to common impedance Z_{bc} ($Z_{bc} = Z_{iso} + Z_{bg} + Z_{b1}$) and, Z_s, Z_{ef} and Z_{b2} became the feedback impedance Z_f ($Z_f = Z_s + Z_{ef} + Z_{b2}$). The transfer function for cECGf is thus:

$$\frac{V_{out}}{V_{ecg}} = \frac{AZ_fZ_{in}}{[Z_f + (A+1)Z_{bc}]Z_{in} + (Z_e + Z_{bc})Z_f + Z_{bc}Z_e} \tag{4.1}$$

Figure 4.2 shows the proposed system converted to circuit elements, which can be estimated: $Z_{b1} \approx Z_{b2} = 100\ \Omega$ (Negligible), $1\,\text{pF} < C_e < 100\,\text{nF}$, $C_{ef} < 1\,\text{pF}$, $C_{bc} \approx 100\,\text{pF}$, $Z_{in} = 1\ \text{T}\Omega\ //\ 3\ \text{pF}$. Hence, $Z_f > Z_e \approx Z_{in} > Z_{bc}$. If $|A| >> Z_{in}Z_{bc}/Z_eZ_f$, equation (4.1) is

simplified to (4.2) and does not depend on Z_e.

$$\frac{V_{out}}{V_{ecg}} \approx \frac{Z_f}{Z_{bc}} \tag{4.2}$$

The reduced form relies on two impedances: Z_{bc} and Z_f, where Z_{bc} is highly dependent on Z_{iso}, which is almost independent of body movements. However, Z_f is given by $Z_{ef} + Z_s$, and Z_{ef} is a capacitive interface susceptible to body movements, hence, Z_s is chosen to be 10 times greater (0.1 pF) than the worst case scenario to attenuate impedance variations. Thus, if $Z_s = 0.1$ pF and $Z_{bc} = 100$ pF, the mid-band gain of cECGf is 1000.

Since ECG systems measure a small biological potential, they are susceptible to noise interference from the amplifier. The noise transfer function for e_n is the same as (4.1), however, V_{ecg} is around 1 mV while e_n is in the range of nV/$\sqrt{\text{Hz}}$. Considering the low bandwidth (<10 kHz) of the application and the large input impedance, the dominant noise source is thus the amplifier input current noise i_n. Its transfer function is:

$$\begin{aligned} \frac{V_{out}}{i_n} &= \frac{AZ_{in}[(Z_e + Z_{bc})Z_f + Z_{bc}Z_e]}{[Z_f + (A+1)Z_{bc}]Z_{in} + (Z_e + Z_{bc})Z_f + Z_{bc}Z_e} \\ \frac{V_{out}}{i_n} &= NTF_i \approx \frac{(Z_e + Z_{bc})Z_f}{Z_{bc}} = \frac{C_{bc} + C_e}{sC_eC_f} \end{aligned} \tag{4.3}$$

In the worst case scenario (i.e. when $Z_e >> Z_{bc}$) the output $V_{n,rms}$ is given by (4.4), where HF and LF being the high frequency and low frequency limits, and C_f is the series combination of C_{ef} and C_s.

$$\begin{aligned} V_{n,rms} &= \left(\int_{LF}^{HF} i_n^2 |NTF_i|^2 df \right)^{1/2} \\ V_{n,rms} &= i_n \frac{C_{bc}}{C_f C_e 2\pi} \left[\left(\frac{1}{LF} - \frac{1}{HF} \right) \right]^{1/2} \end{aligned} \tag{4.4}$$

4.1.2 Results and Discussions

To verify the theoretical analysis just presented, a cECG and the proposed cECGf systems were simulated in LTspice XVII. The circuits simulated are displayed in Fig. 4.2. The cECGf uses the feedback and the resistor values in red, while cECG does not have the feedback and the resistor values are in black. The resistors are different to match the same overall gain (V_{out}/V_{ecg}) of 1000 for both architectures. Some important characteristics of the buffer's

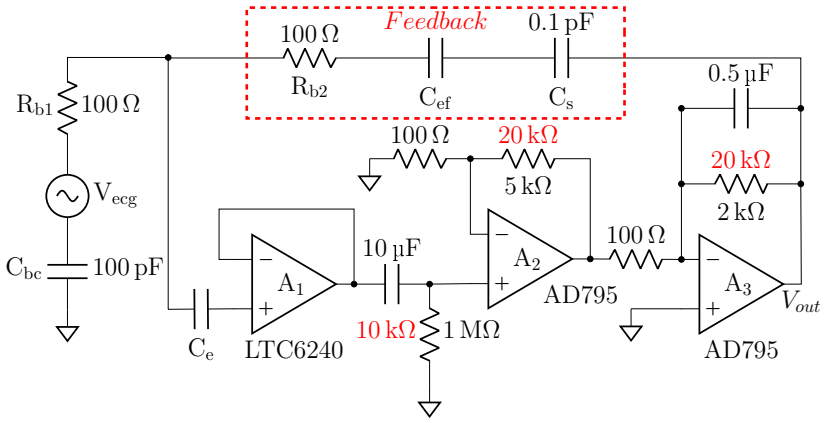

Figure 4.2: Simulated circuits, cECG does not have the feedback path and uses the resistor values in black, while cECGf requires the resistor values in red (when the resistor displays two values)

operational amplifier (LTC6240) are: input voltage noise between 0.1 and 10 Hz is 550 nV_{pp} and voltage noise density of 7 $nV/\sqrt{Hz}$ for higher frequencies, input current noise density equal to 560 $aA/\sqrt{Hz}$, R_{in} of 10^{12} Ω and C_{in} equal to 3.5 pF (differential) and 3 pF (common-mode).

4.1.2.1 AC response

Next, the AC response for both circuits is presented, within the ECG diagnoses frequency range (0.5 to 100 Hz). The coupling capacitances were varied from 100 nF to 1 pF. The curves were labelled F_x (the feedback system) and E_x (cECG without feedback). The numerical simulation of (4.1) labelled as TF_x is also shown.

Figure 4.3 (top) shows that for C_e=100 nF, the amplifier input impedance is high enough to maintain the gain and bandwidth in both systems. When the capacitance is reduced to 1 pF, the low cut-off frequency changes in both E_{1p} and F_{1p}, however, the mid-band gain of E_{1p} dropped by 13 dB while F_{1p} is practically unchanged. The transfer function simulation does not show any bandwidth change because A is constant, while in circuit simulation it is not. The transfer function simulation was also verified by replacing the opamps by an ideal controlled voltage source with constant gain A=10^5 and Z_{in} of 1 TΩ // 3 pF (these results are not shown).

The cECGf has the benefit of having increased bandwidth in comparison to cECG (property of the negative feedback), and the cut-off frequencies are controlled by filters and gain. Although we tried to make the bandwidth of both circuits as close as possible for fair comparison, the systems present different orders and they respond differently to the changes in C_e, leading to discrepancies in bandwidth.

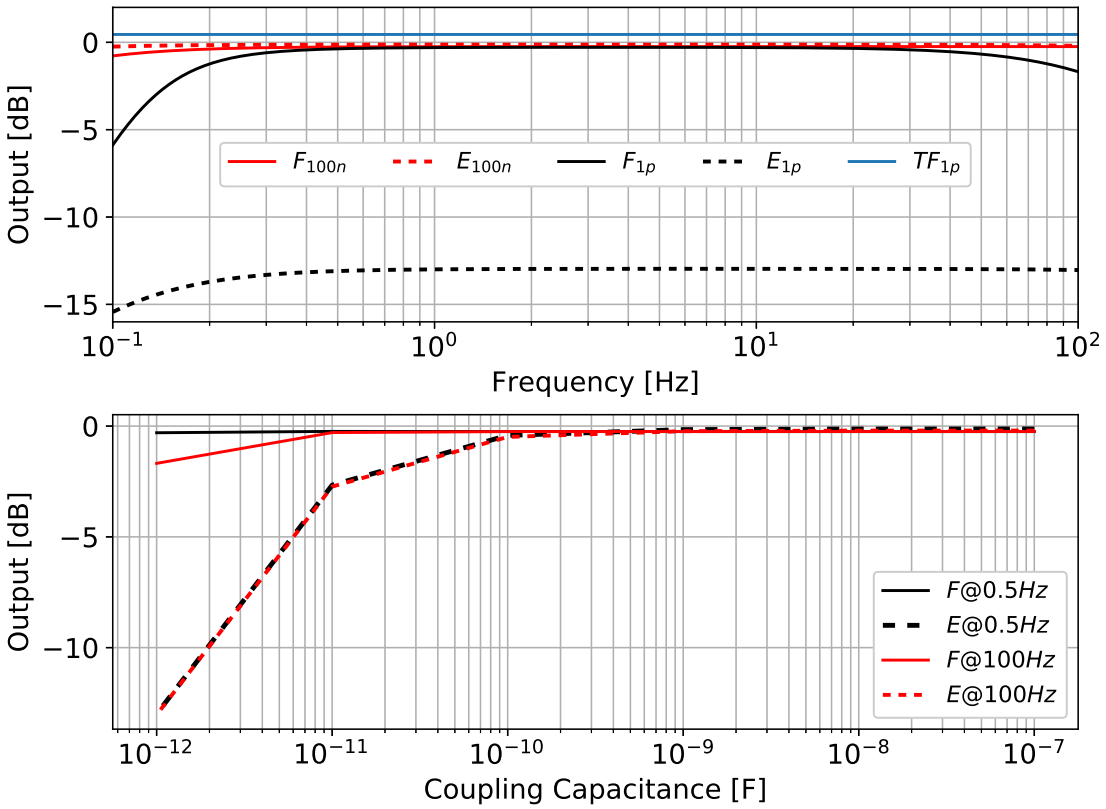

Figure 4.3: Top: E_x dotted traces represent the cECG output and F_x solid lines represent the cECGf output, x is the coupling capacitance. Bottom: Output at 0.5 and 100 Hz as function of $C_e = C_{ef}$.

Figure 4.3 (bottom) displays the output at two frequencies (0.5 Hz and 100 Hz) versus the coupling capacitance ($C_e = C_{ef}$). As the capacitance decreases below 1 nF, the cECG (E) output decreases exponentially for both frequencies, reaching -13 dB. On the other hand, the cECGf (F) gain remains constant for all values of coupling capacitances at 0.5 Hz. At 100 Hz, the gain decreases by 2 dB in the worst coupling case.

While it could be argued that the lowest simulated value of C_e is extreme, we also chose a very high input impedance. Systems that do not present such a high input impedance are more vulnerable to C_e variations and would benefit from the feedback even more.

4.1.2.2 Transient response

A time domain analysis was performed using an ECG waveform V_{ecg} with amplitude of 1 mV, while the coupling capacitance was varied dynamically. That means, three capacitors (1 pF, 10 pF and 100 pF) were placed in parallel and connected by switches. The coupling capacitor C_e can thus have values of 111 pF, 11 pF and 1 pF, while the feedback capacitor

C_{ef} is kept constant. Two simulations were performed, one for $C_{ef} = 100$ nF and one for $C_{ef} = 1$ pF.

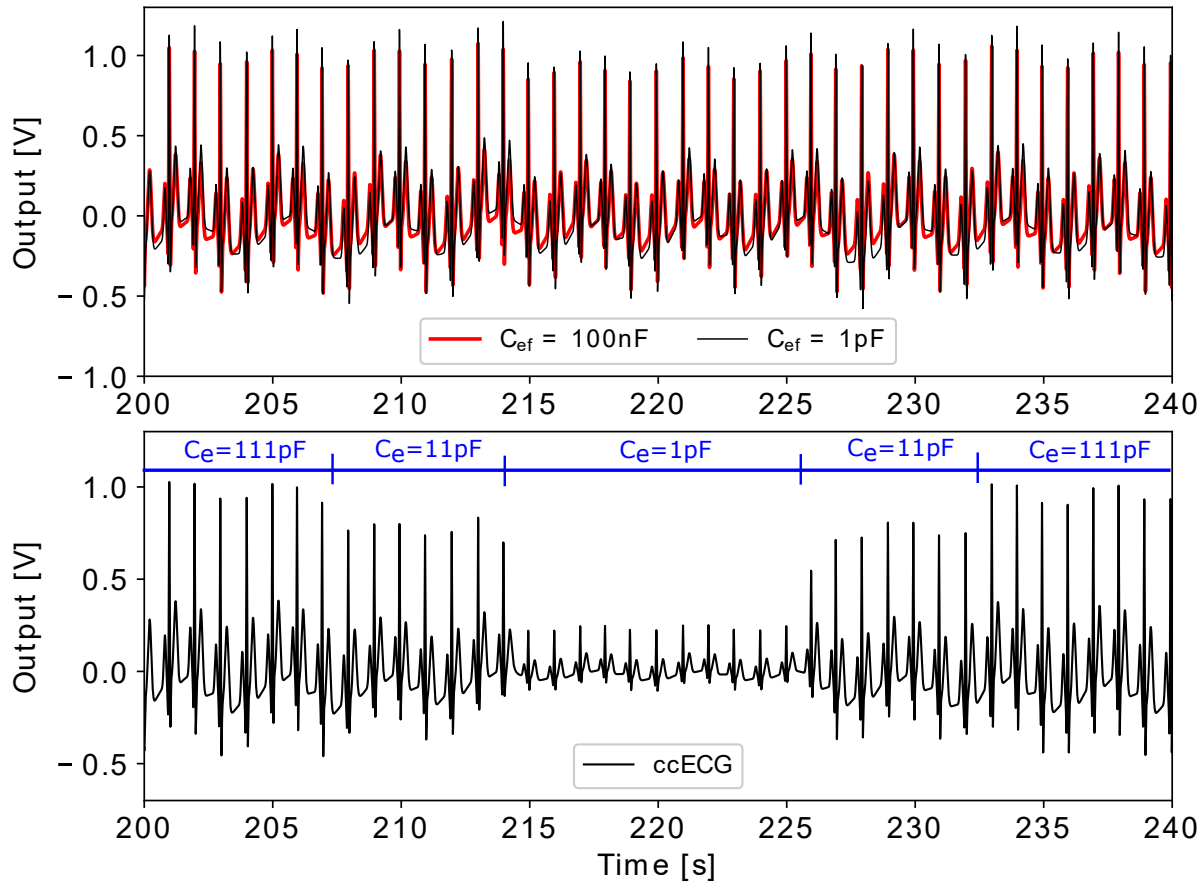

Figure 4.4: Time domain output. Top plot shows the cECGf with $C_{ef} = 100$ nF and $C_{ef} = 1$ pF while varying C_e, Bottom plot shows the output of the cECG with the same variations of C_e. The C_e values timeline is valid for both top and bottom plots

The bottom plot of Fig. 4.4 shows that when the coupling capacitance is 111 pF, the cECG peaks at around 1 V, decreasing to 0.7 V when $C_e = 11$ pF and falls to 0.2 V when the coupling capacitance is 1 pF. This means that without feedback, the output peak-to-peak value can vary from 1.2 V_{pp} to 0.2 V_{pp} when the coupling capacitance changes.

With the proposed feedback solution, cECGf, Fig. 4.4 (top plot) shows very small errors due to MA, for either C_e and C_{ef} variations. Comparing the output for different C_{ef} (red vs black in the top plot) one can see a difference of 10% in the peak value. Our hypothesis for this error is, when C_{ef} changes from 100 nF to 1 pF, $Z_s + Z_{ef}$ increases by 10% in (4.2). Yet, the artifact is almost null when only considering the variation of C_e.

Because the ECG measurement has to assess very low frequencies, the low cut-off frequency creates a long settling time. Moreover, this accommodation time must be fast enough

so as to minimize data losses while the system recovers from disturbances. To evaluate this time constant, a pulse response simulation was performed (Fig. 4.5), where the applied input pulse has an amplitude of 1 mV with duration of 50 seconds.

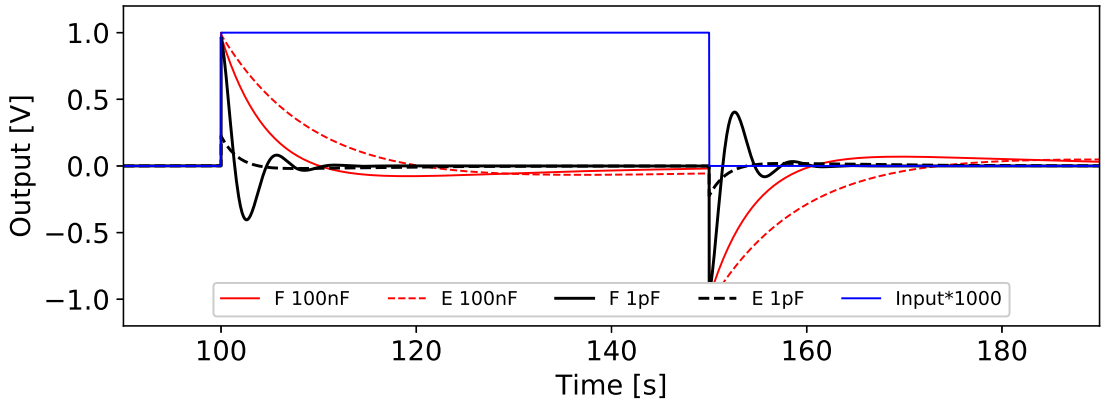

Figure 4.5: Pulse response simulation

The dashed curves represent the cECG (E) in two cases, C_e=100 nF and C_e=1 pF, where both traces present the same behavior. For the 100 nF coupling capacitance, when the pulse begins, the signal reaches 1 V and then it decays as time passes, yet, it does not reach zero within the pulse interval. For 1 pF, the cECG output does not reach the desired value (1 V), and by not reaching high values it is able to restore to zero during the pulse interval. These results are reasonable because the low cut-off frequency is determined by the high-pass 1^{st} order filter formed by C_e and the amplifier's input resistance, hence if C_e varies the settling time also varies ($\tau \approx R_{in}C_e$).

Regarding the cECGf (F, solid lines), for both capacitances the output reached 1 V. However, the behavior and settling time are different between these cases. Perhaps the easiest explanation is to assume the amplifying stage as a first order system, thus the feedback increases the overall system order. By changing the open-loop and feedback gains through C_e and C_{ef}, the damping factor of the transfer function is modified, which explains the presence or absence of ripples.

In addition to time-constants and settling time, the step response also shows that the system is stable for the range of electrode capacitances assessed. The plots for an electrode capacitance of 100 nF showed that both the standard capacitive ECG and the proposed system have an overdamped response. When an electrode capacitance of 1 pF is simulated, the standard method still presents overdamped behavior and the proposed systems has an initial overshoot and hence underdamped behavior. This is expected as the standard capacitive ECG is a first-order system and the proposed electrode is a second-order system. In all cases, the step response led to stable behavior.

4.1.2.3 Noise analysis

The output root mean squared voltage noise was simulated in Spice for cECG ($V_{ne,rms}$) and cECGf ($V_{nf,rms}$). The integration interval was from 0.5 Hz to 100 Hz and the noise voltage was computed for two values of coupling capacitances, 100 nF and 1 pF. The results show that $0.0033 < V_{nf,rms} < 0.33$ and $0.0033 < V_{ne,rms} < 0.075$ (all values in V_{rms}), where the highest noise occurs for the lowest capacitance and the lowest noise is related to the highest capacitance. However, the relation between signal amplitude and noise infers that both systems present a SNR of approximately 3 (1/0.33 and 0.22/0.075) for C_e=1 pF, while for C_e=100 nF, SNR $\approx$ 300. Hence, the proposed feedback technique does not degrade the noise performance. The large noise for C_e of 1 pF shows that to improve the quality of both cECG and cECGf, reducing noise is necessary.

4.2 Differential model

The single-channel cECGf showed that it can attenuate the effects of the coupling capacitance variations due to motion. However, it did not consider the common-mode voltages in the body (V_{cm_b} in Fig. 2.5). The 60 Hz interference can be much greater than the cardiac activity signal, thus using a very large A_s will likely saturate the amplifier.

Moreover, ECG and cECG are differential measurements, thus it is necessary to have at least a second electrode. One can take advantage of that by applying the large gain A_s to the differential signal and feeding it back through a pair of electrodes. The common-mode signal can be fed back by the standard DRL circuit.

4.2.1 Theoretical Development

4.2.1.1 Balanced Model

Figure 4.6 shows a simplified schematic for the differential feedback cECG (cECGfd). The subscripts "n" and "p" refer to the polarity of each channel (negative or positive), although the ECG signal is not fully differential. That means, the difference of voltage between V_p and V_n is the voltage drop through Z_b plus V_{ecg}, which does not imply that $V_n = -V_p$. Furthermore, to create negative feedback in each of the channels, the currents flowing through the measuring electrode and the feedback electrode must have the same polarity. Thus, for "p" the currents are going into Z_{in} and Z_{efp} while for "n" the currents are leaving Z_{in} and Z_{efn}.

The difference between V_{inp} and V_{inn} is performed by an instrumentation amplifier IA

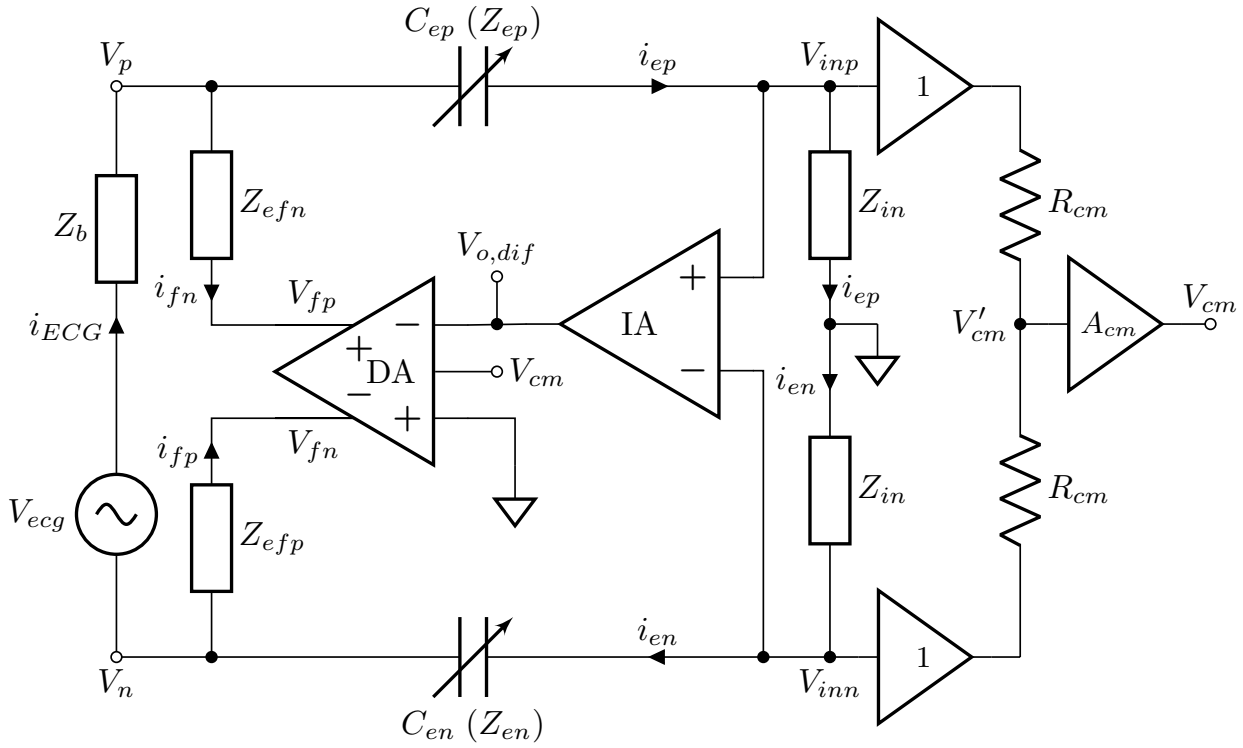

Figure 4.6: Simplified cECG system with differential through-body feedback

and the single-ended signal $V_{o,dif}$ is then applied to the inverting input of a fully differential amplifier (DA). The non-inverting input is tied to the ground, and V_{cm} provides a common-mode reference to V_{fp} and V_{fn}. If a common-mode level is not provided to these outputs, Spice simulations may lead to erratic behavior compared to the TF. For now, let $A_{cm} = 0$ thus $V_{cm} = 0$. Later, the common-mode feedback is also considered.

From Fig. 4.6, the nodal equations were obtained and applied to *wxmaxima* which retrieved the circuit's transfer function $\frac{V_{o,cECGfd}}{V_{ECG}}$. For a first assessment of the transfer function, the circuit is simplified by imposing $Z_{en} = Z_{ep} = Z_e$ and $Z_{efn} = Z_{efp} = Z_{ef}$, and is called "balanced circuit". The balanced circuit's transfer function (4.5) provides some understanding of the circuit dynamics.

The numerator of (4.5) relies only on two terms Z_{in} and Z_{ef}. The first is determined by the choice of amplifier, it is a combination of a resistor and a capacitor in parallel, thus being a constant value in time. The second, similar to the single-channel case, contains a time-varying impedance that must be kept constant.

$$\frac{V_{o,cECGfd}}{V_{ECG}} = \frac{2Z_{ef}Z_{in}}{[2Z_{ef} + (A+1)Z_b]Z_{in} + (2Z_e + Z_b)Z_{ef} + Z_bZ_e} \approx \frac{2Z_{ef}}{AZ_b} \tag{4.5}$$

On the denominator, the effects of the electrode's impedances Z_{ef} and Z_e must be removed or reduced. This is accomplished by setting the gain A (the gain provided by the DA, whereas the gain of the IA is 1) to a very high value. More accurately, the term AZ_bZ_{in} should dominate the denominator. Then, the gain seen by V_{ecg} to $V_{o,dif}$ is simplified to $2Z_{ef}/AZ_b$, while if we take the output at $V_{fp} - V_{fn}$, the gain is just $2Z_{ef}/Z_b$.

4.2.1.2 Unbalanced Model

To analyze the system's transfer function when there are channel mismatches, $Z_{efp} \neq Z_{efn}$ and $Z_{ep} \neq Z_{en}$, the electrode impedances in the positive channels are defined as being "k" times the one of the negative channels. In other words: $Z_{efn} = Z_{ef}$, $Z_{efp} = k_{ef}Z_{ef}$, $Z_{en} = Z_e$ and $Z_{ep} = k_eZ_e$.

From (4.5) it is known that a high gain ($A >> 1$) is necessary to compensate for the changes of Z_e, thus the unbalanced transfer function can be simplified by considering the terms that multiply A as the dominant ones. Further, assuming that a large motion happens and drastically increases the impedance of "p" electrodes, then $k_{ef} >> 1$ and $k_e >> 1$, resulting in the reduced transfer function with unbalanced electrodes (4.6).

$$\frac{V_{o,cECGf}}{V_{ECG}} = \frac{2Z_{ef}[Z_{in}k_{ef} + Z_e(k_e + k_{ef}) + 2k_{ef}Z_{ef}]}{A[Z_{ef}Z_ek_{ef}k_e + Z_b(2Z_{in} + Z_{ef}k_{ef} + Z_ek_e)]} \tag{4.6}$$

The key to achieving a constant gain in (4.6) is making Z_{ef} as low as possible. Hence in the denominator, the dominant term is $Z_b(2Z_{in} + Z_{ef}k_{ef} + Z_ek_e)$. The numerator comprises the expression $Z_{in}k_{ef} + Z_e(k_e + k_{ef}) + 2k_{ef}Z_{ef}$, hence if k_e is considerably larger than k_{ef}, the transfer function is reduced to $2Z_{ef}/AZ_b$. In other words, variations of Z_e are suppressed if Z_{ef} and k_{ef} are small enough for a given large A.

Of course, a practical issue arises with the demand for low Z_{ef} and k_{ef}. To keep a low and constant electrode impedance, the area of a capacitive electrode must be large and the contact (area and pressure) stable. Moreover, the gain is a function of Z_{ef}/Z_b, hence it is necessary to choose Z_{ef} to avoid saturation. Assuming that Z_b is 1 kΩ and the maximum Z_{ef} is 10 MΩ at 1 rad/s, the feedback non-contact electrodes must present capacitances greater than 0.1 µF. Albeit this might not be achievable in practice as it depends on the electrode's position and area, if these conditions are satisfied, it would enhance the accuracy for arrays of small capacitive electrodes (two large feedback electrodes and multiple small measuring electrodes).

The body impedance is unknown and must be found in practice. In case Z_b is too small and requires values of Z_{ef} that cannot be achieved with capacitive electrodes, the proposed

feedback can be used with the standard Ag/AgCl wet electrode. Although the wet electrodes do not present a large voltage division between Z_e and Z_{in}, the mismatch between channels is enough to significantly degrade the CMRR of the system. The wet electrodes impedances are considerably smaller than the one of the capacitive electrode, thus it is easier to secure small Z_{ef}, which can be stabilized by the insertion of a larger impedance in series ($Z_{ef} + Z_s \approx Z_s$).

4.2.1.3 Addition of the common-mode feedback

A common-mode feedback (CMF) can be included with the differential feedback in many ways. One of them is shown in Fig. 4.6, where the common-mode voltage between V_{inp} and V_{inn} is measured with resistors R_{cm}. Then, V'_{cm} is amplified with an inverting gain A_{cm} and fed back to the FDA's common-mode pin.

The resulting transfer function under balanced conditions is the same as in the case without CMF (4.5). This result is completely expected because under balanced conditions the common-mode is null, hence no actions from the CMF are supposed to happen.

For the case with unbalance electrodes, it is also set that A and A_{cm} are very large so they are the dominating terms in the denominator, and (4.7) is obtained. The conditions that $Z_{efn} = Z_{ef} = Z_{efp}/k_{ef}$, and $Z_{en} = Z_e = Z_{ep}/k_e$, are also kept. Consider that a MA largely reduced the capacitance of one measuring electrode ($k_e >> 1$), yet the feedback electrodes were kept equal ($k_{ef} = 1$). Further, if the feedback electrode impedances are larger than the body impedance ($Z_{ef} > Z_b$), the transfer function is reduced to (4.8). If the impedance of the electrode affected by MA is much larger than Z_{ef} and Z_{in}, then $Z_e k_e >> 2Z_{ef}$ and $Z_e k_e >> 2Z_{in}$, the transfer function is further simplified to (4.9).

$$\frac{V_{o,cECGfd}}{V_{ECG}} = \frac{2Z_{in}Z_{ef}[Z_{in}k_{ef} + Z_e(k_e + k_{ef}) + 2k_{ef}Z_{ef}])}{Z_{in}[A_{cm}(Z_{efp} + Z_{efn} + Z_b)(Z_{ep} - Z_{en}) + AZ_b(Z_{efp} + Z_{efn} + Z_{ep} + Z_{en} + 2Z_{in})]} \tag{4.7}$$

$$\frac{V_{o,cECGfd}}{V_{ECG}} \approx \frac{2Z_{in}Z_{ef}(Z_{in} + 2Z_{ef} + Z_e k_e)}{Z_{in}[2A_{cm}Z_{ef}k_e Z_e + AZ_b(2Z_{ef} + Z_e k_e + 2Z_{in})]} \tag{4.8}$$

$$\frac{V_{o,cECGfd}}{V_{ECG}} \approx \frac{2Z_{ef}}{2A_{cm}Z_{ef} + AZ_b} \tag{4.9}$$

Hence, if we consider that $AZ_b >> 2A_{cm}Z_{ef}$, the transfer function is again reduced to $2Z_{ef}/AZ_b$ as in the previous case. Then, why is it necessary to have the CMF? The CMF attenuates common-mode voltages, such as the 60 Hz interference and also reduces the effects of mismatches between Z_{efn} and Z_{efp}.

4.2.2 Circuit Design

Fig. 4.7 shows the proposed circuit (cECGfd). The measuring electrodes should be connected to the input terminals, while the feedback electrodes are placed in the output terminals. The input signals flow into the common-mode detection resistors, $R13$ and $R14$, and are inverted, amplified and filtered by the circuit comprising $U3$ and $U4$. The output of the common-mode circuit is V_{cm}. The differential circuit starts with an INA821 ($U8$) that subtracts the two input, while $U5$ and $U6$ provide a large gain and filtering. The fully differential operational amplifier $U7$ reconverts the signal into the differential mode, and send them to the feedback electrodes.

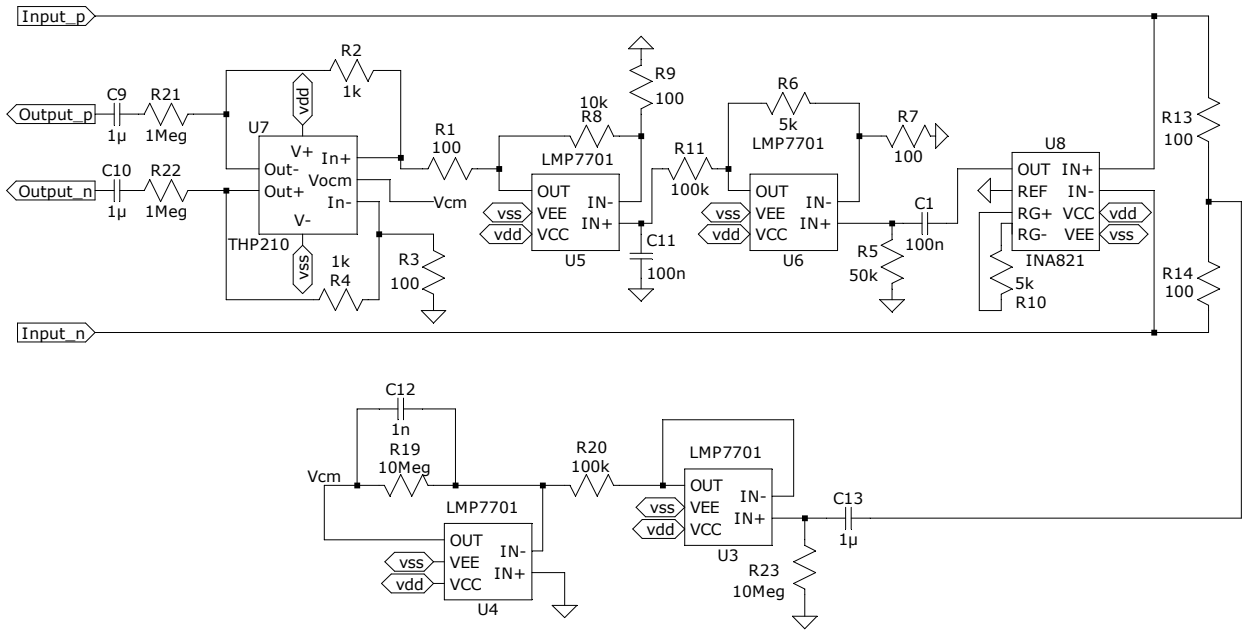

Figure 4.7: Circuit schematic of a cECG system with differential feedback

4.2.3 Results

An AC sweep was performed ranging from 1 mHz to 1 kHz, note that the desired ECG bandwidth lies between 500 mHz and 100 Hz. Two simulations were run, in the first one C_e=100 nF while in the second simulation C_e=1 pF. Fig. 4.8 shows the results, where the y-axis represents normalized gain in dB.

The results show that for the largest C_e, both topologies can reach the targeted mid-band gain. The low cut-off frequency of the cECG is much lower than the ideal value, while for the cECGfd the filters on the feedback path bring it closer to 50 mHz. When C_e is changed to 1 pF, cECGfd keeps the same mid-band gain while the low cut-off frequency moved up one

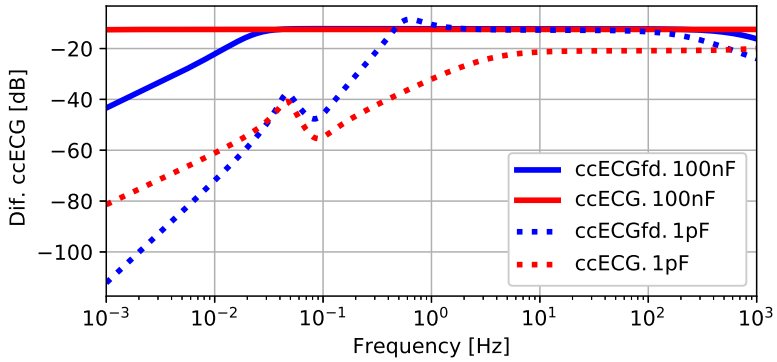

Figure 4.8: Output of the circuits with differential and common-mode feedback (blue) and only with common-mode

decade. For the cECG, voltage division appears and the cut-off frequency moves inversely to the decrease in C_e, now lying in the units of hertz. Both topologies presented a peak at 40 mHz, this is caused by the mismatch error signal in low frequencies not being fed back by the DRL circuit (filtered by $C11$ and $R20$).

The circuit shown in Fig. 4.7 was assembled in a custom PCB, while another board provided an ECG without the differential negative feedback. Figure 4.9 shows the ECG waveforms captured in two separate measurements, where the figures on the left side contain the traditional ECG and the figures on the right side depicts the ECG obtained with the proposed circuit.

The top figures show the ECG signal at the output of the instrumentation amplifier (INA821, U8 in Fig. 4.7). In the waveform presented in Fig. 4.9a (without the proposed feedback), the QRS-complex is very clear. However, the waveform obtained with the use of the proposed feedback (Fig. 4.9b) displays an ECG with negligible Q and S waves. In the case of the S-wave, the peak's amplitude is smaller, and its format is rounded. The hypothesis is that a low-pass filtering process took place.

The bottom figures show the measured ECG after the filtering and amplification stages (output of U5 in Fig. 4.7). These measurements were performed in a different day and with electrodes positioned in slightly different positions compared to the measurements presented in the top figures. Although the voltage scale is different in Figs. 4.9c and 4.9d, it is clear that in both cases the R-wave saturated the amplifier's output and the S-wave was much smaller in the proposed system. The 60 Hz noise is smaller in the proposed circuit because in addition to the common-mode feedback, the differential feedback also works on 60 Hz interference as it contains part of the signal not eliminated in the differentiation stage.

As shown in the theoretical modeling and simulations, the proposed system's transfer

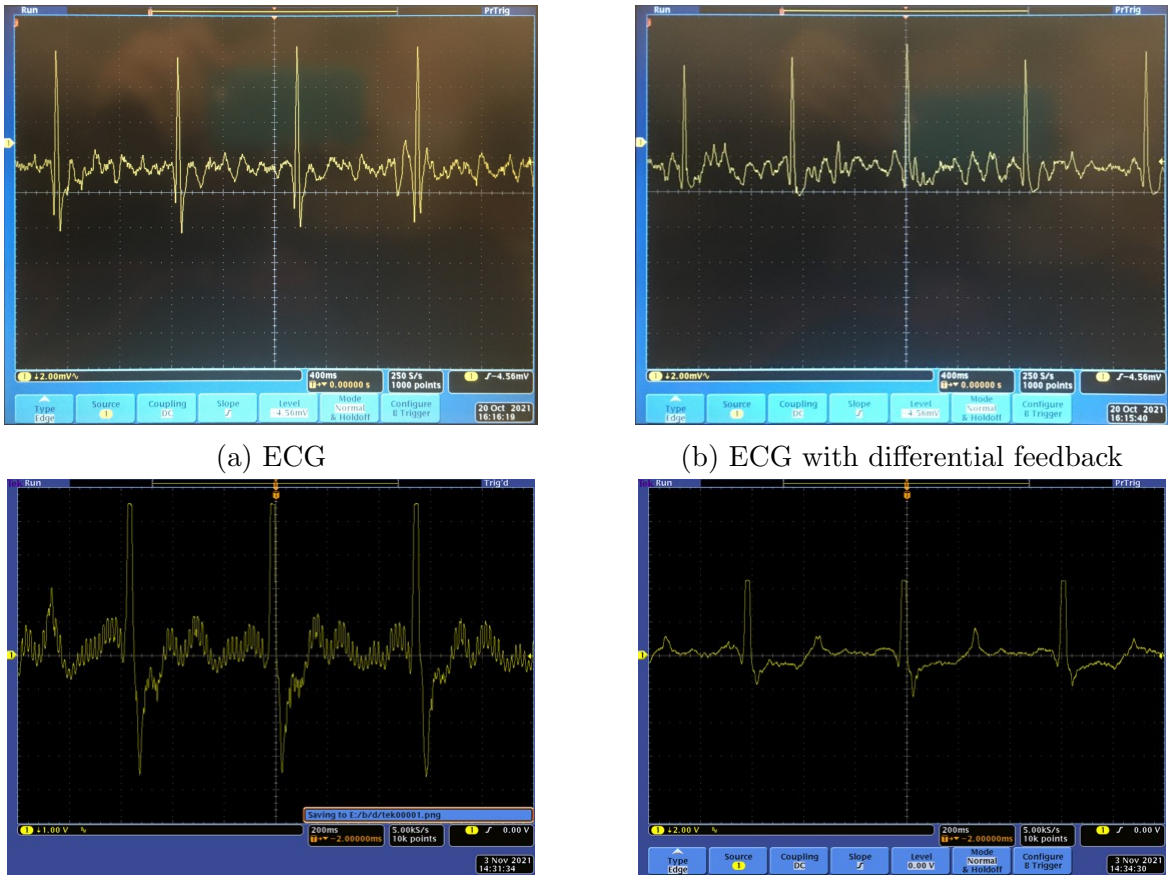

(a) ECG

(b) ECG with differential feedback

(c) ECG

(d) ECG with differential feedback

Figure 4.9: ECG measured with and without feedback. On the top, the signals measured at the instrumentation amplifier's output (low gain). On the bottom, the signals were measured after the gain and filtering stages

function showed a smaller dependency on the electrode coupling capacitance. On the contrary, it shows a strong dependency on the body (Z_b) and isolation (Z_{bc}) impedances. These components have been estimated and measured in the literature, however, the impedance between body and ground as well as the internal body impedances can change with time. In (4.9), the differential gain is inversely proportional to Z_b, therefore the measured signal is a mix between the ECG and the bioimpedance of the chest. This is supported by the distorted waveforms measured with the proposed system. This could be an interesting topic of research and possibly lead to a new evaluation tool of the heart's health. However, it falls too far from the scope of this work and we decided to interrupt the research on this topic.

Chapter 5

Conductance Neutralization

The simplest AFE (base circuit) that allows the measurement of biological signals from the human body through a capacitive interface is displayed in Fig. 5.1a [61]. It consists of an opamp in a buffer configuration and a bias resistor. Internally, each input of the opamp contains an input resistance ($R_{in,op}$) and an input capacitance ($C_{in,op}$), both are connected to ground and are omitted in Fig. 5.1a.

Further, the equivalent impedance formed between the sensing layer of a capacitive electrode and the surface of the human skin can be simplified to a pure capacitance C_e. The biological signals, picked by a single electrode in the human body, are represented by the signal source V_{bio}.

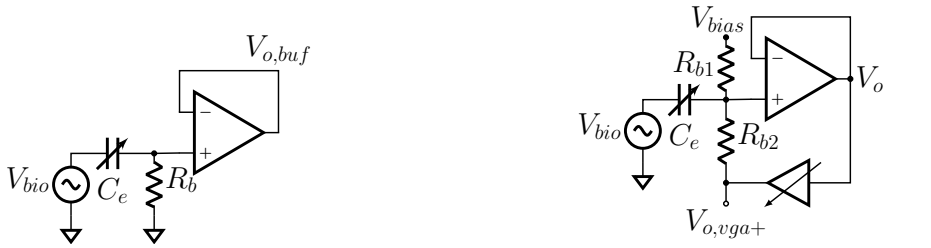

(a) Base circuit (b) Simplified proposed circuit

Figure 5.1: Simplified circuit schematics

The input of a commercial opamp requires a path that allows the flow of a bias current [13]. In an integrated CMOS amplifier, the input is commonly connected to the gate of a transistor because it presents very low leakage current, however, it requires a well-defined DC voltage to function. The resistance looking into this input gate terminal, has a similar role to $R_{in,op}$. Hence, a bias resistor (R_b) in parallel with $R_{in,op}$ is required to provide a path for the bias current or voltage. By assuming that the overall input resistance (R_{in}) is $R_{in,op}||R_b$, that the buffer has unity closed-loop gain, and that the total input capacitance is

C_{in}, the transfer function from V_{bio} to $V_{o,buf}$ is:

$$\frac{V_{o,buf}}{V_{bio}} = \frac{C_e}{C_e + C_{in}} \times \frac{s}{s + \frac{1}{R_{in}(C_{in} + C_e)}} \tag{5.1}$$

the mid-band gain is:

$$\left|\frac{V_{o,buf}}{V_{bio}}\right|_{\text{Mid}-\text{band}} = \frac{C_e}{C_e + C_{in}} \tag{5.2}$$

and the buffer's low cut-off frequency ($f_{c,buf}$) is:

$$f_{c,buf} = \frac{1}{2\pi R_{in}(C_{in} + C_e)} \tag{5.3}$$

The circuit presents a high-pass behavior. The cut-off frequency (5.3) depends on R_b, C_{in} and C_e while the mid-band gain (5.2) is a simple capacitive voltage divider between C_e and C_{in}. Voltage division should be avoided, and to fulfill this requirement, C_{in} must be much smaller than C_e. Moreover, if this condition is met, $f_{c,buf}$ can be approximated as $1/2\pi R_{in} C_e$.

5.1 Development

5.1.1 General Idea

A simplified schematic of the proposed circuit is shown in Fig. 5.1b. It comprises an operational amplifier in voltage follower configuration, two resistors at the non-inverting input (R_{b1} and R_{b2}), and a variable gain amplifier (VGA) with gain G.

The electrode capacitance forbids any flow of current from the amplifier to the body, hence, the resistor R_{b1} sets the input DC voltage to V_{bias}. The VGA creates positive feedback through R_{b2}. For simplicity, it is assumed that $R_{in,op}$ is very large, hence $R_{in,op}||R_{b1} \approx R_b$. Moreover, to simplify the equations, the particular case that $R_{b2} = R_b$ is considered. In a proper design, $C_{in} << C_e$ to avoid voltage division according to (5.2), thus C_{in} is neglected and the transfer function for the circuit in Fig. 5.1b is (5.4).

$$\left.\frac{V_o}{V_{bio}}\right|_{R_{b1},R_{b2}=R_b} = \frac{s}{s + \dfrac{2-G}{C_e R_b}} \tag{5.4}$$

By inspecting the pole of (5.4) and assuming a first order RC filter behavior, an expression for the overall input resistance is reached (5.5).

$$R_{in} = \frac{R_b}{2-G} \tag{5.5}$$

When the VGA's gain (G) is 0, R_{in} is $R_b/2$ (the parallel of R_{b1} and R_{b2}), however, as G increases closer to 2, the input resistance tends to infinity. Increasing the gain further than 2 may lead to oscillation due to excessive positive feedback, which moves the closed-loop pole to the right-half plane. It is also necessary to know the transfer function from the bias voltage to the output (5.6).

$$\left.\frac{V_o}{V_{bias}}\right|_{s=0} = \frac{1}{2-G} \tag{5.6}$$

In dual supply circuits V_{bias} can be set to 0 V, though modern applications are trending to low-voltage single-supply circuits which presents constraints regarding the bias voltage range. Equation (5.6) shows that the gain applied to V_{bias} is proportional to the boosting factor applied to R_{in}. Moreover, any noise coming from the bias voltage is amplified.

5.1.2 Transistor-Level Design

A block diagram of the proposed CMOS circuit is shown in Fig. 5.2. It consists of a low input capacitance buffer and a VGA with common-mode control and low-pass filter negative feedback. The transistor-level schematic of the buffer is shown in Fig. 5.3 and the VGA with its auxiliary circuits is depicted in Fig. 5.4

The buffer used here was the one proposed by [29] and shown in Fig. 5.3. This topology reduces the gate stray capacitances, which leads to negligible voltage division between the electrode capacitance and the input capacitance. It consists of a telescopic cascode opamp with unity gain feedback, wherein the output also drives the cascode devices ($M_{d,1c}$ and $M_{d,2c}$) and the bodies of all transistors in the differential pair are connected to the tail current source's output (drain of $M_{t,1c}$). Hence, the stray capacitance (C_{gd}, C_{gs} and C_{gb}) of

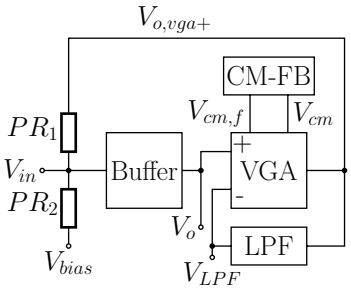

Figure 5.2: Block diagram of the proposed CMOS circuit

M_{d1} are bootstrapped. This circuit is also used in Chapter 6, where it is explained in more detail.

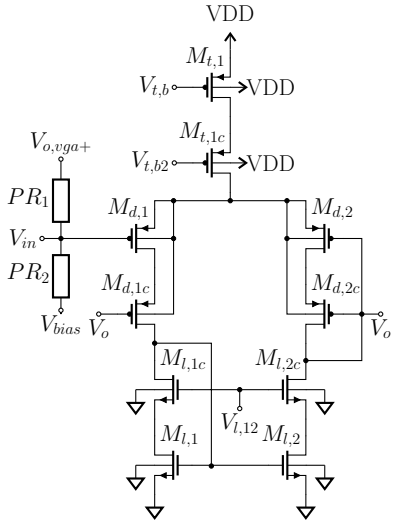

Figure 5.3: Bootstrapped buffer with pseudo-resistors

The bias resistors are implemented with pseudo-resistors such as the ones used in [86]. Pseudo-resistors attract the attention of the bio-amplifier community because they can be simply implemented with 1 or 2 transistors while providing very high resistance [87]. In recent years, the acceptance of pseudo-resistors has grown as researchers proposed improvements, such as enhancing their linearity and PVT sensitivity and making their resistance controllable [88].

The VGA's core is shown in Fig. 5.4a and consists of a PMOS differential pair, where the gain is controlled by the tail current. This control current is copied from an external current source by a current mirror, implemented with $M_{ctrl,p}$ and $M_{t,p}$. The differential pair's non-inverting input receives the input buffer's output (V_o). Two NMOS transistors, operating in the triode region, measure the common-mode signal (V_{cm}), which is amplified by a single-ended differential pair shown in Fig. 5.4b.

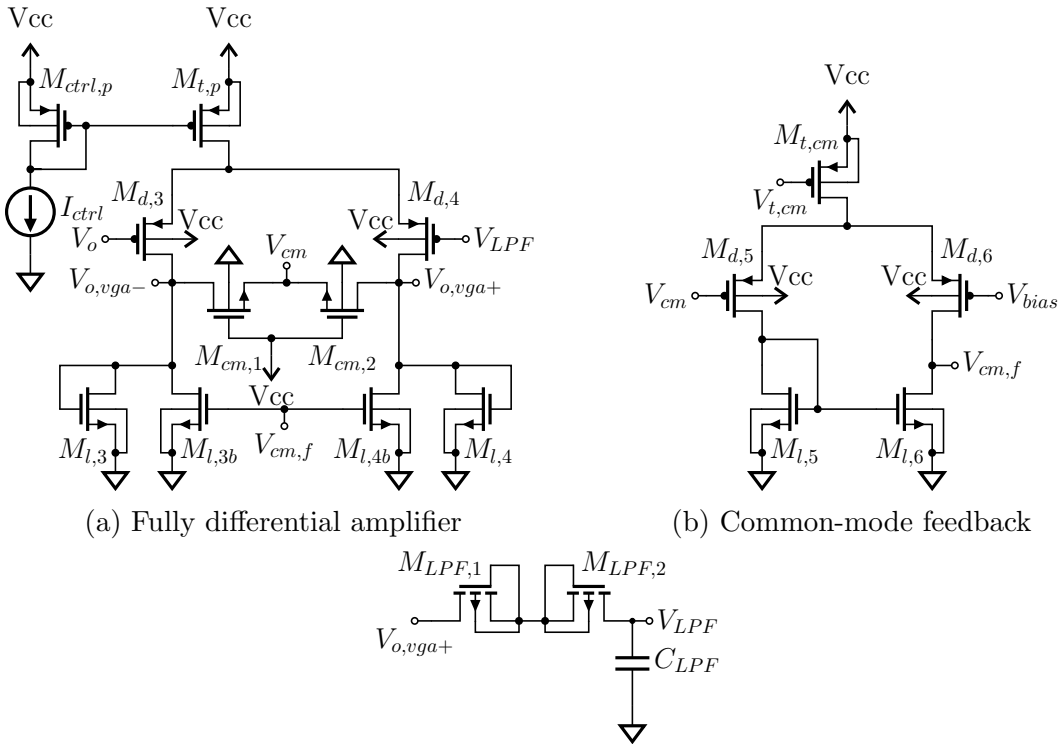

(a) Fully differential amplifier

(b) Common-mode feedback

(c) Feedback filter

Figure 5.4: Feedback network circuitry. The output of the buffer (V_o) is amplified by a fully differential amplifier. A feedback filter is used to control the differential amplifier frequency response and common-mode feedback controls the DC levels at the outputs

The load of the VGA comprises a diode-connected NMOS ($M_{l,3/4}$) in parallel with an active load that receives the common-mode feedback ($M_{l,3b/4b}$). Because the targeted gain is lower than 2, which is a relatively small gain, one can use diode-connected devices as the dominant load. That is, the diode-connected device presents an apparent resistance of $1/gm$, which is much smaller than the apparent resistance r_o of the current source loads.

The pseudo-resistors' (R_{b1} and R_{b2}) linear range is small ($\approx 50\,\text{mV}$), hence the DC component in the VGA's output ($V_{o,vga+}$) must be equal to V_{bias}. Common-mode feedback is essential to even out the voltage drop in both pseudo-resistors. The inverted and amplified common-mode signal ($V_{cm,f}$) controls the amount of current in the active loads ($M_{l,3b}$ and $M_{l,4b}$) and forces the current in the diode-connect loads ($M_{l,3}$ and $M_{l,4}$) to be constant. Moreover, if the amount of current in the dominating load is constant, so is the apparent resistance ($1/gm$). Consequently, changing the tail current modifies the differential pair's gm but not the load resistance.

Because the VGA's input is a sensed signal, it can be contaminated with large low-frequency artifacts. Thus, to avoid differential amplification of these signals and unmatched

DC bias, the low-pass filter network shown in Fig. 5.4c forms a negative feedback between $V_{o,vga+}$ and V_{LPF}. This filter defines the bandwidth of the VGA, and hence limits the bandwidth where R_{in} is boosted. The VGA's gain ($V_{o,vga+}/V_o$) without the feedback filter (open-loop) is named G'_{VGA}, while the gain with the feedback filter is G_{VGA}, and the equation that connects both is (5.7).

$$G_{VGA} = \frac{G'_{VGA}(1 + sC_{LPF}R_{LPF})}{G'_{VGA} + 1 + sC_{LPF}R_{LPF}} \tag{5.7}$$

Replacing G in (5.5) with (5.7), an equation for $R_{in}(s)$ with the frequency response is found:

$$R_{in}(s) = \frac{R_b}{2 - G'_{VGA}} \times \frac{s + (G'_{VGA} + 1)\omega_{LPF}}{s + \dfrac{(G'_{VGA} + 2)\omega_{LPF}}{2 - G'_{VGA}}} \tag{5.8}$$

G'_{VGA} is expected to be between 1 and 2, thus the pole in (5.8) is at a higher frequency than the zero. As G'_{VGA} gets closer to 2, the pole frequency increases with a factor $1/(2 - G'_{VGA})$. In low frequencies, R_{in} is approximately $R_b/2$ while in high frequencies it is $R_b/(2 - G'_{VGA})$. One should notice that opposing effects are taking place, as both the value of $R_{in}(s)$ in the pass-band and the pole frequency increase with $1/(2 - G'_{VGA})$. This means that the design of the feedback filter should consider the largest boost factor ($1/(2 - G'_{VGA})$), to ensure that the desired R_{in} is achieved before the electrode's cut-off frequency (given by $1/2\pi C_e R_{in}$). Replacing the input resistance with the frequency behavior (5.8) in (5.4), the transfer function V_o/V_{bio} is updated to (5.9):

$$\frac{V_o}{V_{bio}} = \frac{s[s + (G'_{VGA} + 1)\omega_{LPF}]}{s^2 + s\left[\dfrac{2 - G'_{VGA}}{C_e R_b} + (G'_{VGA} + 1)\omega_{LPF}\right] + \dfrac{(G'_{VGA} + 2)\omega_{LPF}}{R_b C_e}} \tag{5.9}$$

The zero at the origin, a real zero and two poles forces a high-pass filter behavior. However, as G'_{VGA} changes, the other zero and the two poles move. Thus, the frequency response can change from overdamped to maximally flat, underdamped, or oscillatory behavior. The values of the poles are obtained from the denominator of (5.9). A condition for stability is reached by simplifying the poles' expressions and conditioning them to be in the left-half plane:

$$(G'_{VGA}+1) > 2(G'_{VGA}-2)\omega_{in}/\omega_{LPF}. \tag{5.10}$$

The feedback pole (ω_{LPF}) should be at a lower frequency than the input pole ($\omega_{in} = 1/R_bC_e$). Hence, if $\omega_{in} >> \omega_{LPF}$, G'_{VGA} should be smaller than 2 for stable operation.

The output noise spectra of capacitive electrodes are known to be dominated mostly by input current noise [62]. It can be modeled by adding a noise current source (i_n) to the input node, and hence the transfer function V_o/i_n is the parallel of C_e, R_{in} and C_{in}. The variable i_n is a combination of current noise from the bias resistances and from the buffer's input. In capacitive electrodes, $C_{in} << C_e$ to avoid voltage division of V_{bio}, thus C_{in} is negligible. Hence, the noise transfer function is $R_{in}||1/sC_e$, which can be obtained by dividing (5.9) by $1/sC_e$ and is shown below.

$$\frac{V_o}{i_n} = \frac{\dfrac{s+(G'_{VGA}+1)\omega_{LPF}}{C_e}}{\left\{s^2 + s\left[\dfrac{2-G'_{VGA}}{C_eR_b} + (G'_{VGA}+1)\omega_{lpf}\right] + \dfrac{(G'_{VGA}+2)\omega_{LPF}}{C_eR_b}\right\}} \tag{5.11}$$

For very-low frequencies, (5.11) tends to $(G'_{VGA}+1)R_b/(G'_{VGA}+2)$, thus the smaller the R_b is, the smaller the low-frequency noise contribution. For high frequencies, the noise transfer function tends to $1/sC_e$, thus larger electrode capacitance leads to smaller noise. The transition between these two states shows a second-order low-pass behavior, and it depends on the values of G'_{VGA}, ω_{LPF}, and C_eR_b.

5.1.3 Board-Level Design

In addition to the CMOS circuit, we also propose a board-level design for the conductance neutralization. The proposed analog front-end of Fig. 5.5 (called here ConN) comprises a buffer, guarding circuit to bootstrap the PCB's parasitic impedances, capacitance neutralization to attenuate the input capacitance, series capacitance to reduce the effect of changes in C_e, and conductance neutralization. To control the amount of positive feedback in the neutralization circuits, R_1 and R_3 are potentiometers. Because a low-resistance path to ground is necessary for the DC bias current of U1, a high-pass filter formed by C_1 and R_5 was added (equivalent functionality to the feedback filter of Fig. 5.4c). In this manner, the input resistance is only boosted for frequencies higher than $1/(2\pi R_5C_1)$. An improved diode-based bootstrapped bias circuit replaces the bias resistor (R_b) and provides quick discharging in

the occurrence of large MAs.

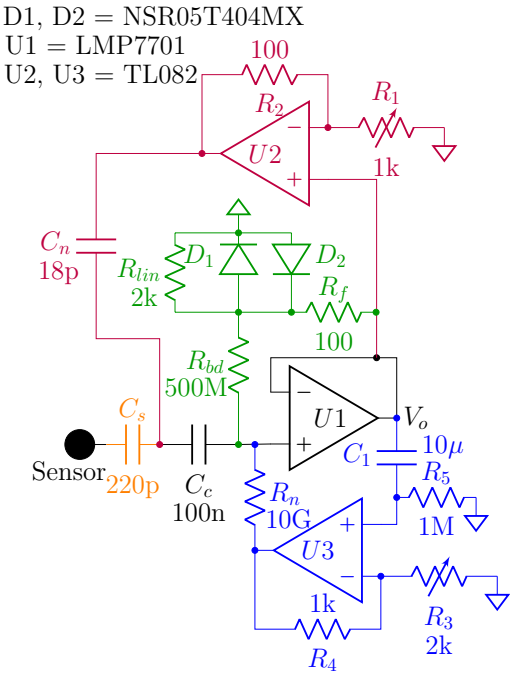

Figure 5.5: Proposed AFE (ConN). It comprises the base circuit (black), capacitance neutralization (purple), conductance neutralization (blue), series capacitor C_s (orange), and a biasing circuit with diodes "D" (green)

The use of a bias resistor R_b is a simple technique to provide the necessary bias current to the opamp's input. However, ultra-high resistors are inaccurate and require careful layout and mechanical assembly to avoid parallel leakage through the PCB's solder mask and any dust that can accumulate. To overcome these issues, bootstrapped bias circuits have been widely used [29], [39], [65], [67], [70], while the most recent developments use only resistors and varistors [69]. Here we introduce two modifications to this circuit as demonstrated in Fig. 5.5. First, the varistors are replaced by Schottky diodes. Then a resistor is placed in parallel with these antiparallel diodes. The equivalent input resistance is given by (5.12), where R_d is the parallel combination of the resistance of D_1 (R_{D1}), D_2 (R_{D2}) and R_{lin}.

$$R_{in,D} = \frac{R_d R_{bd}}{R_f} + R_d + R_{bd} \tag{5.12}$$

R_{bd} is the largest resistance, $R_{lin} > R_f$, and the on-resistance of the diodes ($R_{D1,2,on}$) is smaller than R_f. In normal operation, without voltage artifacts, the diodes are in an "off" state and present a very high resistance. Thus $R_d \approx R_{lin}$ and $R_{in,D}$ is R_{bd} boosted by a factor of R_{lin}/R_f. In the presence of a large voltage artifact, the diodes are "on" and R_d

becomes $R_{D1,on}$ or $R_{D2,on}$, which are very small. Then, $R_{in,D}$ is approximately R_{bd}, providing a low-resistance path for discharging the input node.

The operating dynamics of the circuit used here are the same as the original one in [69]. However, the Schottky diodes present smaller forward voltage than varistors, meaning that they help discharge the input node for lower artifacts. Moreover, if R_{lin} is not included, $R_{in,D}$ in normal operation is proportional to $R_{D1,2,off}$. These resistances change with small voltage artifacts, varying $R_{in,D}$. Hence, to force a constant $R_{in,D}$ when the diodes are "off", R_{lin} was included.

Note that both conductance neutralization and bootstrapped bias can boost the input resistance in discrete and integrated designs. However, the bootstrapped bias circuit cannot compensate for the discrete opamps input resistance or gate leakage in integrated circuits. Thus, the bootstrapped bias circuit is of best use as a replacement for R_b with a fast discharging feature.

Here we consider that C_e and V_{bio} are comprised within the "sensor" in Fig. 5.5 and that $C_{in} << C_e$ due to the capacitance neutralization. Then, conductance neutralization gain from V_o to the output of U3 is (5.13). Replacing this expression of G in (5.4) yields the transfer function for the complete circuit (5.14).

$$G = \left(1 + \frac{R_4}{R_3}\right) \frac{s}{s + \dfrac{1}{C_1 R_5}} \tag{5.13}$$

$$\frac{V_o}{V_{bio}} = \frac{s(s + \dfrac{1}{C_1 R_5})}{s^2 + s\dfrac{C_e R_b + (1 - R_4/R_3) C_1 R_5}{C_e R_b C_1 R_5} + \dfrac{2}{C_e R_b C_1 R_5}} \tag{5.14}$$

From (5.14) it is observed that similar to (5.9), there are two zeros and two poles. One zero is located at the origin while the other is defined by the high-pass $R_5 C_1$ filter within the conductance neutralization circuit. On the other hand, the poles rely on $C_e R_b$, $C_1 R_5$, and R_4/R_3, thus the poles are harder to predict as C_e is uncontrollable.

To comply with ambulatory ECG's bandwidth, f_c=0.5 Hz. For a range of C_e between 1 nF and 1 pF, the input resistance should range between 320 MΩ and 320 GΩ. Allowing up to 10% decrease in the mid-band gain due to voltage division between C_e and C_{in}, leads to the requirement of C_{in} <0.11 pF. This range of C_{in} is easily achievable with capacitance neutralization. The overall capacitance is the series combination of C_s and C_e, and hence C_s limits the maximum value. This aids in reducing the low cut-off frequency variations

with changes in C_e. If C_{in} is neutralized, C_s does not affect the mid-band gain, however, it increases the noise level as shown in (5.11).

In practice, we implemented many variations of the discrete-level proposed circuit, and the one shown in Fig. 5.5 was the preferred one. Removing $D1$ and $D2$ allows increasing the input resistance even further, though the discharge time of MAs becomes too long without the clipping mechanism. Removing C_1 and R_5 eliminates the low-frequency peaks, however, it introduces a DC voltage to the output, which affects the diode's working range. Another alternative is to lower the resistance of R_n to the same value as R_{bd}, facilitating component selection and reducing monetary cost. In that case, a simple adjustment of the VGA's gain leads to similar values of low cut-off frequency, however, the noise becomes larger. The chosen topology is supplied with $\pm 5\,\mathrm{V}$ to allow a larger output swing compared to the $2.5\,\mathrm{V}$ single-supply alternative circuit.

5.2 Results

5.2.1 CMOS Post-Layout Simulations

To explore gate leakage compensation, the low-voltage MOSFETs of the TSMC 65nm technology were chosen because they have gate leakage models. Thicker oxide devices are available in this technology and would provide better input resistance and noise levels, however, the gate leakage is not modeled. The circuit was simulated in Cadence Virtuoso with Spectre. These post-layout simulations comprised C+CC extracted models. A parametric simulation on I_{ctrl} (see Fig. 5.4a), swept the current from $1\,\mu\mathrm{A}$ to $10\,\mu\mathrm{A}$. AC frequency response, noise, and transient simulations were the analyses performed, and the results are shown in Fig. 5.6.

Fig. 5.6a displays the G_{VGA} variation as a function of the control current (I_{ctrl}). The gain was obtained by measuring the ratio of $V_{o,vga+}$ and V_o in an AC sweep. The range of gains desired is achieved for I_{ctrl} of $2\,\mu\mathrm{A}$ and $6\,\mu\mathrm{A}$, where G_{VGA} is 0.97 V/V and 2.04 V/V respectively. The VGA's gain increases due to the rise in $gm_{d3,4}$ ($\approx \sqrt{2I_{ctrl}\mu_p C_{ox} W/L}$), while the VGA's load impedance is kept fairly constant by the common-mode feedback loop.

The input impedance was analyzed with the ratio between the voltage and the current flowing into the circuit's input. Fig. 5.6b shows the input impedance in the pass-band. When G_{VGA} is 1.6 V/V, 1.9 V/V and 2 V/V the input impedance is respectively $27\,\mathrm{M\Omega}$, $83\,\mathrm{M\Omega}$ and $260\,\mathrm{M\Omega}$. The peak value of Z_{in} is $3\,\mathrm{G\Omega}$ for a gain of 2.04 V/V. Knowing that Z_{in} is in the pass-band, one can fit the data from Fig. 5.6b in (5.5). Thus, $R_b/2$ is estimated to be approximately $11.4\,\mathrm{M\Omega}$.

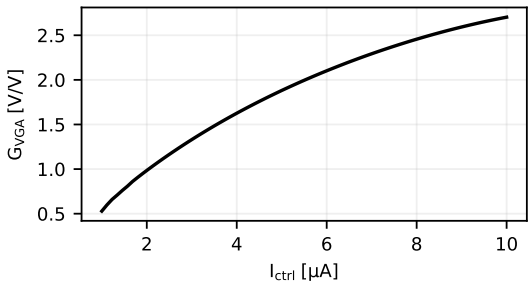

(a) G_{VGA} at 1 mHz as a function of I_{ctrl}

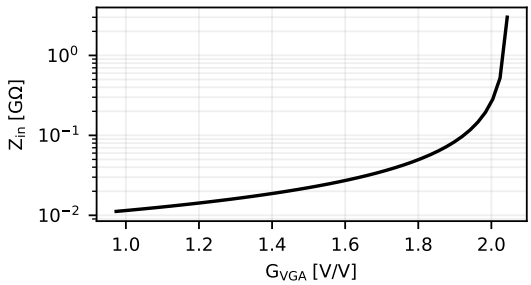

(b) Magnitude of Z_{in} as a function of G_{VGA} at 1 mHz

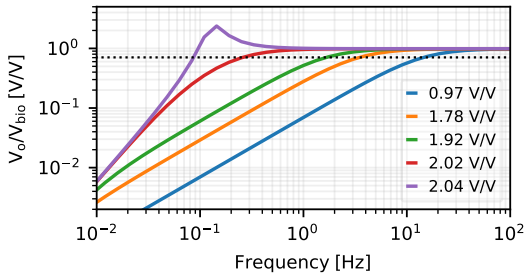

(c) Frequency response of V_o for different G_{VGA}, shown in the legend in V/V

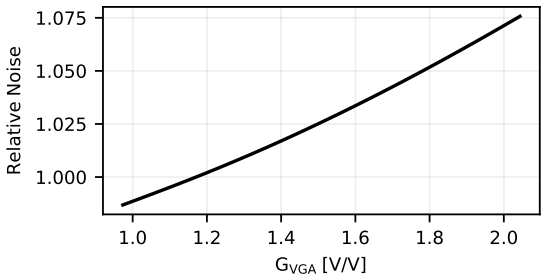

(d) Relative integrated noise as a function of G_{VGA}

Figure 5.6: Integrated CMOS design post-layout simulations

The slope of the curve in Fig. 5.6b provides the sensitivity of Z_{in} to changes in G_{VGA}. Note that to achieve impedance boosting over 100 times, G_{VGA} must be extremely accurate. Moreover, it cannot be vulnerable to noise or unwanted variations. However, for small impedance boosts, such as 10, the sensitivity of Z_{in} with G_{VGA} is much smaller and easier to achieve in practice.

The value of the capacitance between the body and the electrode (C_e) considered here ranges from 1 pF to 1 nF. The frequency response of V_o is shown in Fig. 5.6c, where C_e was 1 nF. The control current I_{ctrl} was swept as reported before, but only 5 curves are presented in Fig. 5.6c.

As expected from (5.9), the output demonstrates a high-pass filter behavior. The increase in I_{ctrl} (and G_{VGA}) decreases the cut-off frequency. Only the maximum simulated G_{VGA} led to a low-frequency peak (2.3 V/V). The cut-off frequencies for the displayed gains were 14.7 Hz, 3.5 Hz, 1.6 Hz, 0.25 Hz and 0.085 Hz. Taking as an example an electrocardiography, where the low cut-off frequency is 0.5 Hz, the proposed circuit is necessary to achieve the desired low cut-off frequency.

From the 40 steps in the parametric simulation, I_{ctrl} equal to 5.23 µA is the one that leads

to the largest bandwidth without peaking. As the current in the VGA increases beyond this I_{ctrl}, the transfer function behavior becomes underdamped. For 5.59 µA the cut-off was 75 mHz with a peak of 1.5 V/V at 0.33 Hz. For the case with the highest I_{ctrl}, a peak of 2.5 V/V occurred.

The relative noise, displayed in Fig. 5.6d as a function of G_{VGA}, is the proposed circuit's integrated input referred noise divided by the integrated input referred noise of the circuit without the input resistance boosting circuit. The integrated input referred noise was obtained from Spectre and the integration limits are 0.5 Hz and 100 Hz. For small G_{VGA}, the proposed circuit's R_{in} is smaller than R_b, tending to $R_b/2$ when G_{VGA} is zero. Thus the relative noise is smaller than 1. As G_{VGA} increases, the proposed circuit's input-referred noise rises and so does the relative noise. At the maximum R_{in} boosting, the noise is 7.5% higher compared to the circuit without boosting.

5.2.2 Board-Level Simulations and Measurements

The proposed AFE's transfer function (5.14) was numerically simulated to evaluate the frequency response and the results are depicted in Fig. 5.7. One of the zeros relies on C_1R_5 while the poles depend on both C_1R_5 and R_bC_e. Hence, variations in C_e change the damping factor ζ of the second order denominator, so C_1R_5 has to be designed to provide an acceptable output for a range of C_e values.

For this analysis, C_e was assumed to be 1 nF and 1 pF, R_b is 10 GΩ and $R4/R3$ is 0.969 to set the equivalent input resistance to 320 GΩ according to (5.5). C_1 was fixed at 10 µF while R_5 was 1 MΩ or 10 MΩ or 100 MΩ. Hence, the zero's frequency was 15.9 mHz, 1.59 mHz and 0.159 mHz respectively. C_s was not included in this simulation to allow an understanding of the frequency behavior with conductance neutralization for different electrode capacitances.

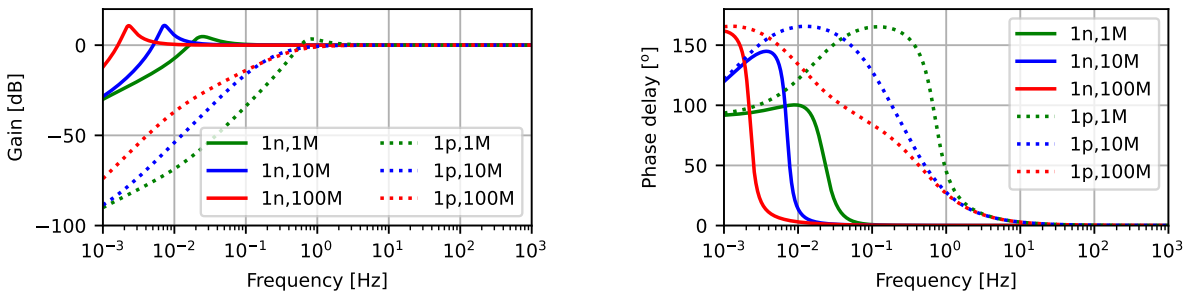

(a) Magnitude

(b) Phase delay

Figure 5.7: Numerical simulation of (5.14), where C_e and R_5 are varied. Legend is in the format "C_e [F], R_5 [Ω]". a) Magnitude of (5.14); b) Phase delay of (5.14)

The results in Fig. 5.7a shows that for C_e=1 nF, all curves have underdamped behavior with peaks of 10.8 dB at 2.3 mHz, 10.9 dB at 7.2 mHz and 4.8 dB at 24.8 mHz. On the other hand, when C_e=1 pF, the gain presents distinct behavior for each value of R_5. For 1 MΩ the curve displays lower damping, with the zero's effect being visible at 15.9 mHz and the complex-conjugate poles cause a peak of 3.5 dB at 0.82 Hz. Setting R_5 to 10 MΩ moves the zero to 1.59 mHz while bringing the poles closer to the real axis, which leads to a response closer to maximally flat. Last, R_5=100 MΩ reduces the zero's frequency to 0.159 mHz and separates the two poles, with their effects being visible around 10 mHz and 500 mHz. A root locus plot (not provided here) confirmed that when C_e is 1 pF, R_5 is 10 MΩ and 100 MΩ, the poles were real. In all other simulated cases, they were complex-conjugate pairs.

The effects described in the magnitude analysis are observed similarly in the phase delay analysis by inspection of Fig. 5.7b. Because of the zero at the origin in (5.14), the phase delay starts at 90°. By comparing the curves with the same color one can observe the effect of the other zero in the phase, which does not depend on C_e according to (5.14). Yet, the smaller damping factor of the complex poles when C_e is 1 nF compared to 1 pF is observed as a steep drop in phase. The aforementioned separation of poles is also visible in the phase plot. For example, the blue curve peak is much wider when C_e is 1 pF.

The high-pass filter (C_1 and R_5) was added to the conductance neutralization loop, so the overall input resistance is not boosted in very low frequencies and a path for the flow of the input bias current is provided. Hence, it creates an impedance that increases with frequency, behaving as an inductor. This apparent inductance interacts with C_e and may cause peaks in the frequency response and also oscillation. However, if well-designed, the filter increases the order of the electrode's high-pass characteristic. The chosen value of R_5 was 1 MΩ to provide similar peaking for low and high C_e with a steeper slope to enhance attenuation of lower frequencies and discharge faster.

Fig. 5.8 shows the measured frequency response of the proposed AFE for different coupling capacitances over a copper board. By replacing C_s (see Fig. 5.5) with a 0 Ω resistor, the condition with maximum coupling was assessed ($C_e \approx$1 nF). Then, a 1 pF capacitor was inserted into the place of C_s, simulating the worst-case scenario. The results shown in Fig. 5.8 are for a maximally boosted input resistance. That is, the calibration took place with a C_s of 1 pF, and the potentiometer was adjusted until the edge of oscillation.

In Fig. 5.8a, the reference AFE displayed an f_c value of 71 mHz for full capacitance (Ref). When C_s was 1 pF, f_c was 72 Hz (Ref 1p), which is too high for ECG measurement. For full C_e, the proposed AFE showed approximately 8 dB (ConN) of peaking, and its f_c was 33 mHz (ConN). When C_s was 1 pF, the peak was negligible and the cut-off frequency was 1.5 Hz (ConN 1p).

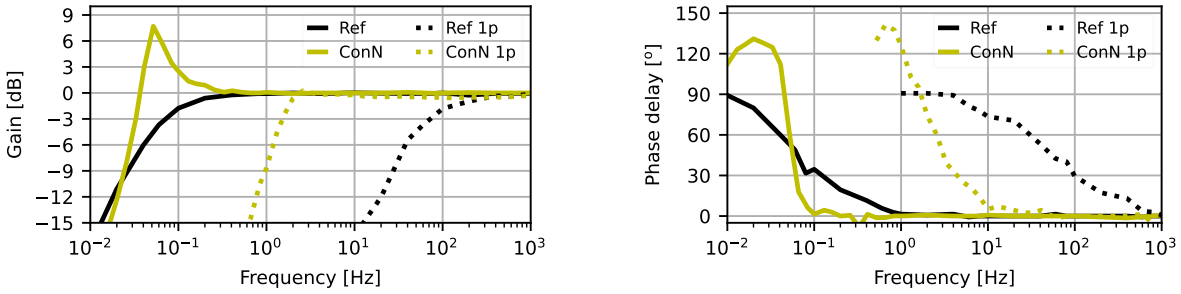

(a) Magnitude

(b) Phase delay

Figure 5.8: Measured bode plot comparing the proposed AFE with the reference AFE. Labels with "1p" stand for circuits where the coupling capacitance was limited by using C_s of 1 pF, while the absence of 1p means that the electrode had maximum electrode capacitance (≈1 nF)

The measured phase delays in Fig. 5.8b are in agreement with the numerical simulations shown in Fig. 5.7b. The phase for the reference AFE starts at 90°, falling to 45° at the cut-off frequency and then reaching zero. The ConN peaks were of 130° at 30 mHz and of 141° at 0.66 Hz. Some traces in Fig. 5.8b are not plotted in the whole frequency range because of the minimum scale of the measuring device. The injected signal's peak-to-peak amplitude was 40 mV, while the minimum resolution of the oscilloscope is 1 mV per division. Hence the output of the reference AFE for C_e equal to 1 pF was too small for frequencies below 1 Hz. Furthermore, the oscilloscope's noise floor was also in the amplitude of the minimum resolution, making measurements in this range of voltages impossible.

For the full C_e, the peak in the gain magnitude was high, and the increase in bandwidth compared to the reference AFE is small. This happens because the R_5C_1 limits the range of frequency where the input resistance is boosted. However, in this measurement, the conductance neutralization gain was maximized to lead to the lowest f_c when C_s =1 pF and was not optimized for high C_e operation. Hence, when C_s is forced to be 1 pF, one can clearly see the input resistance boost at work. Even though the ConND had an f_c 3 times larger than 0.5 Hz for the minimum capacitance, it performed much better than the reference AFE, which had f_c 144 times greater than the desired value. This scaling in cut-off frequency is proportional to the increase of R_{in}.

With the measured low cut-off frequency and the electrode capacitance value, one can estimate the input resistance ($f_c = 1/2\pi R_{in}C_e$). By inspecting the curve from the reference AFE (Ref 1p) in Fig. 5.8 and knowing that C_e was 1 pF, the overall R_{in} is estimated to be 2.2 GΩ. The value of R_b is set to 10 GΩ, and the datasheet of LMP7701 does not provide a value for $R_{in,op}$. Thus we can calculate the value of $(R_{leak}||R_{in,op})$ as 2.82 GΩ. The proposed

circuit with 1 pF capacitance had a cut-off frequency of 1.5 Hz, thus the apparent input resistance is 106 GΩ. This represents a boost of 48 times compared to the reference circuit's input resistance.

To display the clipping mechanism of the bootstrapped circuit with diodes, a triangular waveform was injected into the copper board that was underneath ConN and Ref electrodes. This input signal had a peak-to-peak amplitude of 1 V at a frequency of 0.5 Hz.

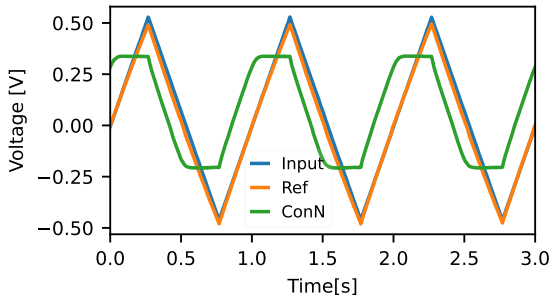

Figure 5.9: Proposed AFE's response to a triangular input

The data from Fig. 5.9 shows that the clipping region was as expected, and signal amplitudes above the Schottky diode forward voltage are blocked. The clipping values were −0.28 V and 0.3 V. During the discharge period (one of the diodes conducting), the resistance seen from the input node is 500 MΩ. The proposed circuit presented a slight phase shift compared to the input and the reference circuit. One can also see distortion on the reference circuit curve, which is caused by the high-pass characteristic.

To demonstrate the performance of the proposed electrodes under different coupling conditions, the common-mode rejection ratio (CMRR) of an unbalanced pair of electrodes was measured. That is, a pair of identical capacitive electrodes were attached to the subject's lower back. One of the electrodes had direct contact with the skin and the other was connected through a cotton t-shirt. A reference signal from the signal generator was injected into the human body through a wet Ag/AgCl electrode connected to the right ankle, enabling the frequency response in realistic conditions to be obtained. An elastic band around the subject's waist held the electrodes in place. The three tested topologies were: the reference circuit, the proposed circuit with C_s (220 pF), and the proposed circuit without C_s (C_s shorted). The bode plot is displayed in Fig. 5.10. The objective is to assess the improvement in the CMRR provided by C_s, which happens mainly around the low cut-off frequency. Thus, only the lower frequencies are displayed.

Fig. 5.10 shows that for frequencies higher than the ambulatory ECG's low cut-off frequency (0.5 Hz), the proposed circuit presented higher CMRR than the reference electrode.

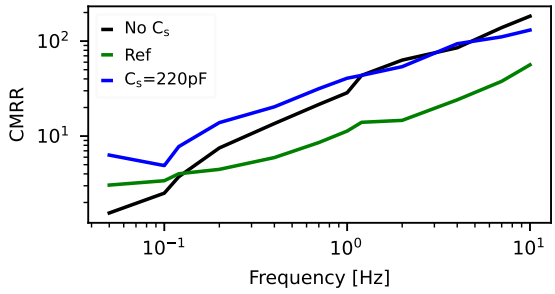

Figure 5.10: CMRR of unbalanced electrodes. The reference circuit and proposed circuit with and without C_s are evaluated

In very low frequencies, the proposed circuit with C_s had the highest CMRR, while the proposed circuit without C_s had the worst CMRR. The explanation is the low-frequency peak created by the conductance neutralization when C_e is high. Because in this test one electrode has direct contact with the skin (high C_e) and the other has a smaller C_e, the peaks' amplitudes differ and create a CMRR issue. The proposed circuit with C_s has a smaller low-frequency peak, and the cut-off becomes less dependent on C_e. The reference circuit does not present low-frequency peaks but the cut-off frequency is inversely proportional to C_e. Thus, the added layer of clothing directly modifies the low-frequency response creating a mismatch and reducing the CMRR.

An ECG acquisition is demonstrated in Fig. 5.11. The waveforms displayed were obtained by using a pair of balanced similar electrodes. The reference circuit and the proposed circuit with and without a C_s of 220 pF were tested. The left column of Fig. 5.11 shows the ECG measured in direct contact with the skin and the right column shows the acquired signals measured through a T-shirt. The acquisition board possessed a band-pass filter with bandwidth between 50 mHz and 300 Hz, then a 2^{nd}-order digital band-pass with cut-off frequencies between 0.5 Hz and 100 Hz was applied in addition to a digital 4^{th}-order notch filter at 60 Hz. The subject was grounded with a wet Ag/AgCl electrode and the driven right leg circuit was not used.

The measurements of ECG in direct contact with the skin (left column of Fig. 5.11) led to clean ECG waveforms for all three electrode topologies. The proposed circuit without C_s was the one with less 60 Hz interference, followed by the one with C_s. This was expected from Fig. 5.10 even though the CMRR at 60 Hz was not measured due to the mixing of noise and reference signal. Most of the breathing/motion artifact was removed by the digital band-pass filter in all cases. In the through-clothing acquisition, in both proposed circuits the QRS wave is still identifiable. However, the breathing artifact is significant, especially in the case without C_s where low-frequency CMRR is worse. Due to the smaller capacitance

generated by C_s, noise is also visible in Fig. 5.11f. The reference circuit was not capable of proving a readable ECG through clothing. The proposed circuit's simulated RMS output noise, considering an electrode capacitance of 220 pF and integration limits of 0.5 Hz and 100 Hz, is 6.12 µV.

5.3 Conclusion

In this chapter, we proposed a capacitive electrode topology based on a NIC circuit that boosts the input resistance and is not sensitive to gate leakage and the opamp's input resistance. An integrated CMOS design was developed and simulated (post-layout). The results showed that with 40 steps of I_{ctrl}, the input resistance can be boosted by a factor of 100. Besides the power and area increase, the performance cost is a 7.5% increase in noise. These results were supported by measurements on a discrete design, where the input resistance increased by 48 times.

The boosted input resistance allowed the insertion of the small C_s in series with the electrode capacitance, reducing the variations of the f_c caused by the changes in the electrode capacitance and consequently improving the CMRR. Compared to the reference electrode, the proposed circuit was able to measure an ECG in direct contact with the skin and through clothing. The addition of C_s increases the amplifier's noise, however, it reduces the breathing artifact.

The results provided in this chapter showed improvements in the overall performance of the AFE of a capacitive electrode for biomedical applications. Yet, some challenges must be addressed to achieve large-scale production. Here, both neutralization loops were tuned with a potentiometer, which requires manual trimming and are expensive. Fixed value resistors present inaccuracy that could lead to mismatched electrodes, and in the worst-case scenario, oscillation of the positive feedback.

The capacitance neutralization usually does not require very fine tuning as commercial opamp's are already in the range of a few pF. Moreover, alternatives to the capacitance neutralization exist [29], [89] and it can also be automatically tuned [90]. Large input capacitances lead to voltage division and subsequent degradation of the mid-band CMRR.

The inaccuracy in the conductance neutralization loops affects R_{in}, and hence creates mismatches in the low cut-off frequencies. This is a critical issue if large input resistance boosting is targeted because accurate positive feedback gain is necessary. However, one should mind that even if C_s is used, significant mismatch in the low cut-off frequency is expected due to mismatched C_e.

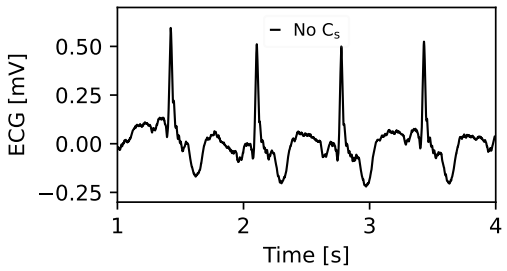

(a) ECG from proposed electrode without C_s in direct contact with the skin

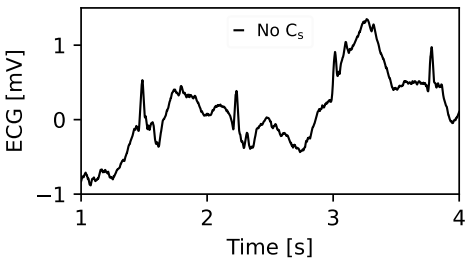

(b) ECG from proposed electrode without C_s through T-shirt

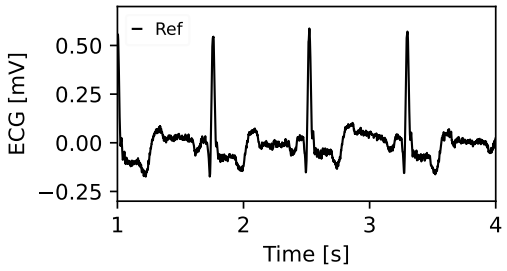

(c) ECG from reference circuit in direct contact with the skin

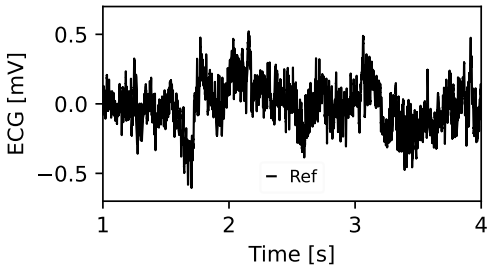

(d) ECG from reference electrode through T-shirt

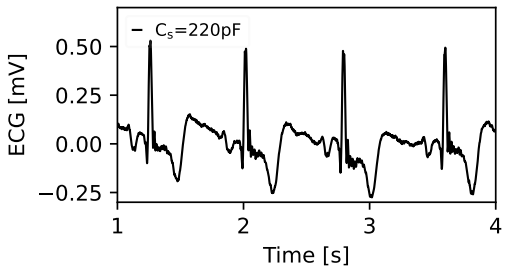

(e) ECG from proposed electrode with C_s=220 pF in direct contact with the skin

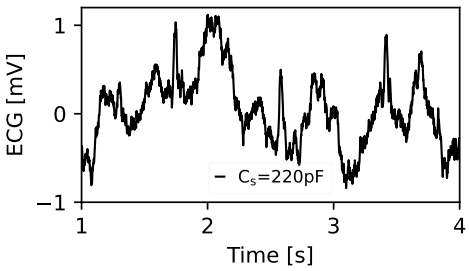

(f) ECG from proposed electrode with C_s=220 pF through T-shirt

Figure 5.11: Measured ECG with proposed and reference circuits in direct contact with the skin and through clothing. The proposed circuit was tested with and without C_s

Chapter 6

Cut-off frequency control

The simplest model for a capacitive active electrode is the one shown in Fig. 6.1a. The interface between the human body and the analog front end is a variable capacitor C_e, and the fixed resistor $R_{b,f}$ provides a DC voltage to bias the input of the opamp, which is connected in a buffer configuration. Using C_e simplifies the contact impedance to a single component, whereas for more accurate modeling each layer (PCB's solder mask, clothing, air, stratum corneum) is described as a capacitor in parallel with a resistor [13], [20], [61].

With motion, the pressure applied onto the electrode towards the body varies, and an air gap appears if the contact ceases. Therefore, C_e changes with motion and so does the buffer's low cut-off frequency $f_{l,b}$, computed as:

$$f_{l,b} = \frac{1}{2\pi R_{b,f} C_e} = \frac{1}{2\pi \tau_{l,b}} \tag{6.1}$$

The changes in C_e also disturb the charge distribution in the input node, which merged with triboelectric voltages and slow common-mode signals, generates large artifacts [12], [25], [76]. The time required to discharge an RC circuit is proportional to the time constant $\tau_{l,b} = R_{b,f} C_e$. Thus, one can estimate the interval of time needed for the signal's baseline to return to its origin after a MA event in a capacitive electrode.

Biopotential acquisition systems have different cut-off frequency demands, and this chapter targets an ECG system with a low cut-off frequency of 0.5 Hz and C_e between 1 pF and 100 pF [34], [36]. Let the best case scenario be when there is strong contact and C_e is 100 pF, while the worst case scenario happens due to a motion that creates an air gap and reduces C_e to 1 pF.

Consequently, the design of $R_{b,f}$ faces a trade-off between bandwidth and settling time [62]. If one chooses an $R_{b,f}$=318 GΩ to provide $f_{l,b}$=0.5 Hz during the worst case scenario,

$\tau_{l,b}$ during good contact is 31.8 s. If a motion restores good contact, the ECG will be off from its baseline for more than 2 minutes (assuming $5\tau_{l,b}$). On the other hand, if $R_{b,f}$ is set to 3.18 GΩ, the circuit will discharge quickly, but it only has enough bandwidth during good contact and attenuates the signal when C_e decreases.

6.1 Proposed System

The issue of the low cut-off frequency changing with C_e can be solved if the bias resistance follows the motion and adjusts inversely proportional to C_e. In this manner, the low cut-off frequency would always be 0.5 Hz and the time-constant is maintained close to 0.318 s. To track C_e without adding a sensor for motion [35], the circuit of Fig. 6.1b is proposed, where R_b is a controllable resistor and C_{test} is a capacitor added to inject a test signal V_{test} into the input node.

Assuming the opamp is ideal (input impedance is extremely high), the output (V_o) of Fig. 6.1b is described by the superposition of V_1 (6.2) and V_2 (6.3), where V_1 is the output generated by V_{ecg} and V_2 is the output from the V_{test} input. Moreover, C_e is defined as a function of motion m while R_b is a function of a control signal x. Thus, they are expressed as $C_e(m)$ and $R_b(x)$.

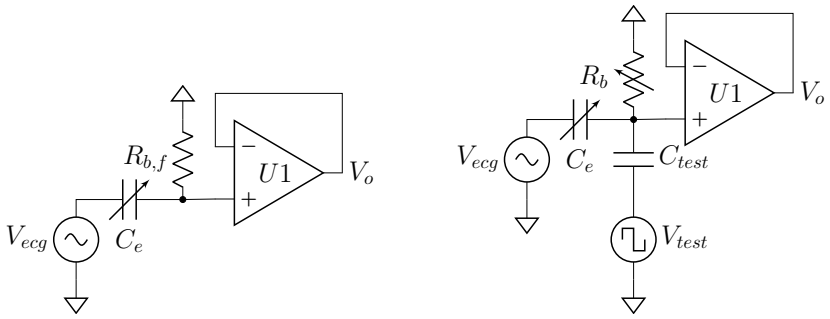

(a) Simplest electrode (b) Proposed electrode

Figure 6.1: Input node model of a capacitive electrode

$$V_1 = V_{ecg}\frac{C_e(m)}{C_{test}+C_e(m)}\frac{s}{s+\dfrac{1}{R_b(x)[C_{test}+C_e(m)]}} \tag{6.2}$$

$$V_2 = V_{test}\frac{C_{test}}{C_{test}+C_e(m)}\frac{s}{s+\dfrac{1}{R_b(x)[C_{test}+C_e(m)]}} \tag{6.3}$$

Both equations show a high-pass filter behavior and the low cut-off frequency (f_l) is computed with (6.4). In the passing band, the two equations comprise a capacitive voltage divider. From (6.2), C_e should be much greater than C_{test} to avoid attenuation of V_{ecg}. If this condition is met and the frequency of V_{test} is greater than f_l, then the pass-band gain of (6.3) can be approximated to $C_{test}/C_e(m)$. Hence, the output of the proposed analog front-end is given by (6.5).

$$f_l = \frac{1}{2\pi R_b(x)[C_{test} + C_e(m)]} \approx \frac{1}{2\pi R_b(x) C_e(m)} \tag{6.4}$$

$$V_o = V_1 + V_2 \approx V_{ecg} \frac{s}{s + \dfrac{1}{R_b(x) C_e(m)}} + V_{test} \frac{C_{test}}{C_e(m)} \tag{6.5}$$

V_o contains V_{ecg} multiplied by the high-pass filter transfer function merged with the test signal modulated by $C_{test}/C_e(m)$. Hence, V_o behaves similarly to the output of Fig. 6.1a, but with a signal that changes its amplitude according to the variations of C_e. Note that V_{test} should be a large signal so it is still measurable after being attenuated by $C_{test}/C_e(m)$, and its frequency must be greater than ECG's highest frequency of interest to allow filtering from the V_{ecg} component.

Figure 6.2 shows a simplified block diagram of R_b's control loop. The summing junction with V_1, V_2, and V_o models the input stage shown in Fig. 6.1b. V_o is followed by a high-pass filter (HPF) that removes the ECG component. The HPF's output is $V'_{o,HPF} = V_{test} C_{test}/C_e(m)$. The cut-off frequency of this stage should be as close as possible to the frequency of V_{test} to quickly eliminate MA interference in the control loop.

The next stage is an inverting amplitude detector, which converts the AC signal into a DC voltage with the negative amplitude. Hence, the sensed amplitude (V'_{aptd}) is given by (6.6), where $\hat{V}_{test}$ is the peak value of V_{test}. The amplitude detection could have been done in a later stage, however, processing the signal as a DC voltage eases the gain-bandwidth product demand of the next stage: an inverting amplifier.

$$V'_{aptd} = -\hat{V}_{test} \frac{C_{test}}{C_e(m)} \tag{6.6}$$

The inverting amplifier's gain is given by a resistor relation, where the feedback resistor has an arbitrary value (R) and the input resistor is a copy of $R_b(x)$. Hence, the stage's gain

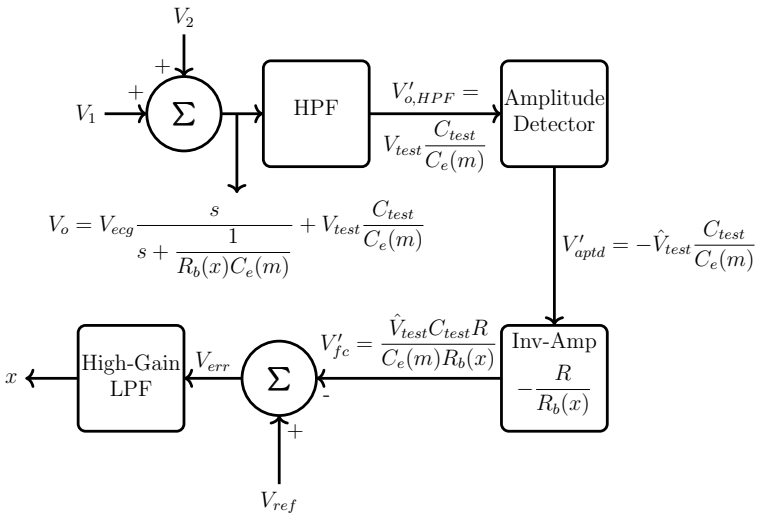

Figure 6.2: Simplified block diagram of the proposed control loop

is $-R/R_b(x)$, and the stage's output is the sensed low cut-off frequency (V'_{fc}) given by (6.7). Thus, V'_{fc} (6.7) follows f_l (6.4).

$$V'_{fc} = \hat{V}_{test}\frac{C_{test}R}{C_e(m)R_b(x)} \tag{6.7}$$

Because V'_{fc} is not exactly f_l, but a value proportional to it, V_{ref} must be designed according to the constant $C_{test}R$. Also, it is an in-phase signal, so it must be subtracted from the reference in order to create an error signal (V_{err}). The controller consists of a high-gain low-pass filter (LPF), which generates signal x that controls R_b. The gain acts as a proportional controller and the LPF sets the response time.

To exemplify the operation, let's consider that a motion m reduces C_e and thus f_l rises. Then, V'_{aptd} becomes larger in the negative direction, and the inverter's output increases. Further, V_{err} goes negative, and consequently so does x. If the resistance of R_b is inversely proportional to x, R_b increases and compensates for the decrease in $C_e(m)$.

6.2 Circuits Description

The development of such a control loop can be carried out in different ways. The input node (Fig. 6.1b) is necessarily analog, but the stages in the control loop can be digital. Moreover, many of the stages could be implemented with off-the-shelf components. Here, we decided to approach the circuit design in an all-analog integrated manner.

The CMOS technology chosen was the TSMC 65nm general purpose (GP), where the

analog front-end and control loop can be built, reducing the electrode's PCB area/density. We preferred to process the signal on-chip rather than in the main system's processor because in a multi-electrodes system, such as an ECG mattress [17], off-chip processing greatly increases the number of I/O ports. Hence, in the proposed design, each electrode has its independent f_l control loop.

Thick oxide devices were used to allow a single supply voltage (VDD) of 2.5 V. V_{test} is a square wave ranging from 0 V (GND) to 2.5 V (VDD) with a frequency of 1 kHz, which is one decade greater than the maximum frequency of interest in our ECG (100 Hz). Increasing the frequency of V_{test} makes the filtering from the ECG signal easier, as the bands of operation become farther apart. However, the frequency was restricted to 1 kHz so that the amplifiers do not need to operate at high frequencies. Figure 6.3 translates the simplified block diagram (Fig. 6.2) into the circuit's schematic. All capacitors used in this work were metal-insulator-metal (MIM) capacitors.

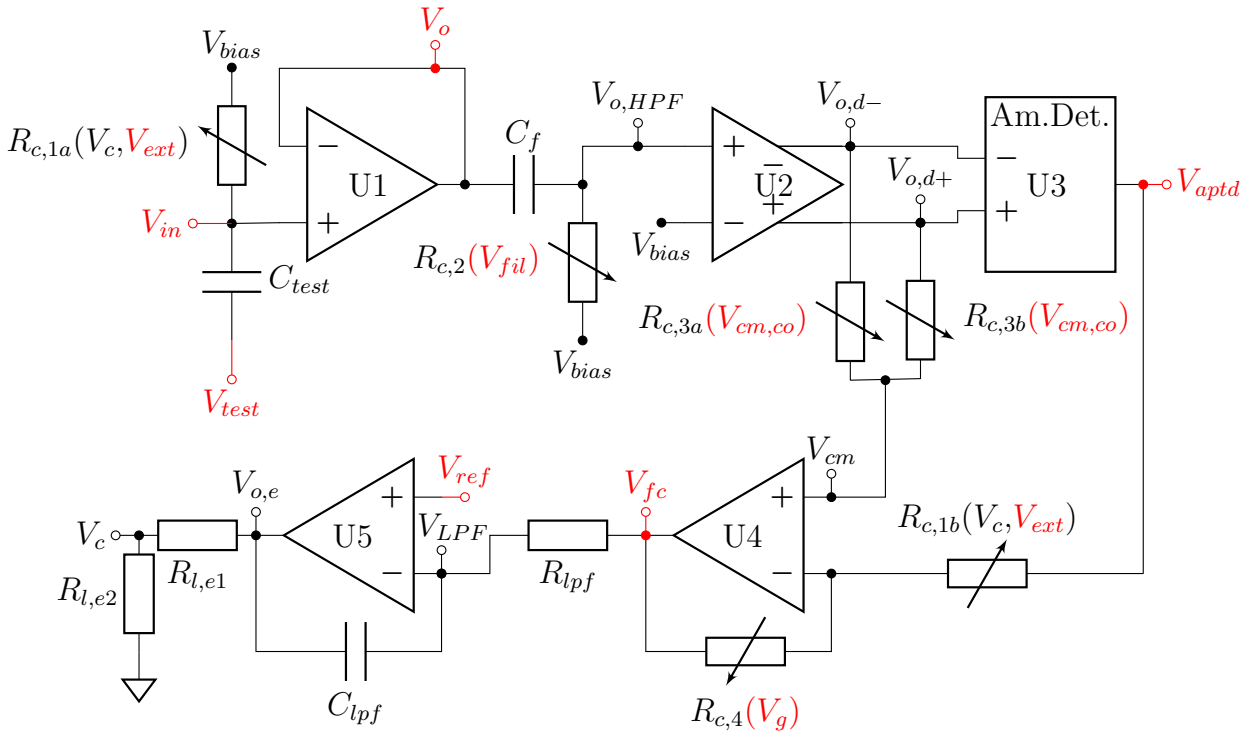

Figure 6.3: Circuit schematic of a capacitive electrode with f_l control, colored voltages are connected to the outside of the chip

6.2.1 ESD Protection

In Fig. 6.3 the red colored voltages mean that the node is connected to a pad and is accessible from the chip's outside. All pads have an Electrostatic discharge (ESD) protection

circuit and the power supply is connected to a power clamp. The ESD protection from the technology's library adds a minimum of 100 fF that could be tolerated everywhere except the input node (V_{in}). This happens because C_e can be as small as 1 pF and would form a voltage divider with the parallel of C_{ESD} (100 fF) and C_{test} (40 fF). Thus, without accounting for U1's input capacitance, the gain of this voltage divider is 0.88 V/V.

In the worst-case scenario, the target is less than 10% of attenuation of V_{ecg} due to voltage division. Therefore, the bootstrapped ESD protection topology of Fig. 6.4 was used at the node V_{in} [91]. The bootstrapping technique is widely used to boost impedances, either increasing resistance or decreasing capacitance. It consists of buffering the voltage in one terminal of a component and reapplying it to the other terminal [68], [70]. Hence, the voltage drop on the impedance is 0 V and no current flows through it.

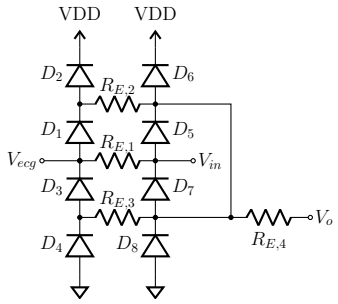

Figure 6.4: Bootstrapped ESD protection circuit

In Fig. 6.4, the IC's pad containing the sensed ECG signal (V_{ecg}) is connected to the buffer's input V_{in} through the ESD protection circuit. Note from Fig. 6.3 that V_o is the output of the input buffer, and hence a copy of V_{in}. The resistors $R_{E,1}$ to $R_{E,4}$ are of 500 Ω and protect the circuit from latching-up. In normal operation, $V_o = V_{in} = V_{ecg}$, thus all diodes are off and no current flows through the stray capacitance of diodes D_1, D_3, D_5 and D_7 because they are bootstrapped. When an ESD event (or large voltage MA) happens, diodes D_2 and D_6 clamp to VDD in case of positive voltages and diodes D_4 and D_8 clamp to GND for negative artifacts. Then, the odd-numbered diodes are not bootstrapped anymore and will also conduct, creating low-resistance paths. Once the input node is discharged and the diodes stop conducting, the bootstrapping returns, and the high impedance is re-established.

6.2.2 Pseudo-Resistors

In this work, three types of pseudo-resistors (PR) are used and are shown in Fig. 6.5. The input node V_{in} is connected to a high-linearity controllable pseudo-resistor (HLCPR) $R_{c,1a}$, detailed in Fig. 6.5a [88], which performs the role of R_b in Fig. 6.1b. The demand

for high linearity does not come from $R_{c,1a}$ but from $R_{c,1b}$ (see Fig. 6.3), yet, they must be equal for a correct inference of f_l at node V_{fc}. The HLCPR requires a control circuit which is shown in Fig. 6.5b.

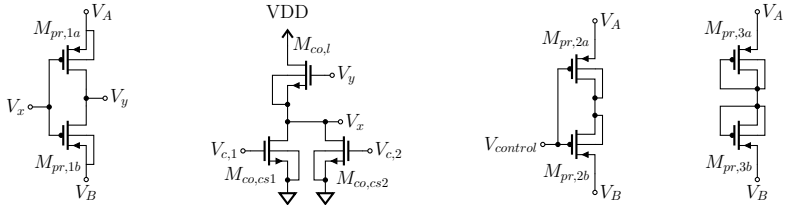

(a) High-linearity CPR (HLCPR)

(b) HLCPR control

(c) standard CPR

(d) fixed resistance PR

Figure 6.5: Topologies of PRs used in this work

The higher linearity of the HLCPR (Fig. 6.5a) compared to the standard CPR (Fig. 6.5c) comes at a cost of a relatively complex control circuit. The HLCPR is controlled by a differential voltage (V_{yx}), while the standard CPR requires a single-ended control voltage ($V_{control}$). Moreover, the smaller the control voltage is, the higher the resistance is. In general, V_{yx} (tens of mV) is significantly smaller than $V_{control}$ (hundreds of mV) to achieve similar resistances [88].

The circuit of Fig. 6.5b has two NMOS current sources ($M_{co,cs1}$ and $M_{co,cs2}$) and an NMOS load ($M_{co,l}$) with body and source connected [86]. V_{c1} and V_{c2} allow automatic or external control of the HLCPR. To turn off the control current sources, V_{cx} should be grounded. To reach a V_{yx} (V_{gs} of $M_{co,l}$) of a few mV, the current flowing in $M_{co,l}$ must be unusually small (pA range) [92]. To achieve such a small current the body has to be connected to the source to avoid leakage, thus $M_{co,l}$ is a triple-well NMOS. $M_{co,cs1}$ and $M_{co,cs2}$ have a small W/L to minimize the conversion of $V_{c1,2}$ into a drain current I_d. $M_{co,l}$ has a large W/L also to minimize the conversion of I_d into V_{yx}.

The reason for having two control signals, V_{c1} and V_{c2}, is the capability of controlling $R_{c,1a}$ and $R_{c,1b}$ in closed loop with V_c or in open loop with V_{ext}. To ground V_{ext}, the pad of the IC should be connected to the external ground. To ground V_c, the pad V_{ref} should be grounded, hence V_c is forced to be zero. Further, controlling the system externally allows calibration and implementation/testing of other forms of control.

6.2.3 Input Buffer

The input buffer used in this work is a bootstrapped buffer due to its ultra-low input capacitance [29]. Its transistor-level schematic is shown in Fig. 6.6a. By using this topology, the input capacitance is minimized to attenuate voltage division with C_e and C_{test}. Note that V_o is connected not only to the inverting input of the amplifier but also to both cascoded devices' gates ($M_{d,1c}$ and $M_{d,2c}$). Moreover, the PMOS transistors' bodies in the cascoded differential pair are tied to the source of $M_{d,1}$ and $M_{d,2}$.

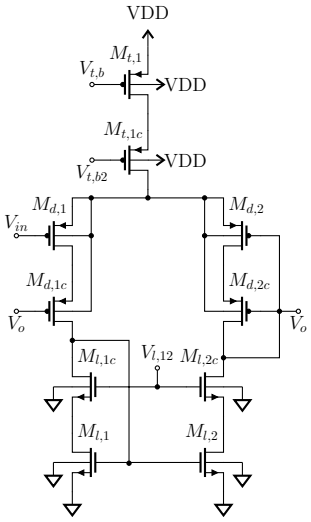

(a) Bootstrapped buffer: U1 with connections

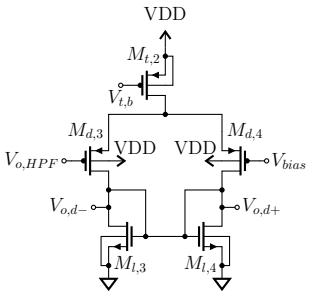

(b) Differential amplifier (U2)

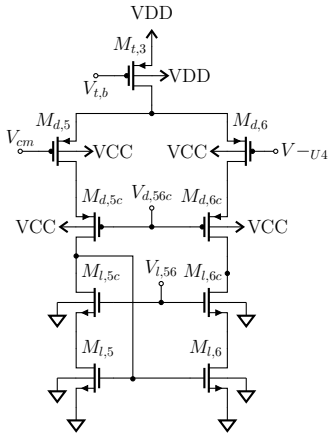

(c) High gain opamp (U4)

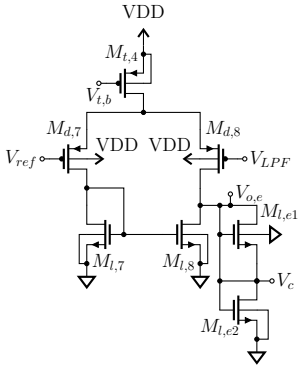

(d) Error amplifier: U5 with voltage divider load

Figure 6.6: Amplifier topologies used for U1, U2, U4 and U5

For a better understanding of this circuit's dynamics, one can refer to Fig. 6.7, where a partial small-signal model is provided. In this schematic, R_{tail} is the resistance seen in the

cascoded current source ($M_{t,1}$ and $M_{t,1c}$), which for simplicity of analysis is approximated to infinity. Ideally, the gain of the buffer is unity and hence $V_o = V_{in}$. Therefore, in small signal, $V_{tail} = V_{in}$ to satisfy the nodal equations at the V_{tail} node, and both C_{gs} and C_{gb} are bootstrapped. In other words, since there is no current in R_{tail}, the voltage drop in $1/gm_{d1}$ and $1/gm_{d2}$ is zero and so is the current. Similarly, assuming that the gate current is null, the voltage at $M_{d,1}$'s drain must be equal to V_{in} to zero the current flowing through $1/gm_{d1c}$ resistor. Thus, C_{gd} is also bootstrapped.

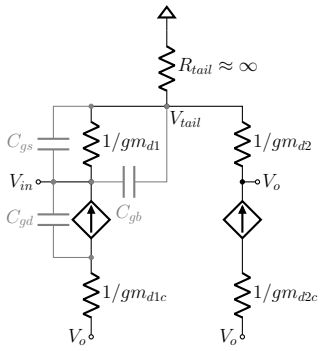

Figure 6.7: Bootstrapping of $M_{d,1}$'s gate capacitances

6.2.4 HPF and Single-to-Differential Amplifier

In Fig. 6.3, the MIM capacitor C_f of 5 pF forms a high-pass filter (cut-off frequency of 200 Hz) with CPR $R_{c,2}$, which is controlled by an external voltage V_{fil}. This control voltage allows for the tuning the filter's cut-off frequency if the frequency of V_{test} is changed and to compensate for the inaccuracy in the pseudo-resistors models and PVT variations [93]. The voltage at the HPF's output $V_{o,HPF}$ is expected to be in CPR's linear region and it is not necessary to use an HLCPR, thus it saves area by avoiding the need for the control circuit.

The signal $V_{o,HPF}$ is converted to the differential mode by a differential pair ($M_{d,3,\&4}$) loaded on both sides with diode-connected devices ($M_{l,3\&4}$), as shown in Fig.6.6b. The sizes of the differential pair's transistors set the differential gain to unity, while the size of the load devices sets the common-mode at the differential outputs to V_{bias}. In this stage, matching is important because the next stage consists of measuring the common-mode and amplitude, therefore, the circuit was laid out as common-centroid structures.

6.2.5 Common-Mode Measurement and Amplitude Detection

The outputs of the differential amplifiers, $V_{o,d+}$ and $V_{o,d-}$, are the inputs of the common-mode sensing circuit and the amplitude detection circuit. The common-mode sensing circuit

consists of two HLCPR in series, connected between $V_{o,d+}$ and $V_{o,d-}$, where the midpoint is the common-mode level of the output of $U2$, denoted as V_{cm} in Fig. 6.3.

HLCPRs were chosen because their ultra-high resistance leads to negligible voltage drop which combined with the high linearity improves accuracy. The controllable topology is preferred over the fixed-resistance PR because this node is one of the main contributors to noise. The resistance value controls the thermal noise and also sets a pole with the input capacitance of U4 in Fig. 6.3 (gate capacitance of M_{d5} in Fig. 6.6c). Thus, by controlling the resistance one can reduce noise and adjust the pole of the common-mode loop.

The amplitude detection circuit in Fig. 6.8 consists of two bidirectional transmission gates, connected in series. The midpoint is the sensed amplitude (V_{aptd}), one external node is connected to $V_{o,d+}$ while the other external node is connected to $V_{o,d-}$, as depicted in Fig 6.8. The gates are clocked with V_{test} or an inverted version of it ($\overline{V_{test}}$).

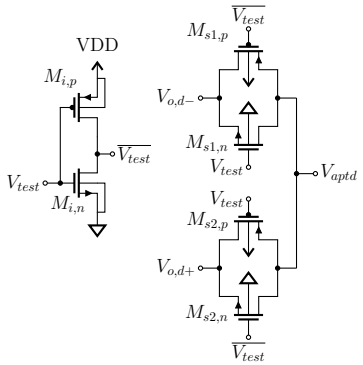

Figure 6.8: Amplitude detector (U3)

The circuit works as a switched rectifier synchronized with the negative cycle. $V_{o,d+}$ and $V_{o,d-}$ can be approximated to $V_{cm} + {}^{V_{test}C_{test}}/_{C_e(m)}$ and $V_{cm} - {}^{V_{test}C_{test}}/_{C_e(m)}$, respectively. Recall that V_{test} is a square wave with amplitude of 2.5 V (GND to VDD). When V_{test} is in the positive cycle, it turns on $M_{s1,p}$ and $M_{s1,n}$, and $V_{o,d-}$ (which is at the negative cycle) passes through the transmission gate. During the negative cycle of V_{test}, $M_{s2,p}$ and $M_{s2,n}$ are switched on and $V_{o,d+}$ (in phase with V_{test}) goes to V_{aptd}. Therefore, $V_{aptd} = V_{cm} - {}^{\hat{V}_{test}C_{test}}/_{C_e(m)}$.

6.2.6 Inverting Amplifier

Referring to Fig. 6.3, the inverting amplifier stage consists of a high gain opamp (U4, Fig. 6.6c) with one HLCPR in the negative feedback ($R_{c,4}$) and another HLCPR ($R_{c,1b}$) inputting the sensed amplitude (V_{aptd}) to "$V-_{U4}$". The same cell (layout) was used for both HLCPRs. However, note in Fig. 6.3 that $R_{c,1b}$ is controlled by the same voltages as $R_{c,1a}$

(V_c and V_{ext}), while $R_{c,4}$ is controlled by V_g, hence the other control pin is tied to ground.

The gains seen by the non-inverting input (6.8) and by the inverting input (6.9) of the amplifier lead to an expression for the sensed low cut-off frequency (V_{fc}) (6.10). Because $R_{c,1b} = R_{c,1a}$, we can write as (6.10), where ω_l is the low cut-off frequency in radians per second.

$$V_{fc,ninv} = V_{cm}\left(1 + \frac{R_{c,4}}{R_{c,1b}}\right) \tag{6.8}$$

$$V_{fc,inv} = -\left(V_{cm} - \frac{\hat{V}_{test}C_{test}}{C_e(m)}\right)\frac{R_{c,4}}{R_{c,1b}} \tag{6.9}$$

$$V_{fc} = V_{fc,ninv} + V_{fc,inv} = V_{cm} + \hat{V}_{test}\frac{C_{test}R_{c,4}}{C_e(m)R_{c,1b}} = V_{cm} + \hat{V}_{test}R_{c,4}C_{test}\omega_l \tag{6.10}$$

Besides showing that V_{fc} is proportional to f_l, (6.10) also provides important information for the design of U4. The value of C_e is assumed to be in the range of 1 pF to 100 pF, hence the gain of the inverting amplifier must be capable of changing by two orders of magnitude. Designing the gain to be unity when the input signal is at its highest value (C_e =1 pF) forces the gain to be 100 V/V when C_e is 100 pF. Thus, the open-loop gain of U4 must be much greater than 100 V/V, and the telescopic cascode topology of Fig. 6.6c led to a gain of 8000 V/V.

The tail current source is not cascoded to allow more voltage headroom for the changes in the input and output. As mentioned before, the amplitude detector comes before the inverting amplifier rather than after because of bandwidth constraints. The input PR ($R_{c,1b}$) sees the parallel combination of the gate capacitance of $M_{d,6}$ with the Miller-boosted parasitic capacitance of $R_{c,4}$. Hence, a low pass filter is formed at $V-_{U4}$ and its cut-off frequency is lower than the frequency of V_{test}. Thus, processing in AC mode is not possible, but one can take advantage of this low-pass filtering to remove switching spikes from the amplitude detector.

6.2.7 Low-Pass Filtering and Error Amplifier

The high cut-off frequency of the inverting amplifier varies with the value of $R_{c,1b}$ because it changes both the resistance and total capacitance (Miller's capacitance depends on the gain). Therefore, if the dominant pole of the whole control loop is the inverting amplifier's pole, the loop will not have a well-defined settling time and phase margin. That could lead to instability of the system and oscillation.

To create the control loop's dominant pole, R_{lpf} (implemented with a fixed-resistance PR

from Fig. 6.5d) forms a low-pass filter with the 200 fF MIM capacitor C_{lpf} (between V_{LPF} and $V_{o,e}$ in Fig. 6.3). The capacitor is in negative feedback with opamp U5 (Fig. 6.6d), which has an open-loop gain of approximately 70 V/V. Thus, C_{lpf} is also a Miller-boosted capacitance and sets the pole to very low frequencies. The resulting cut-off frequency of the LPF is 100 mHz

In Fig. 6.6d, transistor $M_{d,7}$ has a current that follows V_{ref}, while the current in $M_{d,8}$ is a function of V_{LPF}. At node $V_{o,e}$ these currents are subtracted, and the remaining current (error current) passes through $M_{l,e1}$ and $M_{l,e2}$. Because V_c can be in the range of 200 mV, one cannot take the control signal at $V_{o,e}$ as such a low voltage could put $M_{l,8}$ in triode and unbalance the current mirror. However, working with $M_{l,e1}$ and $M_{l,e2}$ in sub-threshold (BJT-like operation) is not a problem. Moreover, these diode-connected devices generate large DC voltages for small DC error currents, while presenting low small-signal resistances.

6.2.8 Physical Implementation

The fabricated IC is packaged into a CFP24 (CCF02414 by spectrum-semi) leaded chip carrier ($U3$ in Fig. 6.9). It is soldered onto a 4-layer PCB, which also comprises buffers and filters to aid in testing/debugging ($U2$ in Fig. 6.9). The top layer contains the components, the top inner layer has the supply voltages (VDD and GND), while the bottom inner layer is a large area of shielding, which bootstraps the bottom/sensing layer. The sensing area is a square with a side of 31 mm, surrounded by a guard ring. The bottom layer is fully covered by the solder mask, which acts as the electrode's dielectric.

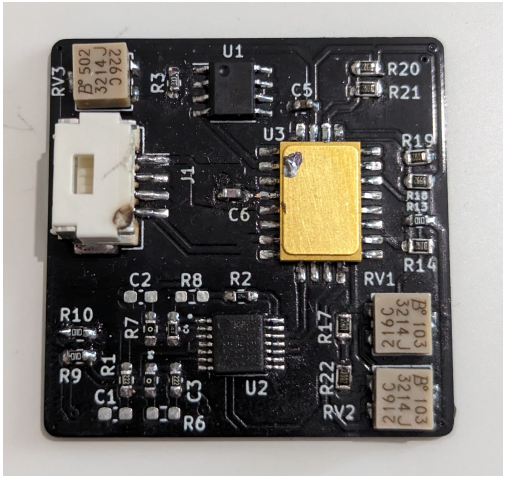

Figure 6.9: Assembled electrode

The 2 µA bias current is generated externally to the proposed IC by an LM334 ($U1$ in Fig. 6.9). The 1 kHz test signal was generated in the main ECG board and sent through a

wire to the electrode. External reference voltages are required, such as V_{ref}, V_g, $V_{cm,co}$, thus the 2.5 V supply was regulated to avoid fluctuations. The main board, presented in Fig. B.1, differences, amplifies, and filters the signal from two electrodes. Then it is sent to a laptop for digital signal processing.

6.3 Results

6.3.1 Simulations

Before evaluating the system's performance in a closed-loop, it is necessary to measure the accuracy of the f_l sensing mechanism, which is displayed in Fig. 6.10. This is achieved by setting V_{ref} to 0 V and finding the value of V_{ext} that leads to a f_l of 0.5 Hz in an AC simulation for multiple values of C_e. The accuracy of V_{ext} is limited to the closest mV, and values of C_e tested are: 1 pF, 2 pF, 4 pF, 6 pF, 10 pF, 20 pF, 40 pF, 60 pF, and 100 pF.

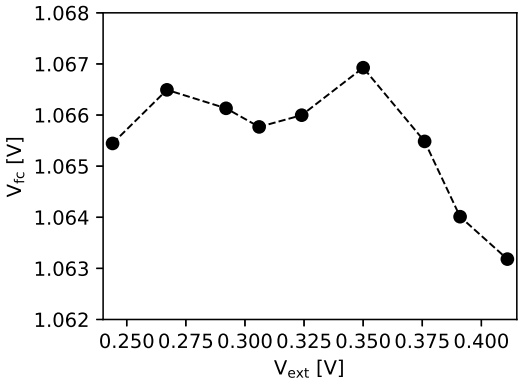

Figure 6.10: V_{fc} for different values of C_e and ideal values of V_{ext} that sets f_l to 0.5 Hz

In Fig. 6.10, the lowest value of V_{ext} is associated with the smallest C_e, whilst the highest V_{ext} sets the cut-off for the highest C_e. For the first seven values of V_{ext}, V_{fc} lies between 1065 mV and 1067 mV, however, for the two largest values, V_{fc} is 1064 mV and 1063 mV. The average value of V_{fc}, rounded to the closest mV, is 1065 mV. Removing V_{cm} of 1000 mV, the variation of V_{fc} is of $\pm 3\%$.

Ideally, these values should match exactly, however, due to methodology limitations and artifacts introduced by the circuit, inaccuracy is expected. For example, by using the closest mV, an error of up to 0.5 mV is added to V_{ext}. The major circuit-related contributors to errors are the inaccuracy/variation of V_{cm} when the amplitude of $V_{o,HPF}$ is small, non-linearity of the inverting amplifier gain as a function of $R_{c,1b}$, and non-linearity of $R_{c,1b}$ and $R_{c,4}$ due to the signal amplitude.

The AC sweep simulation of the system in an open-loop, with V_{ext} set to lead to a low-cut off frequency of 0.5 Hz (V_{ref} is grounded), is shown in Fig. 6.11a. The curves displayed are measured at V_o for a unitary input, hence they are equivalent to the gain. Three values of C_e are tested, 1 pF, 10 pF and 100 pF and the respective control voltages (V_{ext}) are 244 mV, 324 mV and 411 mV.

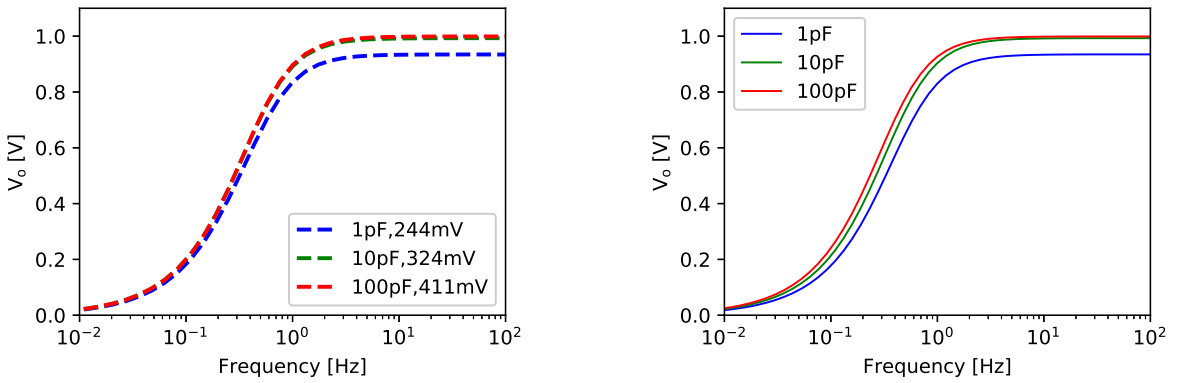

(a) Open-loop ideal frequency response, V_{ext} was set to the value that leads to f_l of 0.5 Hz, legend in the format C_e,V_{ext}

(b) Closed-loop frequency response, with V_{ref} of 1065 mV

Figure 6.11: Frequency response of the proposed system in open-loop and closed-loop with different electrode capacitances, the targeted f_l is 0.5 Hz

The simulated mid-band gains are 0.932 V/V, 0.992 V/V and 0.999 V/V for C_e of 1 pF, 10 pF and 100 pF, respectively. The difference in gain from one electrode capacitance to another is explained by the non-ideal input capacitance. From (6.2) it is known that V_{ecg} sees a voltage divider between C_e and C_{test}. Moreover, one should account for the stray capacitance not eliminated by the bootstrapped ESD protection and bootstrapped input buffer, which is in parallel with C_{test}. The simulated input capacitance is 73 fF, accounting for ESD protection, routing and C_{test}.

From Fig. 6.10, the average V_{fc} that sets f_l to 0.5 Hz is 1065 mV. Therefore, this is the value used as V_{ref} in closed-loop gain. Moreover, V_{ext} must be grounded to turn off the external control. Because the control loop is periodically time varying due to the switching (V_{test}), standard AC sweeps cannot be used for this simulation, then periodic AC (PAC in Spectre) must be performed. This sort of simulation differs from a regular AC sweep because it first accounts for the circuit's settling time. Therefore it computes the AC parameters based on steady-state DC operating points created by the switching of the amplitude detection. The values of C_e tested are the same three used in Figure 6.11a.

Figure 6.11b shows the frequency response of the proposed system with the control loop.

The pass-band gains are the same as in Fig. 6.11a. Although the PR's parasitic capacitance depends on the control voltage/resistance, the differences between the ideal values V_{ext} and resulting values of V_c are small. Thus, the parasitic capacitance is approximately the same in both open and closed loops.

The measured values of f_l in the PAC simulation were 402 mHz for C_e=100 pF, 454 mHz for C_e=10 pF, and 517 mHz for C_e=1 pF. For the three tested values of C_e, f_l fluctuated within 115 mHz range, while the maximum error to the targeted f_l was 98 mHz. In comparison to a fixed bias resistance system, variations of C_e between 1 pF and 100 pF can lead to f_l fluctuations of up to 2 decades.

Another parameter that was simulated was the noise. There are two nodes that are sensitive to noise in the proposed circuit, V_o and V_c. Table 6.1 summarizes the measured integrated RMS noise voltages in both nodes. The frequency sweep and integration range was from 1 mHz and 1 kHz for the noise at V_c. While for V_o, the integration band lied between 0.5 Hz and 100 Hz, which is the ECG bandwidth.

C_e [pF]	Noise @ V_o [μV_{rms}]	Noise @ V_c [mV_{rms}]
1	59.2	0.29
10	24.2	0.33
100	17.6	1.84

Table 6.1: Integrated noise at V_o and V_c for three values of C_e

The largest RMS noise at V_o is 59.2 µV when C_e is 1 pF. The noise at V_o in the capacitive electrode is dominated by interactions of the input current noise with C_e and the bias resistor. More specifically, the current noise of the input buffer is multiplied by the parallel of the bias resistor and the total capacitance seen in the input ($\approx C_e$), thus the smallest C_e becomes, the largest the noise at V_o is [29], [62]. For a C_e of 10 pF and 100 pF, the RMS integrated noise is 24.2 µV and 17.6 µV, respectively. Compared to the open loop circuit, the addition of the control loop had negligible impact on noise within the ECG bandwidth.

Noise at the control voltage was monitored because it could change the value of the bias resistor and hence lead to fluctuations in f_l. At node V_c, the most significant RMS noise (1.84 mV) takes place when C_e is maximized. This phenomenon is the result of the higher gain in the inverting amplifier when the capacitance is high. However, V_c is the largest when the noise is also the largest, therefore the ratio between noise and signal amplitudes is partially compensated.

To understand more about the signal flow and output characteristics, a transient analysis was run and evaluated in different conditions and nodes. The first results are the settling times and steady-state waveforms of V_{fc} and V_c. Figures 6.12a and 6.12c show the behavior

of those nodes from time 0 s (start-up) until 700 ms (steady-state), while Figs. 6.12b and 6.12d show the steady-state waveforms. The simulations shown in Fig. 6.12 are the results of a conservative analysis with transient noise in the range of 1 Hz to 100 Hz.

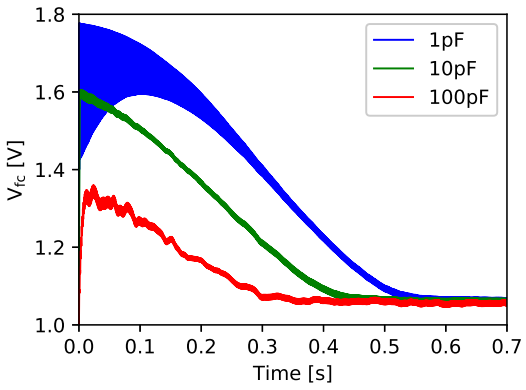

(a) V_{fc} from start-up to steady-state

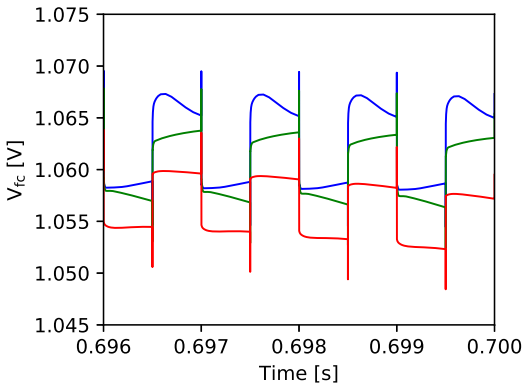

(b) Steady-state waveform of V_{fc}

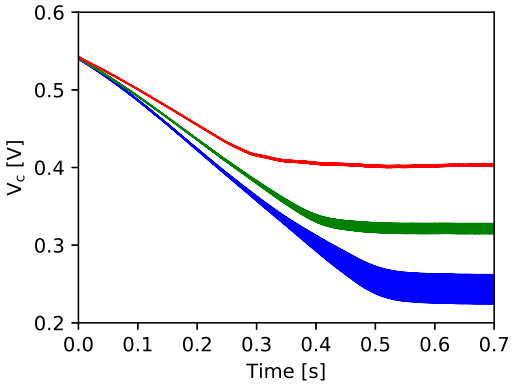

(c) V_c from start-up to steady-state

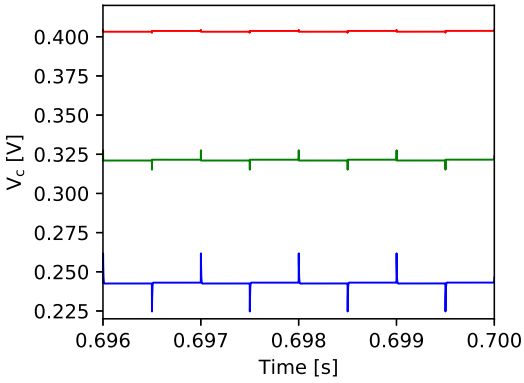

(d) Steady-state waveform of V_c

Figure 6.12: Transient response from start-up to steady-state at nodes V_{fc} and V_c, when C_e is 1 pF, 10 pF and 100 pF. The color legend in (a) is also valid for (b), (c) and (d)

The steady-state is reached at approximately 400 ms for C_e=100 pF, 500 ms for C_e=10 pF and 600 ms for C_e=1 pF. Comparing Figs. 6.12a and 6.12c, one can notice that node V_c settles slightly slower than V_{fc} due to the strong LPF between these nodes. Note that the steady-state is reached within half period of the cut-off frequency (2 s). Thus, in the case of severe MA, less than half of the slowest ECG harmonic is corrupted due to incorrect bandwidth.

At the start-up, both V_{fc} and V_c are higher than their steady-state values, meaning that the resistance of $R_{c,1a}$ is smaller than the value it should be. The control loop then starts to work, decreasing V_c which increases $R_{c,1a}$ and hence decreases f_l (and V_{fc}). Because the resistance increases almost linearly with V_c, it is expected that the time to reach higher

resistances is greater than to reach smaller resistances.

Figure 6.12b shows that the simulated V_{fc} is not a perfect DC voltage equal to V_{ref}, but a square wave centered close to V_{ref} (1065 mV). The square wave signal comes from unmatched peak voltages at $V_{o,d+}$ and $V_{o,d-}$, which after the rectification on the amplitude detector creates this waveform. This effect is seen equally for the three values of C_e. Figure 6.12b also shows the error of V_{fc} in relation to V_{ref}, as the average of the three curves should be 1065 mV.

The control voltage waveform, displayed in Fig. 6.12d, shows that the low-pass filter drastically reduces the undesired square-wave signal in V_{fc}. The average V_c is 403 mV, 321 mV and 243 mV, while the ideal values (from Fig. 6.10) are 411 mV, 324 mV and 244 mV. These results agree with the ones found in Fig. 6.11b, where for C_e=100 pF the f_l was lower than the targeted value and the error was the greatest.

Noise is present in this transient analysis and can be spotted in Fig. 6.12a for C_e=100 pF, especially before 0.1 s. During this period, the gain of the inverting amplifier is maximized, and noise reaches its highest value. The spikes in the waveforms of Fig. 6.12d are not caused by noise, but due to capacitive coupling with the trace carrying V_{test}. This trace was carefully designed in the layout and is guarded with ground lines on its top, bottom, and sides, whereas the ground of this guard has a separate trace to the ground pin. Yet, it still couples with the high impedance nodes such as V_{LPF}.

A sinusoid with amplitude 2 mV (peak-to-peak) and frequency of 0.5 Hz was applied to V_{ecg} and V_o was measured. Because V_o also contains part of V_{test}, the results shown in Fig. 6.13a were low-pass filtered (5 Hz) to remove the high-frequency test signal. The ideal amplitude of V_o for the 2 mV tone at 0.5 Hz is 1.414 mV, meaning that f_l is 0.5 Hz. The simulated amplitudes for the three values of C_e are 1.5 mV (C_e =100 pF), 1.3 mV (C_e =10 pF) and 1.4 mV (C_e =1 pF).

The data of Fig. 6.13a was cubic-interpolated and re-sampled with a 2 kHz sampling rate. The Fast Fourier Transform (FFT) was computed and is shown Fig. 6.13b. At the fundamental frequency, the measured V_o for C_e of 1 pF, 10 pF, and 100 pF are 1.33 mV, 1.39 mV, and 1.54 mV. The Total Harmonic Distortion was computed with the harmonics shown in Fig. 6.13b, and the values (from smallest C_e to largest C_e) are 0.79%, 0.24%, and 0.24%. This means that artifacts in V_c does not distort the acquired signal considerably.

MA was emulated as a capacitance step during a transient simulation. The simulation starts with C_e of 100 pF (good contact), changing to 1 pF when time is 2 s (bad contact), and back to 100 pF at time equal to 6 s (good contact). The V_o response to a MA is depicted in Fig. 6.14a, where circuit's outputs with and without the control loop are compared. The bias resistance of the circuit without control was set to provide f_l of 0.5 Hz when C_e is 1 pF.

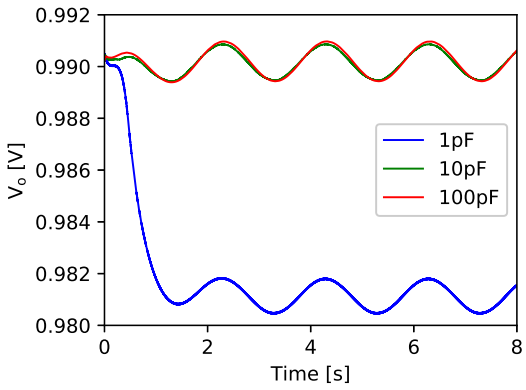

(a) Filtered V_o for a sinusoidal input of amplitude 2 mV and frequency of 0.5 Hz

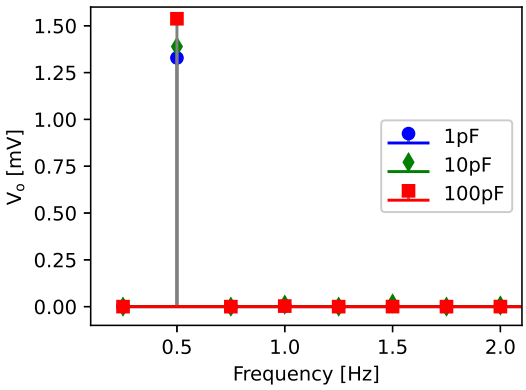

(b) FFT of signals from Fig. 6.13a sampled from 3.5 s to 7.5 s

Figure 6.13: V_o response to an input tone at the target f_l of 0.5 Hz in time and frequency domain

In the first step, C_e going from 100 pF to 1 pF, both curves in Fig. 6.14a peak at 3.2 V, which is the supplied VDD (2.5 V) plus the forward voltage of the protection diodes on that pin (0.7 V). This peak happens due to the rearrangement of the charges with the new capacitance.

Initially, the controlled circuit had the bias resistance minimized to comply with C_e of 100 pF. Hence, when the first capacitance step takes place, the settling time of the controlled circuits becomes smaller, and by the time the bias resistance increased to correct f_l, the node was already discharged. The opposite happens in the uncontrolled circuit, where the resistance is maximized and the settling time is longer. The controlled circuit reaches steady-state almost instantaneously (50 ms), while the uncontrolled circuit needs 2 s to completely settle.

The worst-case scenario in terms of settling time is the change from bad to good contact because C_e increases and so does the settling time. For the uncontrolled circuit, the maximized bias resistance leads to a f_l of 0.005 Hz and a τ_l of 32 s ($1/2\pi f_l$). After the step, the controlled circuit presents a large time-constant, however, it decreases as the input resistance is lowered. Therefore, the controlled circuit requires 2 s to return to its baseline of 1 V while the uncontrolled circuit is far from the steady-state, whereas the calculated settling time (5τ) is 160 s. One could argue that a simple high-pass after V_o removes the DC error, however, because the input node is not fully discharged, new MA events would be worse and could easily saturate the input node.

Figure 6.14b shows how the MA affects the f_l sensing. At both 2 s and 6 s, a negative spike followed by a positive spike is observed. These spikes are the high-frequency components of

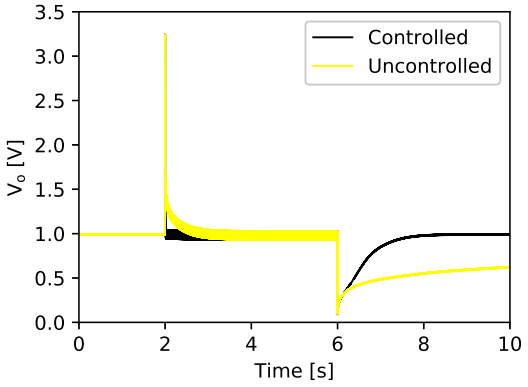

(a) Measured V_o in closed-loop and open-loop. In open-loop, V_{ext} is set to 411 mV so the bandwidth is enough to handle C_e as low as 1 pF

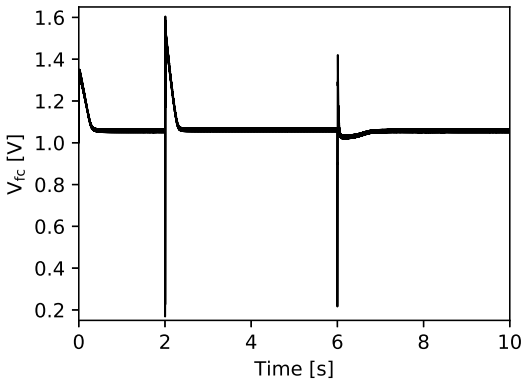

(b) V_{fc} response to a capacitance step

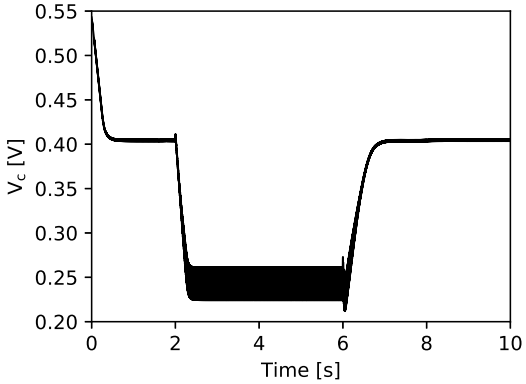

(c) V_c response to a capacitance step

Figure 6.14: Response to a capacitance step

V_o that passes the HPF formed by C_f and $R_{c,2}$. The higher the cut-off frequency of this filter is, the smaller the impact of MA on the control loop is. Moreover, the increase of this cut-off frequency should be accompanied by an increase in the frequency of V_{test}. Figure 6.14c shows that the low-pass filtering after V_{fc} removes those spikes, and the control voltage looks free from MA. In this figure, one can also notice that for the second capacitance step, the control loop reacts faster than the V_o's settling time, meaning that although V_o is not centered at 1 V the bandwidth is correct.

To demonstrate an ECG acquisition, the input source applies an ECG waveform to a single electrode. A capacitance step takes place at 7 s, changing the initial C_e of 100 pF to 1 pF until the end of the simulation. The signal was simulated at V_o, thus a digital 4^{th}-order low-pass filter with a cut-off frequency of 100 Hz was used to remove the test signal from the

output. This transient simulation contained noise from 0.1 Hz to 100 Hz.

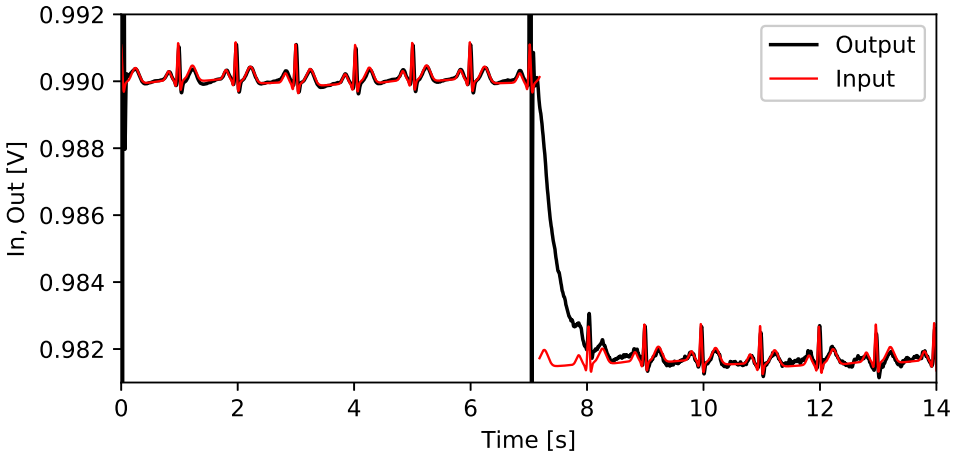

(a) Complete simulation

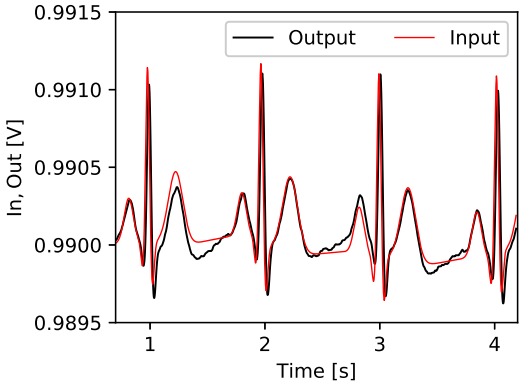

(b) C_e=100 pF

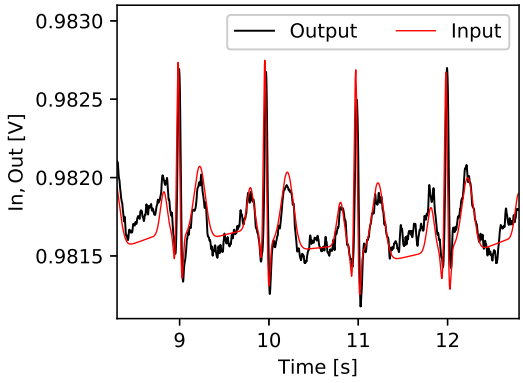

(c) C_e=1 pF

Figure 6.15: ECG input with offsets and filtered V_o for a capacitance step from 100 pF to 1 pF at 7 s

Figure 6.15 shows the acquired and the inputted ECG waveforms. The input has an offset of 0 V, however, it was split into two sections with different offsets, enabling the comparison between the input and the output. According to Fig. 6.15a, even with the addition of the low-pass filter, the output signal settles to the new baseline within 1 second. Hence, only one cycle of the ECG is lost.

For a more detailed comparison between output and input signals, Figs. 6.15b and 6.15c zoom into the two sections. When C_e is 100 pF, the noise is almost negligible, and the input and output overlap most of the time. The largest difference occurs in the T-P interval, where the output shows a steeper rise. When C_e is 1 pF, the noise increases considerably and is merged with a higher leftover of V_{test}. This was expected and was already predicted

by Table. 6.1 and (6.5). Yet, the P, Q, R, S, and T waves are still well-distinguishable.

6.3.2 Measurements

The proposed electrode's performance is compared to that of a standard electrode. This reference electrode is a single-supply variation of the one proposed in Chapter 5. Albeit the targeted cut-off frequency is 0.5 Hz, both proposed and standard electrodes could be tuned to provide other values of cut-off frequency. The electrode's sensing area is similar in both electrodes, and at least one dielectric layer is present, the PCB's solder mask. A capacitor of 100 pF is placed in series with the input to limit the maximum overall electrode capacitance. This is done to suppress the effects of heterogeneous contact pressure. Therefore, the standard electrode should have a cut-off frequency of 0.5 Hz when in direct contact (no clothing layers), while the proposed electrode's cut-off frequency should adapt to different dielectric layers and stabilize at 0.5 Hz.

The IC's cut-off frequency control accuracy was verified in practice. The test consisted of injecting a signal into a plain copper board and measuring the electrode's cut-off frequency with multiple cloth layers between the board and the electrode. A total of 3 T-shirts were applied, meaning that six layers of textiles posed as extra dielectrics between the electrode and the copper board. The results are shown in Fig. 6.16, where 0 "number of cloth layers" means that the electrode and the copper board were in direct contact. Note that the cut-off frequency was measured as 70.7% of the mid-band gain, taking into account the voltage division between electrode capacitance and input capacitance.

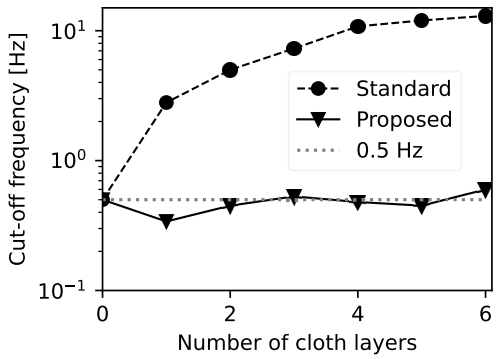

Figure 6.16: Cut-off frequency of the proposed and standard electrode for multiple layers of clothing

Fig. 6.16 shows that the proposed circuit's cut-off frequency is mostly overlapping with the 0.5 Hz reference line. The largest error for the proposed circuit happened for one layer of clothing when the cut-off frequency was 340 mHz, an absolute error 160 mHz or a relative

error of 32%. For two or more layers of clothing, the proposed electrode's cut-off frequency lies between 0.45 Hz and 0.6 Hz. Meanwhile, the standard electrode's cut-off frequency for a single layer of clothing was 3 Hz, an error of 500%. As expected, the error for the standard electrode increases as more layers are inserted. For six layers of clothing, the standard electrode's cut-off frequency was 13 Hz.

Recall that the advantage of the proposed topology does not come only from matching cut-off frequencies, but also from minimizing the recovery time after motion artifacts. Therefore, the next experiment presented emulates a capacitance step, and the results are shown in Fig. 6.17. To achieve that, a plastic sheet was used as a dielectric, and weight was applied on the top of the electrodes, pressuring them against the copper board with the test signal. The plastic sheet is then pulled and the electrodes fall over the copper board. Therefore, the capacitance between electrode and copper increases after the dielectric is pulled. The choice of dielectric was made so one could pull it smoothly, if cloth was used, it would stretch and drag the electrode instead of letting it slide.

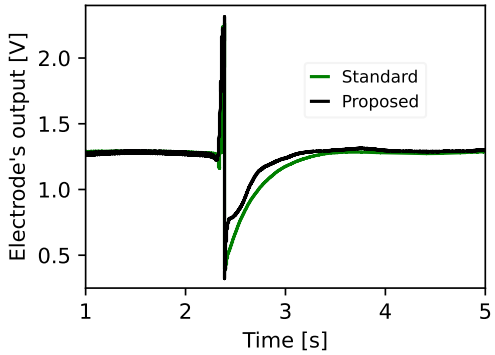

Figure 6.17: Settling time after a capacitance step for both standard and proposed electrodes

Initially, the cut-off frequencies were approximately 1.5 Hz (standard) and 0.5 Hz (proposed). After 2 s the plastic sheet is pulled and a motion artifact takes place. Note that not only capacitance changes are present but also triboelectric effects. The sliding effect creates a positive spike and as the electrode falls over the copper board a negative spike follows. After settling back to the baseline, the cut-off frequency of both electrodes was 0.5 Hz.

The time constant, calculated as 63% of the total change in voltage, is 0.23 s (proposed) and 0.31 s (standard). This means that even though the proposed circuit had an input resistance three times higher before the capacitance step, it discharged faster than the standard electrode. Similarly, if the standard electrode input resistance was set to provide the target cut-off frequency with the plastic dielectric, it would discharge three times slower.

The control loop constantly changes the input resistance to compensate for changes in

the electrode capacitance. However, the control signal is also vulnerable to noise, and it can undesirably change the input resistance. To measure the amount of distortion created by the control's signal noise, a sinusoid of 40 mV (peak to peak) at 0.5 Hz was applied to the copper coupling to the electrode via only the solder mask dielectric. From the point of view of noise, this represents the worst-case scenario because when the electrode capacitance is high, more gain is applied in the inverting amplifier of Fig. 6.3. The low-pass filtered output (with frequencies over 100 Hz removed) is shown in Fig. 6.18a and its FFT is displayed in Fig. 6.18b.

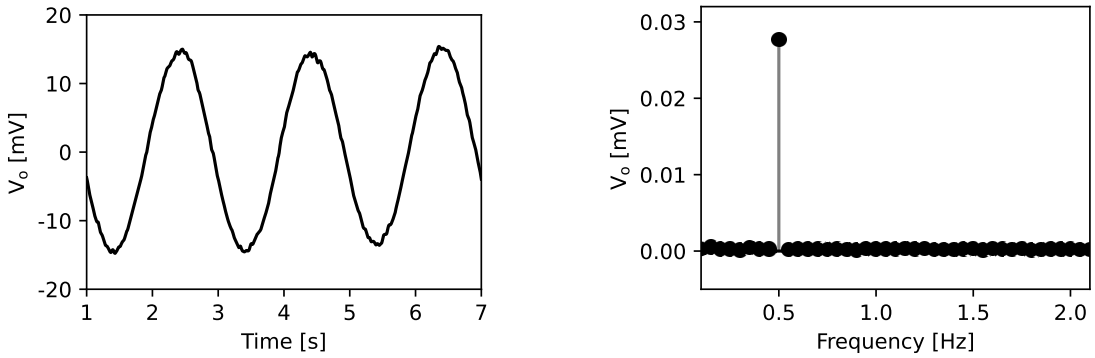

(a) Sinusoidal input at 0.5 Hz

(b) FFT

Figure 6.18: Measured THD of a sinusoidal input with a frequency of 0.5 Hz

From the FFT, the THD was calculated with 10 harmonics following the fundamental (0.5 Hz). The result was a distortion of 3%. If all FFT bins are used instead of the harmonics only, accounting for distortion and noise, the computation rises to 8.8%. As shown in Fig. 6.18, the most relevant factor to the increased distortion is the frequency content below 0.5 Hz.

An ECG acquisition is demonstrated in Fig. 6.19 by subtracting the signals from electrodes on the left and right side of the chest (RA-LA). The differential circuits, low-pass filter, and common-mode feedback are included in the analog processing board. The single-ended signal is acquired by a 16 bits ADC, low-pass filtered and decimated (oversampling for higher resolution), notch filtered (remove 60 Hz), and then smoothed with a Savitzky-Golay filter. A detailed description of our custom ECG system is provided in Appendix B. The ECG was obtained with both proposed and standard electrodes, through one or two T-shirts, in direct contact with skin (Skin), and with an electrode in direct contact and the other over the clothing (Mix).

In Fig. 6.19a, the results for the standard electrode are shown. The top curve shows the acquisition in direct contact with the skin, and the ECG characteristics can be easily

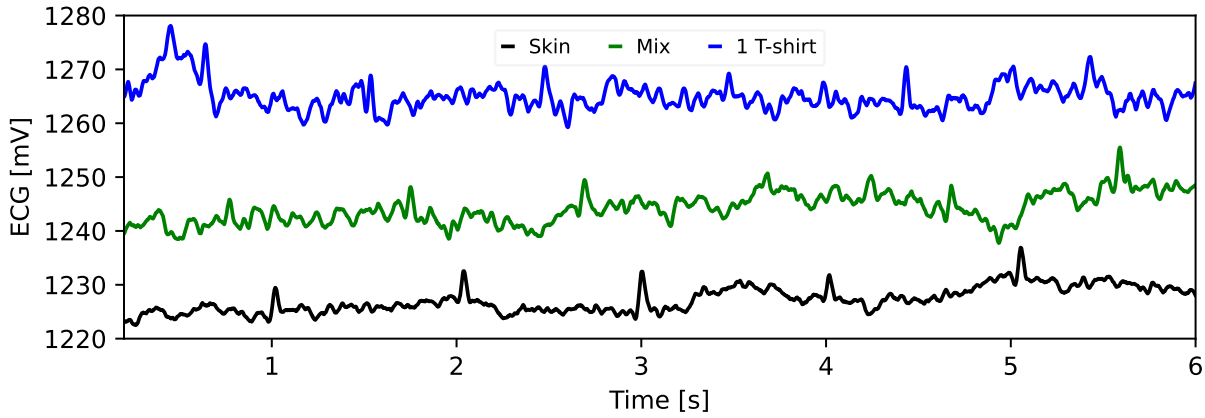

(a) ECG measured with a standard capacitive electrode

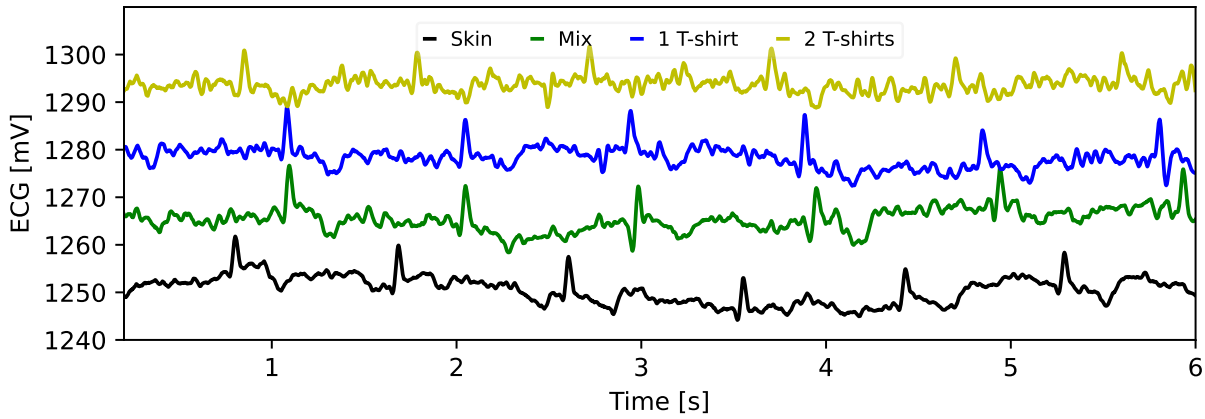

(b) ECG measured with the proposed capacitive electrode

Figure 6.19: ECG measurement with standard and proposed capacitive electrodes. The ECG was acquired in direct contact with the skin, through 1 or 2 T-shirts, and with one electrode contacting the skin and the other one over the clothing.

identified. When an electrode is placed over the T-shirt, the ECG waveform becomes less clear although still recognizable. Lastly, the ECG measurement over a T-shirt is even noisier, and the ECG characteristics can be mistaken for noise spikes.

The measurements with the proposed electrodes are presented in Fig. 6.19b. The ECG waveform with electrodes in direct contact with the skin, is as clear as the one provided by the standard capacitive electrode. The ECG with mixed conditions and one T-shirt presented slightly larger noise, however, most ECG features are still recognizable. The ECG acquisition through two T-shirts allows visual identification of the R-wave more easily than in the "Mix" and "1 T-shirt" cases of the legacy capacitive electrode. However, the smaller amplitude features of the ECG are merged with noise.

The improved performance of the proposed electrode over the standard electrode observed in Fig. 6.19 is explained by two factors. In "Mix", the standard electrodes' low cut-off frequencies do not match, thus errors are introduced due to the subtraction. This does not happen for the proposed topology because the control loop matches the low cut-off frequencies. For a single T-shirt, the standard electrodes do not have enough bandwidth, and in addition to that, the increased input resistance in the proposed electrode reduces the noise contribution of the bias resistor.

6.4 Discussion

In this chapter, the benefits of keeping a constant a constant low cut-off frequency (and time-constant) on the input node of a capacitive electrode are further explored. The proposed system consists of an all-analog integrated front-end that controls the input resistance locking the cut-off frequency at the targeted 0.5 Hz. Theoretical development with a block diagram and a circuit schematic provided the foundation for the proposed control loop, while post-layout simulations and practical measurements supported the initial hypothesis. However, the models rely on assumed idealistic behaviors, which are not seen in practice. Therefore, in this section the nonidealities that had impact in the results are discussed, as well as the limitations of the experiment.

A major element that contributes to the error in measuring f_l (Fig. 6.10) is the common-mode detection. When C_e is at its highest value, the part of (6.5) containing V_{test} is the smallest. Thus, the amplified subtraction of V_{aptd} and V_{cm} performed in the inverting amplifier is more susceptible to offsets/mismatches in both V_{aptd} and V_{cm}. This error is observed in Fig. 6.10, where the two highest V_{ext} (hence the two highest C_e) deviate from the rest and become smaller than the average V_{fc} of 1065 mV.

Accordingly, the simulated f_l in closed-loop for C_e equal to 1 pF, 10 pF, and 100 pF showed a maximum error of -98 mHz when C_e was 100 pF. This agrees with Fig. 6.10, where the largest negative error to the target values happens with C_e =100 pF. The measurement of f_l with clothing layers showed that the largest error (160 mHz) also occurred for a relatively large capacitance (1 layer of clothing), and f_l was smaller than the desired value.

From post-layout simulations, the total input capacitance seen from C_e was calculated as 73 fF and caused an attenuation in the input signal of 7.3% when C_e was 1 pF. Knowing that C_{test} is 40 fF, C_{par} is 33 fF. This range of input capacitance converges with [29], where the bootstrapped buffer's input capacitance was 60 fF. Note that in this work there is an extra capacitance C_{test} and the results are from extracted post-layout simulations. While in [29], the results are from practical measurements on the fabricated IC. Our packaged IC

presented an input capacitance of 1 pF and in future works the die will be wire-bonded to the PCB, however it was not a problem for the tests performed.

In both simulation and practice, the HLCPR ($R_{c,1a}$) can generate the range of resistances needed to establish an f_l of 0.5 Hz for C_e between 100 pF and 1 pF. By changing the value of V_{ref} one can modify the desired f_l, and although not presented here, $R_{c,1a}$ can achieve values high enough to provide an f_l of 0.05 Hz. This means that the 2.5 V thick oxide transistors available in TSMC 65 nm have negligible gate leakage and the choice of technology was appropriate.

Other than the f_l's accuracy, the constancy of the control signal V_c (which sets f_l) and how it could affect the ECG signal was investigated. As shown in Fig. 6.12, the control loop waveforms are not perfect DC voltages and are contaminated with spikes, noise, and the test signal. The low-pass filter between the inverting amplifier and the error amplifier drastically reduces noise and the square waves seen in the V_{fc}, leading to a cleaner V_c. The spikes in V_c are a result of the capacitive coupling between R_{lpf} and C_{lpf} with the V_{test} trace, which should be improved in the next iteration. Yet, the results from Fig. 6.18 confirm that there was not enough noise in V_c to significantly distort signals at the cut-off frequency, where THD was of only 3%.

The settling time was also an important feature of the proposed design. Figure 6.12c showed that the system takes 0.7 s to reach the steady state from the start-up moment. Complementary, Fig. 6.14a shows that after a large MA, the proposed circuit discharges much faster than the circuit with fixed ultra-high bias resistance. Fig. 6.17 showed that even if an electrode with the minimum allowed input resistance and diode-based discharging circuit is used, the proposed circuit discharges faster while maintaining the correct bandwidth.

The noise simulation showed that the proposed topology delivered output noise compatible with others presented in the literature. Significant noise was observed in the ECG of Fig. 6.19 when the signal was acquired through the clothing because the electrode capacitance drops. Moreover, additional noise is expected due to the resistive component of cotton. Yet, even in the worst-case scenario of noise, the ECG's R-waves were still recognizable in the proposed topology.

A methodology limitation on the ECG measurement is the electrode placement. Misalignment could be present because the electrodes were held in place with an elastic band around the chest, and not with an adhesive similar to standard electrodes. Also, our current device only allows the acquisition of two channels at a time, hence simultaneous measurement of the standard and proposed electrodes was not possible. The technical cost of the proposed design compared to a simple bootstrapped buffer of Fig. 6.6a is increased power consumption and area. The proposed circuit's area and power consumption are 30 800 µm^2

and 93 µW, while these values are 5600 µm^2 and 5 µW for the only bootstrapped buffer. Although the proposed system increased power consumption and area, it did not fall into prohibitive values, specially if the power consumption of the microcontroller and its peripherals is considered.

In Table 6.2 a comparison with other relevant work is made. Note that all the compared topologies can reach input resistances above 100 GΩ. However, with the exception of this work, the input resistance is fixed, meaning that their input node possesses a large time constant and variable low cut-off frequency. The input capacitance should have been similar to the one reported in [29]. However, due to packaging it was considerably larger. From the compared works, only [8] measured the discharge time, which was similar to the one reported for the proposed circuit. This was achieved by biasing the input with diodes and calculating only the time in saturation, neglecting the time required to settle back onto the baseline (greater than 20 s). This is a good way of quickly discharging the node, however, the input resistance becomes voltage-dependent. The proposed circuit presented larger noise compared to other works. This is mainly because of the lower electrode capacitance and lower input resistance. However, when the resistance and capacitance are taken into account, the values are close to the ones reported in [8]. Therefore, there is a clear trade-off between MA suppression and noise.

To conclude, the proposed circuit was able to keep f_l within 160 mHz of the target f_l (500 mHz) for up to 6 layers of clothing, while the standard circuit's f_l rose as more clothing was added, reaching 13 Hz. Also, the control loop drastically reduces the settling time in the input node, which allows the system to recover faster from large MA. Noise levels were low enough not to affect the control voltage V_c or make the ECG waveform unreadable. Future works will look to improve the accuracy of f_l by using digital circuits in the control loop and more advanced control techniques. Also, the noise was not optimized in this design and could be reworked for the next iteration, being that the largest contributor to noise was the current steering circuit.

	Chen [8]	Chi [29]	Spinelli [70]	Hao [93]	This work
Interface Type	Furniture or Clothing	Clothing	Polypropylene	-	Solder Mask + Clothing
Capacitance Range	220 nF to 10 pF	0.25 pF to infinity (test value)	100 pF (test value)	-	100 pF to 1pF
Implementation	0.18 um	0.5 um	Discrete	55 nm	65 nm
Input Resistance	>61.2 G* (fixed)	>50 T (fixed)	100 G* (fixed)	580 G (fixed)	3.2 to 320 G (adjustable)
Input Capacitance	0.8 pF (packaged)	60 fF (wire bonded)	<0.1 pF*	-	1 pF (packaged)
Low Cut-Off Frequency	<0.26 Hz (post-input)	<0.01 Hz (post-input)	0.016* (post-input)	0.2 Hz (post-input, tunable)	0.5 Hz (at input, tunable)
Settling Time at input	1s	-	10s (Rin x Ce)*	-	<1s
RMS Noise within 0.5-100Hz [µV]	3.7 (220 nF) or 22 (10 pF)	-	3.3 (100 pF)	2.02 (-)	17.6 (100 pF), 24.2 (10pF), 59.2 (1 pF)
Features	Capacitance Neutralization; High-pass filter after input (DSL); Input biased with diodes; Differential amplifier and DRL;	Ultra-low input capacitance buffer; Bootstrapped bias;	Capacitance neutralization; Bootstrapped Bias;	Capacitance neutralization; Bootstrapped bias with diodes; Tunable DSL;	Ultra-low input capacitance buffer; Low cut-off frequency control; External control can be used as a discharge switch; Info about electrode capacitance for DSP;

Table 6.2: Comparison table, values with * were estimated

Chapter 7

Conclusion and Future Work

In this dissertation, the input node of a capacitive electrode has been thoroughly investigated. The bibliographic review highlighted the best practices known to the date. The bootstrapping technique and the capacitance neutralization are the standard circuits for decreasing the AFE's input capacitance, either in discrete or integrated designs. The changes on the capacitance that couples the electrode to the human body, due to motion or different clothing and pressure, modify the electrode's frequency response. Thus, the low cut-off frequency is inconsistent. The bibliographic review also pointed to preliminary MA models, where they considered the problem as a time-varying capacitor and a random triboelectric voltage source. Then, this dissertation focused on providing an improved MA model based on those that already existed and finding ways to stabilize the electrode's frequency response. To achieve the latter, three distinct techniques were tried: a through-body negative feedback; using bootstrapping and neutralization to boost and control the input resistance; and an integrated control loop to set the input resistance as the electrode's capacitance varies. Next, the outcome of each proposed techniques is discussed, followed by the directions for future work.

7.1 Conclusion

The working principles of TENGs and MAs are the same, contact electrification and capacitance changes. However, TENGs have well-established models, and thus they were used as base to develop a MA model. The outcome of our work is a single equation that describes MA for motions in both longitudinal and transverse directions. It also adds a term to model MA when the electrode slides over the skin or onto an empty area (air). The results showed that, under controlled motions, the predicted and measured behaviors matched. The parameters that are usually assumed too hard to measure, such as the charge density, do

not need to be tracked as they can be scaled to match the amplitude.

Once the physics behind MA were clear, the research moved into compensating for the electrode capacitance changes. The first attempted solution revolved around a through-body negative feedback. Negative feedback is known for desensitizing gains and improving the bandwidth, thus it was a strong candidate to tackle the voltage division on the input node and the fluctuations in the bandwidth. A single-ended and a differential version were proposed, and both improved the frequency response of the cECG system in simulations. However, the transfer function showed a strong dependency on the body and insulation impedances. The practical measurements showed distorted S-waves and due to the complexity of this technique, this topic was not further explored.

Although at first glance it appears that the input biasing circuit design is a simple task, it is a rather challenging topic. The bias circuit should provide low "DC resistance" and ultra-high "AC resistance". The bootstrapped bias circuit and pseudo-resistors often achieve high resistances, however, they are limited by the opamp's input resistance or by the gate's leakage current. By getting inspiration from the capacitance neutralization, the conductance neutralization was proposed. The proposed technique boosted the input resistance by several times in both discrete and integrated designs. Further, by adding a series capacitance the effects of the electrode capacitance fluctuation is reduced, and an improved CMRR was measured. The proposed electrode also relied on the bootstrapped bias circuit, which was improved here for better linearity and smaller clipping range.

Lastly, adding a series capacitance can only partially tackle the issues that arise from the electrode capacitance change. When the electrode capacitance becomes smaller than the series capacitance, the technique is not efficient anymore. Therefore, in addition to the series capacitance an integrated AFE for capacitive electrodes was proposed. The simulations and measurements showed that the proposed IC can keep the cut-off frequency around the targeted value, with an error smaller than 0.2 Hz. This compensates for changes in the electrode capacitance due to motion or different patient's clothing, which improves the rejection of slow common-mode signals and optimizes the discharging time. One can observe that the ECG measured through the T-shirt with the proposed IC (Fig. 6.19b) has less baseline wander than the ECG measured with the conductance neutralization circuit (Fig. 5.11f).

In summary, the main contributions that this dissertations leaves to the field of capacitive electrodes are: a verified equation that model simple MAs; an electrode design with boosted input resistance, better linearity and smaller clipping range; the only reported electrode that tracks the changes of the electrode capacitance and adjust the input resistance.

7.2 Future Work

The author believes that contactless biopotential acquisition embedded into daily life objects is on the brink of its breakthrough. In the next decade, I expect the popularization of wearables that measure ECG for people in risk-groups and athletes. One example is the "HeartWatch", a bracelet being developed by Toronto-based company HelpWear. Another applications that shall gain momentum is car seats. Professional drivers (trucks, delivery, or taxis) spent countless hours siting and may not have easy access to the health system. Also, cars already have on-board computers, which makes implementing an ECG device less costly.

Capacitive electrodes plays a fundamental role in these new applications, thus their development will continue. The area that currently needs the most attention is the mechanical part because the electrode must be seamlessly integrated into objects. Therefore, flexible electronics and conductive or insulating materials are being explored. Reducing the electrode's area and power consumption will also facilitate its integration, thus specialized integrated circuits are essential.

Besides the general public acceptance, it is also necessary to convince the medical community that these new applications of the ECG can provide reliable waveform. Then, a huge challenge to be overcome is dealing with MA and unique forms of coupling. Therefore, the MA model proposed here should be further developed. The first step is to elaborate a more accurate test jig, where one could obtain three dimensional information about acceleration, displacement and contact pressure. The proposed model can also be improved by considering variable acceleration and more circuit components. These improvements should lead to a smaller error between estimated and measured MAs.

The proposed conductance neutralization render controllable ultra-high input impedances with a fast-discharge mechanism. However, it requires fine-tuning of the positive feedback gain through a potentiometer. An industry-oriented research could focus on automating this calibration or understanding the component's tolerances that lead to satisfying results. This same research could evaluate the opamp's offset threshold required so one can remove the high-pass filter and therefore eliminate the low-frequency peaks.

The proposed AFE with low cut-off frequency control showed promising results, yet, a lot more can be done. In the short term, one could evaluate the performance of our IC for different target cut-off frequencies; change packaging or wire-bond the circuit directly to the PCB to reduce the input capacitance; and assess the system's response for different test frequencies. Another option of research is exploring a better integration between the electrode and the measuring device. For example, besides the proposed control loop, the

microcontroller could detect saturation and use the external input resistance control to reset the input. Also, the part of the output containing the test signal provides information on the capacitance change, which can be correlated with triboelectric voltages. Therefore, this information could be used to digitally remove MA. For the next tapeout iteration, one could evaluate more complex control techniques to reduce settling time and enhance accuracy. A mix of analog and digital circuits is a likely path.

Appendices

Appendix A

Boosting Circuits Test

To demonstrate the improvements provided by some of the boosting circuits described in Chapter 2, this section presents the frequency response of a capacitive electrode with different boosting circuits. The guarding technique depends on the PCB design, which is shown in Fig. A.1. This PCB is the same that will be used for the circuits tested in Chapter 5. In this design, the input node was surrounded by its buffered copy on all layers. The PCB size is 34.3 mm by 34.3 mm while the sensing area is 29.7 mm by 29.7 mm.

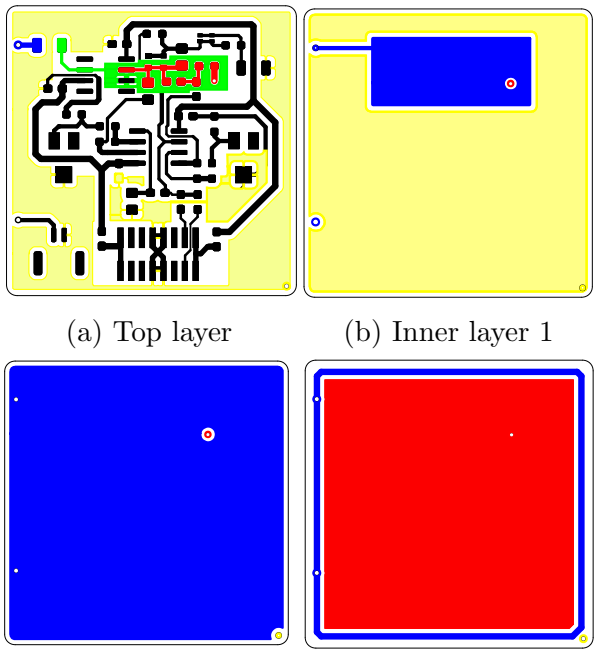

(a) Top layer (b) Inner layer 1

(c) Inner layer 2 (d) Bottom layer

Figure A.1: PCB layout layers, where inner layer 1 is below the top layer and above the inner layer 2, the bottom layer is the sensing surface. Input node in red, non-removable guard in green, removable guard in blue, ground planes in yellow

In Fig. A.1a the top layer is displayed, and the red traces contain the sensed signal, the green plane is a non-removable guard surrounding, but not in contact, with the red traces. It can be connected to the removable guard shown in blue. The inner layer 1 (Fig. A.1b) contains a large ground plane to provide noise protection and a guard plane under the input node. The inner layer 2 (Fig. A.1c) is only a guard plane protecting the sensing area in the bottom layer (Fig. A.1d) from the ground plane in the inner layer 1. A guard ring in the bottom layer also protects the sensing area.

The results in Fig. A.2 follow the theoretical explanations of the boosting circuits. "B" stands for a voltage follower with a bias resistor of 10 GΩ, "G" means the guard technique and "C" is the capacitance neutralization. In the practical measurements, C_e was controlled by adding known capacitors of 1 pF or a jumper in series with the input node. Hence, in Fig. A.2, curves labeled with 1 pF means C_e was forced to have this value, while the absence of it in the legend stands for the case where no limiting capacitor was used (jumper), and C_e is approximately 1 nF.

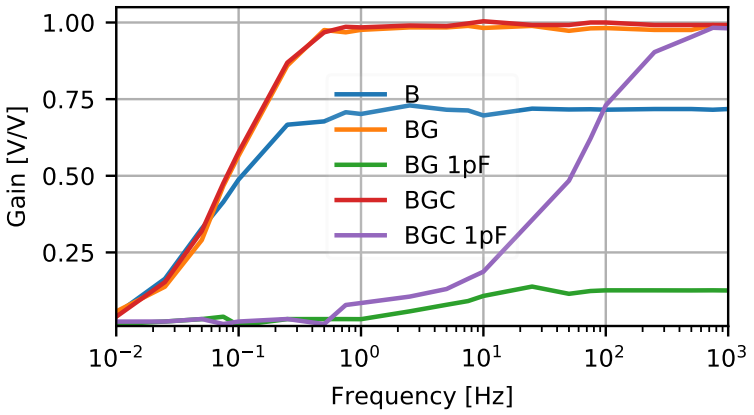

Figure A.2: Practical measurements of non-proposed techniques, where 1 pF means that a capacitor with this value was added in series with the electrode capacitance. "B" is only the buffer with R_b, "BG" has the addition of the guarding technique and "BGC" includes the capacitance neutralization circuit

The base circuit only, curve "B" in Fig. A.2, presents a gain of 0.7 V/V when no series capacitance is added. By connecting the removable guard to the non-removable guard with 0 Ω resistor (see Fig. A.1a), the gain is improved to 0.98 V/V as shown by curve "BG". This improvement comes because the guard bootstraps C_{PCB}, decreasing C_{in}, then $C_e + C_{in} \approx C_e$ and the voltage division is almost negligible. However, if a series capacitor of 1 pF is added to simulate the worst-case scenario of C_e, then the gain drops to 0.15 V/V (curve "BG 1pF").

Introducing the capacitance neutralization circuit "C", improves further the response, whereas the gain of "BGC" is larger than 0.99 V/V. Moreover, even if a series capacitance

of 1 pF is added, the gain reaches 0.98 V/V. This shows that the "C" circuit is effective in restoring the gain by diminishing C_{in}. A practical note is that if overcompensated, "C" leads to a gain greater than unity and possible oscillation.

On the other hand, Fig. A.2 demonstrates that f_c is inversely proportional to $C_{in} + C_e$, and as C_{in} is forced to be much smaller than C_e, f_c ends up being a function of C_e. Note that for no series capacitance added, the f_c of "BGC" is 150 mHz, while for "BGC 1pF" f_c is 96 Hz.

This practical measurement demonstrated that the assumption $C_{in} << C_e$, many times considered here, is true for the BGC circuit. We can see that the "B" circuit with neither "C" nor "G" circuits cannot achieve a satisfactory gain, even for the maximum electrode capacitance. The guarding technique ("G") mitigates the PCB's stray capacitances and boosts the mid-band gain to almost unity. However, this gain can only be achieved for a C_e of 1 pF if the "C" circuit is used. Hence the assumption that the C_{in} will not cause voltage division with C_e is indisputable when "C" and "G" circuits are present.

Appendix B

Implemented ECG Acquisition Board

Although the focus of this dissertation is on capacitive electrodes, the acquisition of an ECG requires analog processing circuitry such as a differential amplifier, filters, common-mode feedback, and digital signal processing. This was achieved with the design of a custom PCB comprising analog circuits. This PCB connects as a shield of a microcontroller. The data measured by the microcontroller's ADC is then sent to a laptop running a custom graphical user interface (GUI) developed in Python.

Figure B.1 shows the implemented ECG acquisition system. The white PCB is the microcontroller, and on the top of it, there is the PCB containing the analog processing circuits (labeled as "Diff+DRL"). The electrodes are connected to the "Diff+DRL" board through connectors. Note that between these connectors, a wire outputs the common-mode feedback signal (DRL). Another wire gives access to the system's ground, needed for testing with other laboratory instruments such as oscilloscopes. A USB cable connects the device to a PC, establishing power supply and communication.

An example of an ECG acquisition is depicted in Fig. B.2. The GUI can be seen on the laptop's screen, where the filtered and raw ECG are displayed. To reduce power line interferences/noise the laptop is not plugged into an electrical outlet, therefore, it is powered by the battery. In the picture, the electrodes are in direct contact with the skin, on the chest region. They are held in place by an elastic band over the T-shirt. The DRL is implemented by attaching its output on the PCB through an alligator cable to an aluminum sheet, which the subject is sitting over. Next, the analog processing circuit, microcontroller setup, and GUI are described in detail.

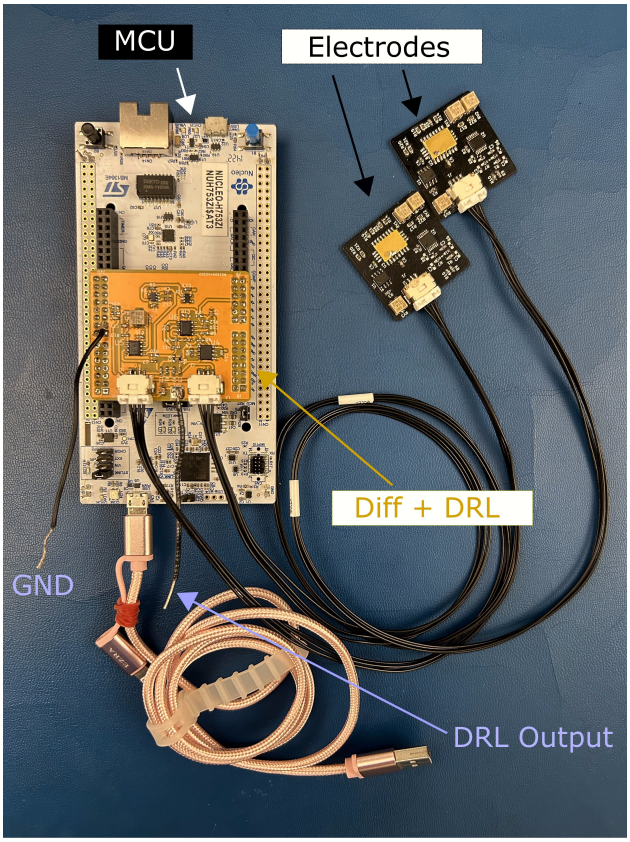

Figure B.1: Microcontroller, analog processing PCB and electrodes

B.1 Analog Circuitry

Figure B.3 shows the full schematic of the analog circuit without the electrodes. The top branch leading to $V_{o,ADC}$ is the differential path, while the bottom branch processing V_{cm} into $V_{o,DRL}$ is the common-mode path. The reference voltage of 1.25 V was obtained from the IC MAX6070BAUT12+T and the supply voltage is regulated to 2.5 V from the microcontroller's 3.3 V.

B.1.1 Input

The design considers that electrodes connected to the two inputs (IN+ and IN-) may be biased with different offsets. Moreover, passive electrodes present very low DC voltages. Therefore, to accommodate both active and passive electrodes, the input stage consists of high-pass filters that set the signal's offset to 1.25 V.

The resistors R_{cm1} and R_{cm2} extract the common-mode voltage between the inputs (V_{cm}). Their resistance, 10 kΩ (±1%), was chosen to be much higher than the source's impedance, which is the electrode's low output resistance in series with the cable's resistance. However,

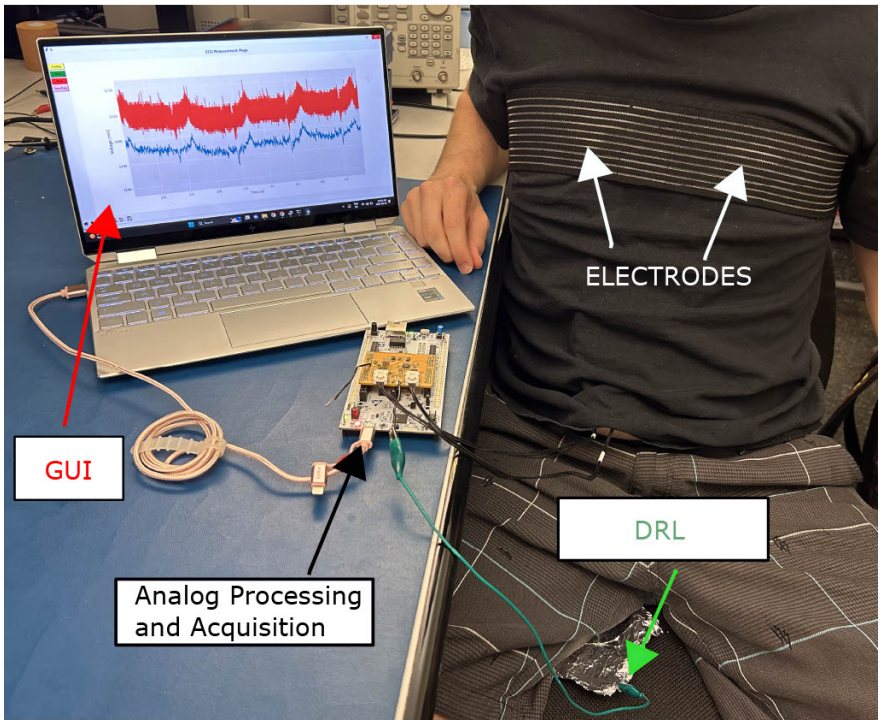

Figure B.2: A portable capacitive ECG system

R_{cm1} and R_{cm2} should be low enough to not interfere with the subsequent high-pass filter (C_7 and R_9) and the biasing at 1.25 V. Besides setting V_{cm}'s offset the filter removes low-frequency artifacts such as MA below 0.16 Hz. Note that setting the DC offset is mandatory for the common-mode branch to avoid DC gain in the next stage.

On the differential branch, the high-pass filter is mandatory only for passive electrodes (to bias the amplifier's input) or electrodes with unmatched DC offset and high gain amplifiers (avoiding DC saturation). Nevertheless, the implemented board comprises the filters C_1R_1 and C_2R_2. The cut-off frequency is 5 mHz, which provides enough bandwidth even for ECG applications that require cut-off frequencies as low as 50 mHz. Although the focus is on ECG with a cut-off frequency at 500 mHz, this circuit's cut-off frequency is very low so that the electrode's cut-off frequency is the dominant one. The drawback of these filters is the initial slow settling time.

B.1.2 Differential Branch

The first stage of the differential branch is an instrumentation amplifier, the AD8226. It is supplied with 2.5 V and ground, the resistor R_G sets the gain to approximately 10 ($1+49.4\text{k}/R_G$). The input resistance is 400 MΩ and the input capacitance is 2 pF, introducing negligible error to the precedent high-pass filter. The amplifier's common-mode rejection

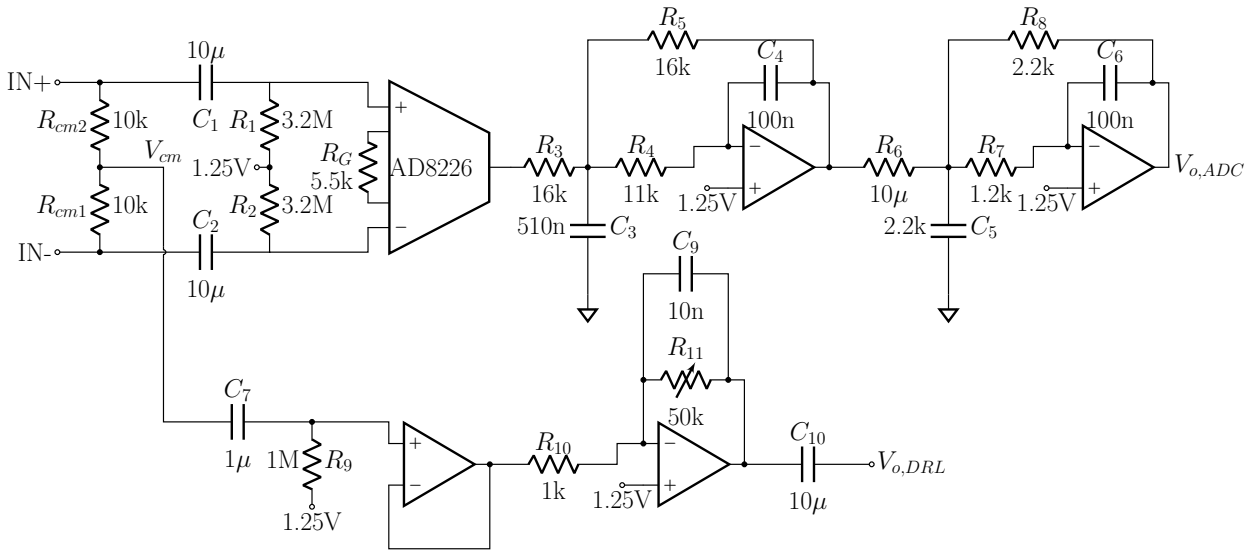

Figure B.3: Implemented differential circuit

ratio in the bandwidth of interest is greater than 106 dB.

The second stage consists of a 4$^{\text{th}}$ order low-pass filter with a cut-off frequency of 100 Hz. Normally, this filter could consist of a simple RC passive filter, however, one of the circuits proposed in this dissertation contains a large test signal at 1 kHz, thus, the high attenuation filter was used for the purpose of eliminating it, leaving just the ECG waveform.

B.1.3 Driven Right Leg

The common-mode branch is also known as the right-leg drive. After the R_9C_7 high-pass filter, a buffer isolates the filter from the succeeding inverting amplifier. The driven right-leg principle of operation relies on creating negative feedback with the common-mode signals, which from the body's perspective is a lower impedance path to ground that reduces the 60 Hz interference. Hence, to establish the negative feedback, an inverting amplifier is used, whereas its gain is given by R_{11}/R_{10}. To optimize the DRL's performance, R_{11} is a potentiometer of 50 kΩ and C_9 aids with phase margin. The value of R_{11} was increased until the common-mode feedback reached the edge of oscillation.

Figure B.4a shows cECG waveforms acquired with and without the DRL circuit. The acquisition with DRL outputs a waveform where the ECG characteristics can be easily spotted. On the other hand, the measurement without DRL is mostly dominated by 60 Hz noise, and only the largest peaks on the ECG can be spotted. Figure B.4b computes the FFT from the two cECGs shown in Figure B.4a. The plot is centered around 60 Hz and by computing the ratio between the highest components, the attenuation factor imposed by the

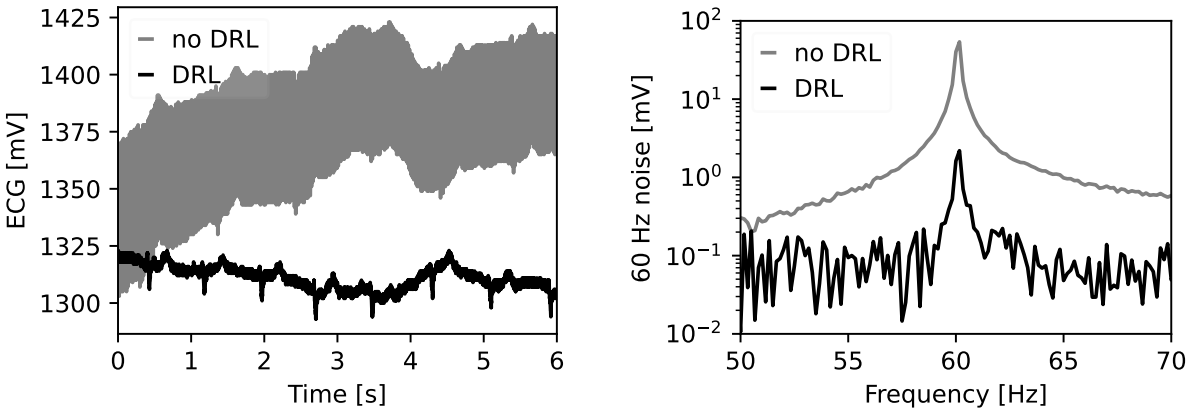

(a) cECG with and without DRL

(b) FFT around 60 Hz of a cECG with and without DRL

Figure B.4: Demonstration of the DRL circuit suppressing the 60 Hz interference. The signal was measured at $V_{o,ADC}$

DRL is estimated to be 25.

B.2 Microcontroller

Two microcontrollers were tested, the STM32F303ZE and the STM32H753ZI, both within the NUCLEO-144 development board, which allowed using the same I/O pins for both devices. The two microcontrollers are capable of providing ECG waveforms with the same sampling rate of 3.2 kSa/s. However, the STM32F3 series ADC has a resolution of 12 bits while the STM32H7 ADC resolution is 16 bits. The clock frequency of the STM32H7 is much higher than the one of the STM32F3, 240 MHz against 72 MHz.

The microcontroller programming used the hardware abstraction layer (HAL) drivers, which allows an easy configuration of the peripheral's registers. The microcontroller's ADC was triggered by the timer's output every 31.25 ms. Once a conversion is completed, an interruption is generated and the software transfers the measured data to a PC via UART communication with a baud rate of 230400 bits/s.

A second timer toggles a digital I/O pin every 1 ms, generating a square wave with amplitude ranging from ground to 3.3 V and a frequency of 1 kHz. This signal goes to the PCB containing the analog circuits, where it passes through a low-pass filter at 1.28 kHz and voltage divider, shown in Fig. B.5a. This is necessary to attenuate the 3.3 V amplitude down to 2.5 V and reduce the spikes created edges of the square wave. This signal is required for one of the proposed electrodes.

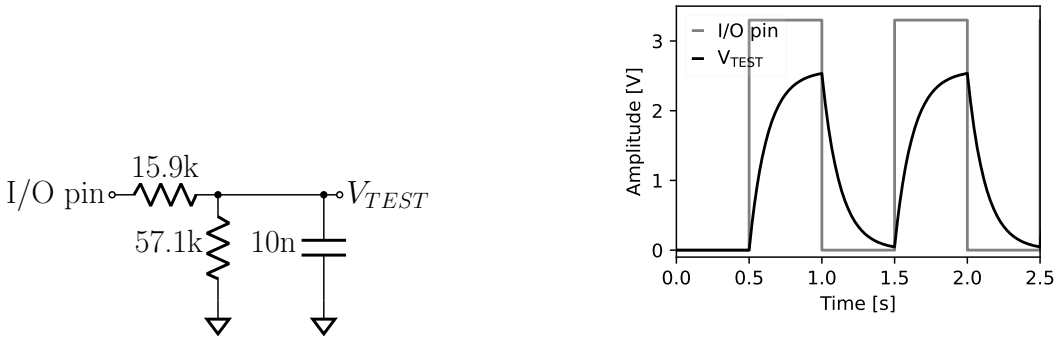

(a) Low-pass filter and voltage divider to generate the test signal

(b) Simulated I/O pin output and resulting V_{TEST}

Figure B.5: Circuit to generate V_{TEST} from the I/O pin and the resulting waveform

B.3 GUI

The custom GUI was developed in Python, based on the Tkinter library. Other libraries used were matplotlib, numpy, scipy, and pySerial. The GUI consists of two pages, the initial page allows the user to set the ADC resolution (12 or 16 bits) and choose the COM port to which the device is connected. The second page, called the "measurement page", comprises buttons to return to the initial page, start or stop a measurement, and save data. The measurement page is shown in Fig. B.6.

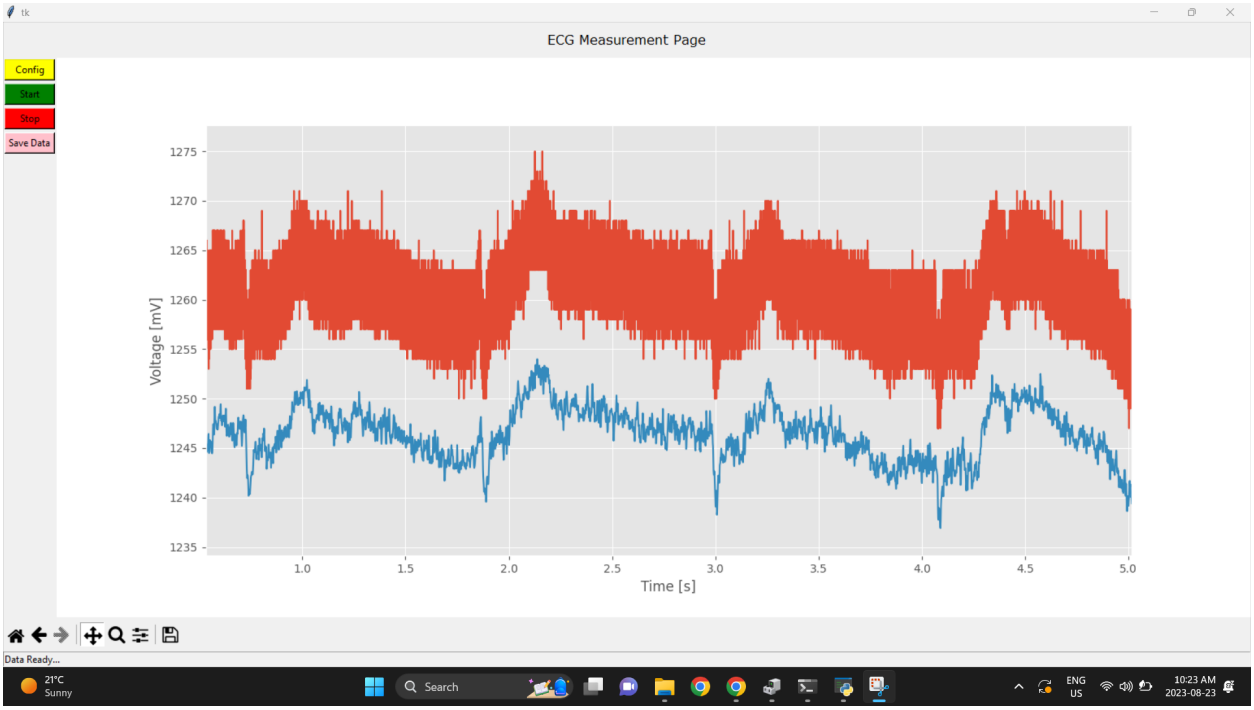

Figure B.6: The custom graphical user interface for ECG acquisition

During measurement, the GUI uses threads to perform tasks simultaneously. That is, the acquire function receives data through the USB port and stores it in the sample buffer. Once this buffer is filled, the plot function is called in parallel, which copies the data in the sample buffer to the plot buffer. Hence new data can be received while the old data is still being plotted. In each plot, 6 s of ECG is acquired, while the first 0.5 s is not displayed to remove the settling time from the digital filters. To save the data being visualized, one must stop the measurement and press the save data button. Only the raw data is saved to the .txt file to optimize speed.

Bibliography

[1] World Health Organization (WHO), *Cardiovascular diseases (CVDs)*, 2021. [Online]. Available: https://www.who.int/news-room/fact-sheets/detail/cardiovascular-diseases-(cvds).

[2] C. W. Tsao, A. W. Aday, Z. I. Almarzooq, *et al.*, "Heart disease and stroke statistics—2023 update: A report from the american heart association," *Circulation*, vol. 147, no. 8, e93–e621, 2023.

[3] S. L. Ivey, H. R. Hanley, C. Taylor, *et al.*, "Early identification and treatment of women's cardiovascular risk factors prevents cardiovascular disease, saves lives, and protects future generations: Policy recommendations and take action plan utilizing policy levers," *Clinical Cardiology*, vol. 45, no. 11, pp. 1100–1106, 2022.

[4] S. Mishra, G. Khatwani, R. Patil, *et al.*, "Ecg paper record digitization and diagnosis using deep learning," *Journal of medical and biological engineering*, vol. 41, no. 4, pp. 422–432, 2021.

[5] C. Roopa and B. Harish, "A survey on various machine learning approaches for ecg analysis," *International Journal of Computer Applications*, vol. 163, no. 9, pp. 25–33, 2017.

[6] J. Francis, "Ecg monitoring leads and special leads," *Indian pacing and electrophysiology journal*, vol. 16, no. 3, pp. 92–95, 2016.

[7] A. Davies and A. Scott, *Starting to Read ECGs*. Springer, 2014.

[8] M. Chen, H. S. Chun, I. D. Castro, *et al.*, "A 400 GΩ Input-Impedance Active Electrode for Non-Contact Capacitively Coupled ECG Acquisition with Large Linear-Input-Range and High CM-Interference-Tolerance," *IEEE Transactions on Biomedical Circuits and Systems*, vol. 13, no. 2, pp. 376–386, Apr. 2019, ISSN: 19324545. DOI: 10.1109/TBCAS.2019.2895660. [Online]. Available: https://ieeexplore.ieee.org/document/8627965/.

[9] J. J. Bailey, A. S. Berson, A. Garson Jr, *et al.*, "Recommendations for standardization and specifications in automated electrocardiography: Bandwidth and digital signal processing. a report for health professionals by an ad hoc writing group of the committee on electrocardiography and cardiac electrophysiology of the council on clinical cardiology, american heart association.," *Circulation*, vol. 81, no. 2, pp. 730–739, 1990.

[10] L. Xu, C. Rabotti, Y. Zhang, *et al.*, "Adaptive motion-artifact reduction in capacitive ECG measurements by using the power-line interference," in *MeMeA 2018 - 2018 IEEE International Symposium on Medical Measurements and Applications, Proceedings*, IEEE, Jun. 2018, pp. 1–5, ISBN: 9781538633915. DOI: 10.1109/MeMeA.2018.8438751. [Online]. Available: https://ieeexplore.ieee.org/document/8438751/.

[11] G. D. Clifford, F. Azuaje, and P. McSharry, *Advanced methods and tools for ECG data analysis*, English, Boston, 2006. [Online]. Available: http://www.books24x7.com/marc.asp?bookid=27221.

[12] X. Li, H. Hui, and Y. Sun, "Investigation of motion artifacts for biopotential measurement in wearable devices," *BSN 2016 - 13th Annual Body Sensor Networks Conference*, pp. 218–223, 2016. DOI: 10.1109/BSN.2016.7516263.

[13] Y. Sun and X. B. Yu, "Capacitive Biopotential Measurement for Electrophysiological Signal Acquisition: A Review," *IEEE Sensors Journal*, vol. 16, no. 9, pp. 2832–2853, 2016, ISSN: 1530437X. DOI: 10.1109/JSEN.2016.2519392.

[14] A. Aleksandrowicz and S. Leonhardt, "Wireless and Non-contact ECG Measurement System – the "Aachen SmartChair"," *Acta Polytechnica*, vol. 47, no. 4-5, pp. 5–8, 2007, ISSN: 1210-2709. DOI: 10.14311/974.

[15] K. Ko, K. Yong, and S. Kwang, "Common mode noise cancellation for electrically non-contact ECG measurement system on a chair," in *Annual International Conference of the IEEE Engineering in Medicine and Biology - Proceedings*, vol. 7 VOLS, 2005, pp. 5881–5883, ISBN: 9780780387409.

[16] K.-F. Wu and Y.-T. Zhang, "Contactless and continuous monitoring of heart electric activities through clothes on a sleeping bed," in *5th Int. Conference on Information Technology and Applications in Biomedicine, ITAB 2008 in conjunction with 2nd Int. Symposium and Summer School on Biomedical and Health Engineering, IS3BHE 2008*, 2008, pp. 282–285, ISBN: 9781424422555. DOI: 10.1109/ITAB.2008.4570586.

[17] J. Weeks, M. Elsaadany, M. Lessard-Tremblay, L. Targino, M. Liamini, and G. Gagnon, "A Novel Sensor-Array System for Contactless Electrocardiogram Acquisition," in *2020 42nd Annual International Conference of the IEEE Engineering in Medicine & Biology Society (EMBC)*, vol. 2020-July, IEEE, Jul. 2020, pp. 4122–4125, ISBN: 978-1-7281-1990-8. DOI: 10.1109/EMBC44109.2020.9175666. [Online]. Available: https://ieeexplore.ieee.org/document/9175666/.

[18] T. Wartzek, B. Eilebrecht, J. Lem, H.-J. J. Lindner, S. Leonhardt, and M. Walter, "ECG on the Road: Robust and Unobtrusive Estimation of Heart Rate," *IEEE Transactions on Biomedical Engineering*, vol. 58, no. 11, pp. 3112–3120, Nov. 2011, ISSN: 0018-9294. DOI: 10.1109/TBME.2011.2163715. [Online]. Available: http://ieeexplore.ieee.org/document/5976431/.

[19] D. Uguz, R. Dettori, A. Napp, *et al.*, "Car Seats with Capacitive ECG Electrodes Can Detect Cardiac Pacemaker Spikes," *Sensors*, vol. 20, no. 21, p. 6288, Nov. 2020, ISSN: 1424-8220. DOI: 10.3390/s20216288. [Online]. Available: https://www.mdpi.com/1424-8220/20/21/6288.

[20] Y. M. Chi, T.-P. Jung, and G. Cauwenberghs, "Dry-Contact and Noncontact Biopotential Electrodes: Methodological Review," *IEEE Reviews in Biomedical Engineering*, vol. 3, pp. 106–119, 2010, ISSN: 1937-3333. DOI: 10.1109/RBME.2010.2084078. [Online]. Available: http://ieeexplore.ieee.org/document/5598518/.

[21] T. Wartzek, C. Bruser, T. Schlebusch, *et al.*, "Modeling of motion artifacts in contactless heart rate measurements," *Computing in Cardiology*, vol. 40, no. 1, pp. 931–934, 2013, ISSN: 23258861.

[22] J. Xu, B. Busze, C. Van Hoof, K. A. A. Makinwa, and R. F. Yazicioglu, "A 15-Channel Digital Active Electrode System for Multi-Parameter Biopotential Measurement," *IEEE Journal of Solid-State Circuits*, vol. 50, no. 9, pp. 2090–2100, Sep. 2015, ISSN: 0018-9200. DOI: 10.1109/JSSC.2015.2422798. [Online]. Available: http://ieeexplore.ieee.org/document/7100949/.

[23] X. An, Y. Liu, Y. Zhao, S. Lu, G. K. Stylios, and Q. Liu, "Adaptive motion artifact reduction in wearable ecg measurements using impedance pneumography signal," *Sensors*, vol. 22, no. 15, p. 5493, 2022.

[24] D. U. Uguz, P. Weidener, C. D. Bezek, T. Wang, S. Leonhardt, and C. H. Antink, "Ballistocardiographic Coupling of Triboelectric Charges into Capacitive ECG," in *2019 IEEE International Symposium on Medical Measurements and Applications (MeMeA)*,

IEEE, Jun. 2019, pp. 1–5, ISBN: 978-1-5386-8428-3. DOI: 10.1109/MeMeA.2019.8802227. [Online]. Available: https://ieeexplore.ieee.org/document/8802227/.

[25] T. Wartzek, T. Lammersen, B. Eilebrecht, M. Walter, and S. Leonhardt, "Triboelectricity in capacitive biopotential measurements," *IEEE Transactions on Biomedical Engineering*, vol. 58, no. 5, pp. 1268–1277, May 2011, ISSN: 00189294. DOI: 10.1109/TBME.2010.2100393. [Online]. Available: http://ieeexplore.ieee.org/document/5672585/.

[26] L. Leicht, B. Eilebrecht, S. Weyer, S. Leonhardt, and D. Teichmann, "Closed-loop control of humidification for artifact reduction in capacitive ecg measurements," *IEEE transactions on biomedical circuits and systems*, vol. 11, no. 2, pp. 300–313, 2017.

[27] S. Niu and Z. L. Wang, "Theoretical systems of triboelectric nanogenerators," *Nano Energy*, vol. 14, pp. 161–192, 2014, ISSN: 22112855. DOI: 10.1016/j.nanoen.2014.11.034. [Online]. Available: http://dx.doi.org/10.1016/j.nanoen.2014.11.034.

[28] V. Sirtoli, M. Liamini, L. T. Lins, *et al.*, "Removal of motion artifacts in capacitive electrocardiogram acquisition: A review," *IEEE Transactions on Biomedical Circuits and Systems*, 2023.

[29] Y. M. Chi, C. Maier, and G. Cauwenberghs, "Ultra-high input impedance, low noise integrated amplifier for noncontact biopotential sensing," *IEEE Journal on Emerging and Selected Topics in Circuits and Systems*, vol. 1, no. 4, pp. 526–535, 2011, ISSN: 21563357. DOI: 10.1109/JETCAS.2011.2179419.

[30] M. Yoshiwaki, A. Murai, Y. Sakaue, and M. Makikawa, "A new approach to estimate ECG signal source using voltage divider technology," *Proceedings of the SICE Annual Conference*, pp. 1460–1465, 2014. DOI: 10.1109/SICE.2014.6935278.

[31] Y. Sakaue and M. Makikawa, "Signal source estimation inside the human heart during ventricular activation using switching voltage divider," *Proceedings of the Annual International Conference of the IEEE Engineering in Medicine and Biology Society, EMBS*, vol. 2016-Octob, pp. 3879–3882, 2016, ISSN: 1557170X. DOI: 10.1109/EMBC.2016.7591575.

[32] a. Baba and M. J. Burke, "Measurement of the electrical properties of ungelled ECG electrodes," *International Journal of Biology and Biomedical Engineering*, vol. 2, no. 1, pp. 89–97, 2008. [Online]. Available: http://www.naun.org/journals/bio/bio-17.pdf.

[33] C. J. Harland, T. D. Clark, and R. J. Prance, "Electric potential probes - new directions in the remote sensing of the human body," *Measurement Science and Technology*, vol. 13, no. 2, pp. 163–169, Feb. 2002, ISSN: 0957-0233. DOI: 10.1088/0957-0233/13/2/304. [Online]. Available: http://stacks.iop.org/0957-0233/13/i=2/a=304?key=crossref.2ee885bfa6ef48333405373ee4f44c0f.

[34] T. Komensky, M. Jurcisin, K. Ruman, O. Kovac, D. Laqua, and P. Husar, "Ultra-wearable capacitive coupled and common electrode-free ECG monitoring system," in *2012 Annual International Conference of the IEEE Engineering in Medicine and Biology Society*, IEEE, Aug. 2012, pp. 1594–1597, ISBN: 978-1-4577-1787-1. DOI: 10.1109/EMBC.2012.6346249. [Online]. Available: http://ieeexplore.ieee.org/document/6346249/.

[35] A. Serteyn, R. Vullings, M. Meftah, and J. W. M. Bergmans, "Motion artifacts in capacitive ecg measurements: Reducing the combined effect of DC voltages and capacitance changes using an injection signal," *IEEE Transactions on Biomedical Engineering*, vol. 62, no. 1, pp. 264–273, Jan. 2015, ISSN: 0018-9294. DOI: 10.1109/TBME.2014.2348178. [Online]. Available: http://ieeexplore.ieee.org/document/6879256/.

[36] B. Chamadiya, S. Heuer, U. G. Hofmann, and M. Wagner, "Towards a capacitively coupled electrocardiography system for car seat integration," in *IFMBE Proceedings*, vol. 22, 2009, pp. 1217–1221, ISBN: 9783540892076. DOI: 10.1007/978-3-540-89208-3_291. [Online]. Available: http://link.springer.com/10.1007/978-3-540-89208-3%7B%5C_%7D291.

[37] E. Nemati, M. J. Deen, and T. Mondal, "A wireless wearable ECG sensor for long-term applications," *IEEE Communications Magazine*, vol. 50, no. 1, pp. 36–43, Jan. 2012, ISSN: 0163-6804. DOI: 10.1109/MCOM.2012.6122530. [Online]. Available: http://ieeexplore.ieee.org/document/6122530/.

[38] S. Leonhardt and A. Aleksandrowicz, "Non-contact ECG monitoring for automotive application," in *2008 5th International Summer School and Symposium on Medical Devices and Biosensors*, IEEE, 2008, pp. 183–185, ISBN: 978-1-4244-2252-4. DOI: 10.1109/ISSMDBS.2008.4575048. [Online]. Available: http://ieeexplore.ieee.org/document/4575048/.

[39] Y. M. Chi, S. R. Deiss, and G. Cauwenberghs, "Non-contact Low Power EEG/ECG Electrode for High Density Wearable Biopotential Sensor Networks," in *2009 Sixth International Workshop on Wearable and Implantable Body Sensor Networks*, IEEE, Jun. 2009, pp. 246–250, ISBN: 978-0-7695-3644-6. DOI: 10.1109/BSN.2009.52. [Online]. Available: http://ieeexplore.ieee.org/document/5226885/.

[40] V. P. Rachim and W.-Y. Chung, "Wearable Noncontact Armband for Mobile ECG Monitoring System," *IEEE Transactions on Biomedical Circuits and Systems*, vol. 10, no. 6, pp. 1112–1118, Dec. 2016, ISSN: 1932-4545. DOI: 10.1109/TBCAS.2016.2519523. [Online]. Available: https://ieeexplore.ieee.org/document/7471436/.

[41] I. D. Castro, R. Morariu, T. Torfs, C. Van Hoof, and R. Puers, "Robust wireless capacitive ECG system with adaptive signal quality and motion artifact reduction," *2016 IEEE International Symposium on Medical Measurements and Applications, MeMeA 2016 - Proceedings*, pp. 1–3, May 2016. DOI: 10.1109/MeMeA.2016.7533802. [Online]. Available: http://ieeexplore.ieee.org/document/7533802/.

[42] J. Wannenburg, R. Malekian, and G. P. Hancke, "Wireless Capacitive-Based ECG Sensing for Feature Extraction and Mobile Health Monitoring," *IEEE Sensors Journal*, vol. 18, no. 14, pp. 6023–6032, Jul. 2018, ISSN: 1530-437X. DOI: 10.1109/JSEN.2018.2844122. [Online]. Available: https://ieeexplore.ieee.org/document/8371587/.

[43] J. H. Kim, S. M. Lee, and S.-H. Lee, "Capacitive monitoring of bio and neuro signals," *Biomedical Engineering Letters*, vol. 4, pp. 142–148, 2014.

[44] A. Ueno, Y. Akabane, T. Kato, H. Hoshino, S. Kataoka, and Y. Ishiyama, "Capacitive sensing of electrocardiographic potential through cloth from the dorsal surface of the body in a supine position: A preliminary study," *IEEE Transactions on Biomedical Engineering*, vol. 54, no. 4, pp. 759–766, Apr. 2007, ISSN: 00189294. DOI: 10.1109/TBME.2006.889201. [Online]. Available: http://ieeexplore.ieee.org/document/4132946/.

[45] Z. Xiao, Y. Xing, Y. Li, C. Yang, J. Li, and C. Liu, "Effect of cotton fabric moisture regain and thickness on signal quality of noncontact capacitive coupling ecg," *IEEE Transactions on Instrumentation and Measurement*, vol. 71, pp. 1–12, 2022.

[46] M. Lessard-Tremblay, J. Weeks, L. Morelli, G. Cowan, G. Gagnon, and R. J. Zednik, "Contactless Capacitive Electrocardiography Using Hybrid Flexible Printed Electrodes," *Sensors*, vol. 20, no. 18, p. 5156, Sep. 2020, ISSN: 1424-8220. DOI: 10.3390/s20185156. [Online]. Available: https://www.mdpi.com/1424-8220/20/18/5156.

[47] L. Morelli, G. Gagnon, and R. J. Zednik, "Flexible capacitive kirigami electrode: Experimental investigation and analytical model," *IEEE Journal on Flexible Electronics*, 2023.

[48] T. Torfs, Y.-H. Chen, H. Kim, and R. F. Yazicioglu, "Noncontact ECG Recording System With Real Time Capacitance Measurement for Motion Artifact Reduction," *IEEE Transactions on Biomedical Circuits and Systems*, vol. 8, no. 5, pp. 617–625, Oct. 2014, ISSN: 1932-4545. DOI: 10.1109/TBCAS.2014.2359053. [Online]. Available: http://ieeexplore.ieee.org/document/6920090/.

[49] D. M. Gooding and G. K. Kaufman, "Tribocharging and the Triboelectric Series," in *Encyclopedia of Inorganic and Bioinorganic Chemistry*, Chichester, UK: John Wiley & Sons, Ltd, Mar. 2014, pp. 1–9. DOI: 10.1002/9781119951438.eibc2239. [Online]. Available: http://doi.wiley.com/10.1002/9781119951438.eibc2239.

[50] A. Ghaffarinejad and J. Yavand Hasani, "Modeling of triboelectric charge accumulation dynamics at the metal–insulator interface for variable capacitive structures: application to triboelectric nanogenerators," *Applied Physics A: Materials Science and Processing*, vol. 125, no. 4, pp. 1–14, 2019, ISSN: 14320630. DOI: 10.1007/s00339-019-2495-y. [Online]. Available: http://dx.doi.org/10.1007/s00339-019-2495-y.

[51] H. Zou, Y. Zhang, L. Guo, *et al.*, "Quantifying the triboelectric series," *Nature Communications*, vol. 10, no. 1, p. 1427, Dec. 2019, ISSN: 2041-1723. DOI: 10.1038/s41467-019-09461-x. [Online]. Available: http://www.nature.com/articles/s41467-019-09461-x.

[52] B. W. Lee and D. E. Orr, *The TriboElectric Series*. [Online]. Available: https://www.alphalabinc.com/triboelectric-series/ (visited on 02/10/2021).

[53] M. Safronov, A. Kuzmin, O. Bodin, V. Baranov, A. Trofimov, and A. Tychkov, "Mobile ECG monitoring device with bioimpedance measurement and analysis," *Conference of Open Innovation Association, FRUCT*, vol. 2019-April, pp. 375–380, 2019, ISSN: 23057254. DOI: 10.23919/FRUCT.2019.8711944.

[54] K. V. T. Piipponen, R. Sepponen, and P. Eskelinen, "A biosignal instrumentation system using capacitive coupling for power and signal isolation," *IEEE Transactions on Biomedical Engineering*, vol. 54, no. 10, pp. 1822–1828, 2007, ISSN: 00189294. DOI: 10.1109/TBME.2007.894830.

[55] V. Acharya, "Improving Common-Mode Rejection Using the Right-Leg Drive Amplifier," *Ti*, no. July, pp. 1–11, 2011. [Online]. Available: http://www.tij.co.jp/jp/lit/an/sbaa188/sbaa188.pdf.

[56] F. N. Guerrero and E. Spinelli, "High gain driven right leg circuit for dry electrode systems," *Medical Engineering and Physics*, vol. 39, pp. 117–122, 2017, ISSN: 18734030. DOI: 10.1016/j.medengphy.2016.11.005. [Online]. Available: http://dx.doi.org/10.1016/j.medengphy.2016.11.005.

[57] J. Gomez-Clapers, E. Serrano-Finetti, R. Casanella, and R. Pallas-Areny, "Can driven-right-leg circuits increase interference in ECG amplifiers?" In *2011 Annual International Conference of the IEEE Engineering in Medicine and Biology Society*, IEEE, Aug. 2011, pp. 4780–4783, ISBN: 978-1-4577-1589-1. DOI: 10.1109/IEMBS.2011.6091184. [Online]. Available: http://ieeexplore.ieee.org/document/6091184/.

[58] C. Hoog Antink, F. Schulz, S. Leonhardt, and M. Walter, "Motion Artifact Quantification and Sensor Fusion for Unobtrusive Health Monitoring," *Sensors*, vol. 18, no. 2, p. 38, Dec. 2017, ISSN: 1424-8220. DOI: 10.3390/s18010038. [Online]. Available: http://www.mdpi.com/1424-8220/18/1/38.

[59] J. Ottenbacher and S. Heuer, "Motion Artefacts in Capacitively Coupled ECG Electrodes," *IFMBE Proceedings*, vol. 25, no. 4, pp. 1059–1062, 2009, ISSN: 16800737. DOI: 10.1007/978-3-642-03882-2-282. [Online]. Available: http://link.springer.com/10.1007/978-3-642-03882-2%7B%5C_%7D282.

[60] A. Karmakar, D. M. Das, and M. S. Baghini, "Adaptive analogue calibration technique to compensate electrode motion artefacts in biopotential recording," *IET Circuits, Devices and Systems*, vol. 14, no. 3, pp. 327–332, 2020, ISSN: 1751858X. DOI: 10.1049/iet-cds.2019.0409.

[61] J. Xu, S. Mitra, C. Van Hoof, R. F. Yazicioglu, and K. A. Makinwa, "Active Electrodes for Wearable EEG Acquisition: Review and Electronics Design Methodology," *IEEE Reviews in Biomedical Engineering*, vol. 10, pp. 187–198, 2017, ISSN: 19411189. DOI: 10.1109/RBME.2017.2656388.

[62] E. Spinelli and M. Haberman, "Insulating electrodes: A review on biopotential front ends for dielectric skin-electrode interfaces," *Physiological Measurement*, vol. 31, no. 10, 2010, ISSN: 09673334. DOI: 10.1088/0967-3334/31/10/S03.

[63] A. Devices, *Mt-047: Op amp noise, 2009*.

[64] R. J. Prance, A. Debray, T. D. Clark, *et al.*, "An ultra-low-noise electrical-potential probe for human-body scanning," *Measurement Science and Technology*, vol. 11, no. 3, pp. 291–297, Mar. 2000, ISSN: 0957-0233. DOI: 10.1088/0957-0233/11/3/318. [Online]. Available: https://iopscience.iop.org/article/10.1088/0957-0233/11/3/318.

[65] Y. Chi and G. Cauwenberghs, "Micropower non-contact EEG electrode with active common-mode noise suppression and input capacitance cancellation," in *2009 Annual International Conference of the IEEE Engineering in Medicine and Biology Society*, IEEE, Sep. 2009, pp. 4218–4221, ISBN: 9781424432967. DOI: 10.1109/IEMBS.2009.5333527. [Online]. Available: http://ieeexplore.ieee.org/document/5333527/.

[66] F. N. Guerrero and E. M. Spinelli, "A two-wired ultra-high input impedance active electrode," *IEEE Transactions on Biomedical Circuits and Systems*, vol. 12, no. 2, pp. 437–445, 2018, ISSN: 19324545. DOI: 10.1109/TBCAS.2018.2796581.

[67] H. Nakamura and A. Ueno, "Bootstrapped Non-Inverting Front-End Amplifier for Capacitive Electrocardiogram Measurement *," *2018 IEEE Biomedical Circuits and Systems Conference, BioCAS 2018 - Proceedings*, pp. 2018–2021, 2018. DOI: 10.1109/BIOCAS.2018.8584676.

[68] R. J. Prance, T. D. Clark, H. Prance, and A. Clippingdale, "Non-contact VLSI imaging using a scanning electric potential microscope," *Measurement Science and Technology*, vol. 9, no. 8, pp. 1229–1235, 1998, ISSN: 09570233. DOI: 10.1088/0957-0233/9/8/014.

[69] H. Nakamura, Y. Sakajiri, H. Ishigami, and A. Ueno, "A novel analog front end with voltage-dependent input impedance and bandpass amplification for capacitive biopotential measurements," *Sensors (Switzerland)*, vol. 20, no. 9, 2020, ISSN: 14248220. DOI: 10.3390/s20092476.

[70] E. Spinelli, F. Guerrero, P. García, and M. Haberman, "A simple and reproducible capacitive electrode," *Medical Engineering and Physics*, vol. 38, no. 3, pp. 286–289, 2016, ISSN: 18734030. DOI: 10.1016/j.medengphy.2015.12.006.

[71] T. W. Wang and S. F. Lin, "Negative Impedance Capacitive Electrode for ECG Sensing through Fabric Layer," *IEEE Transactions on Instrumentation and Measurement*, vol. 70, 2021, ISSN: 15579662. DOI: 10.1109/TIM.2020.3045187.

[72] T. J. Sullivan, S. R. Deiss, and G. Cauwenberghs, "A low-noise, non-contact EEG/ECG sensor," *Conference Proceedings - IEEE Biomedical Circuits and Systems Conference Healthcare Technology, BiOCAS2007*, pp. 154–157, Nov. 2007. DOI: 10.1109/BIOCAS.2007.4463332. [Online]. Available: http://ieeexplore.ieee.org/document/4463332/.

[73] N. Van Helleputte, M. Konijnenburg, J. Pettine, *et al.*, "A 345 uW Multi-Sensor Biomedical SoC With Bio-Impedance, 3-Channel ECG, Motion Artifact Reduction, and Integrated DSP," *IEEE Journal of Solid-State Circuits*, vol. 50, no. 1, pp. 230–

244, Jan. 2015, ISSN: 0018-9200. DOI: 10.1109/JSSC.2014.2359962. [Online]. Available: http://ieeexplore.ieee.org/document/6923499/.

[74] E. Spinelli, M. Haberman, P. García, and F. Guerrero, "A capacitive electrode with fast recovery feature," *Physiological Measurement*, vol. 33, no. 8, pp. 1277–1288, 2012, ISSN: 13616579. DOI: 10.1088/0967-3334/33/8/1277.

[75] X. Li and Y. Sun, "A wearable button-like system for long-term multiple biopotential monitoring using non-contact electrodes," *Smart Health*, vol. 11, pp. 2–15, 2019, ISSN: 23526483. DOI: 10.1016/j.smhl.2018.09.001. [Online]. Available: http://dx.doi.org/10.1016/j.smhl.2018.09.001.

[76] J. Ottenbacher, M. Kirst, L. Jatobá, M. Huflejt, U. Großmann, and W. Stork, "Reliable motion artifact detection for ECG monitoring systems with dry electrodes," in *Proceedings of the 30th Annual International Conference of the IEEE Engineering in Medicine and Biology Society, EMBS'08 - "Personalized Healthcare through Technology"*, 2008, ISBN: 9781424418152. DOI: 10.1109/iembs.2008.4649502.

[77] N. Van Helleputte, Sunyoung Kim, Hyejung Kim, Jong Pal Kim, C. Van Hoof, and R. F. Yazicioglu, "A 160 ¡formula formulatype="inline"¿¡tex Notation="TeX"¿${A}$¡/tex¿¡/formula¿ Biopotential Acquisition IC With Fully Integrated IA and Motion Artifact Suppression," *IEEE Transactions on Biomedical Circuits and Systems*, vol. 6, no. 6, pp. 552–561, Dec. 2012, ISSN: 1932-4545. DOI: 10.1109/TBCAS.2012.2224113. [Online]. Available: http://ieeexplore.ieee.org/document/6384827/.

[78] Yong Gyu Lim, Gih Sung Chung, and Kwang Suk Park, "Capacitive driven-right-leg grounding in Indirect-contact ECG measurement," in *2010 Annual International Conference of the IEEE Engineering in Medicine and Biology*, IEEE, Aug. 2010, pp. 1250–1253, ISBN: 978-1-4244-4123-5. DOI: 10.1109/IEMBS.2010.5626424. [Online]. Available: http://ieeexplore.ieee.org/document/5626424/.

[79] M. Guermandi, E. F. Scarselli, and R. Guerrieri, "A Driving Right Leg Circuit (DgRL) for Improved Common Mode Rejection in Bio-Potential Acquisition Systems," *IEEE Transactions on Biomedical Circuits and Systems*, vol. 10, no. 2, pp. 507–517, 2016, ISSN: 19324545. DOI: 10.1109/TBCAS.2015.2446753.

[80] J.-M. Redoute and M. Steyaert, "An instrumentation amplifier input circuit with a high immunity to EMI," in *2008 International Symposium on Electromagnetic Compatibility - EMC Europe*, IEEE, Sep. 2008, pp. 1–6, ISBN: 9781424427376. DOI: 10.1109/EMCEUROPE.2008.4786901. [Online]. Available: http://ieeexplore.ieee.org/document/4786901/.

[81] H. Chandrakumar and D. Markovic, "An 80-mVpp Linear-Input Range, 1.6-GΩ Input Impedance, Low-Power Chopper Amplifier for Closed-Loop Neural Recording That Is Tolerant to 650-mVpp Common-Mode Interference," *IEEE Journal of Solid-State Circuits*, vol. 52, no. 11, pp. 1–18, 2017, ISSN: 0018-9200. DOI: 10.1109/JSSC.2017.2753824. [Online]. Available: http://ieeexplore.ieee.org/document/8068941/.

[82] S. Niu, S. Wang, L. Lin, *et al.*, "Theoretical study of contact-mode triboelectric nanogenerators as an effective power source," *Energy and Environmental Science*, vol. 6, no. 12, pp. 3576–3583, 2013, ISSN: 17545692. DOI: 10.1039/c3ee42571a.

[83] R. Hinchet, A. Ghaffarinejad, Y. Lu, J. Y. Hasani, S.-W. Kim, and P. Basset, "Understanding and modeling of triboelectric-electret nanogenerator," *Nano Energy*, vol. 47, no. January, pp. 401–409, May 2018, ISSN: 22112855. DOI: 10.1016/j.nanoen.2018.02.030. [Online]. Available: https://linkinghub.elsevier.com/retrieve/pii/S2211285518300983.

[84] C. Pailler-Mattei and H. Zahouani, "Analysis of adhesive behaviour of human skin in vivo by an indentation test," *Tribology International*, vol. 39, no. 1, pp. 12–21, 2006.

[85] M. Kwiatkowska, S. Franklin, C. Hendriks, and K. Kwiatkowski, "Friction and deformation behaviour of human skin," *Wear*, vol. 267, no. 5-8, pp. 1264–1273, 2009.

[86] D. Djekic, M. Ortmanns, G. Fantner, and J. Anders, "A tunable, robust pseudo-resistor with enhanced linearity for scanning ion-conductance microscopy," *Proceedings - IEEE International Symposium on Circuits and Systems*, vol. 2016-July, pp. 842–845, 2016, ISSN: 02714310. DOI: 10.1109/ISCAS.2016.7527372.

[87] S. Zhang, X. Zhou, and Q. Li, "A Voltage Swing Robust Pseudo-Resistor Structure for Biomedical Front-end Amplifier," *2018 IEEE Asia Pacific Conference on Circuits and Systems, APCCAS 2018*, pp. 61–64, 2019. DOI: 10.1109/APCCAS.2018.8605717.

[88] M. T. Shiue, K. W. Yao, and C. S. A. Gong, "A bandwidth-tunable bioamplifier with voltage-controlled symmetric pseudo-resistors," *Microelectronics Journal*, vol. 46, no. 6, pp. 472–481, 2015, ISSN: 00262692. DOI: 10.1016/j.mejo.2015.03.013. [Online]. Available: http://dx.doi.org/10.1016/j.mejo.2015.03.013.

[89] R. Camós-Vidal and J. Rosell-Ferrer, "Ultra-high input impedance buffer for dry or capacitive electrodes: Design and characterization for industry," *IEEE access*, 2023.

[90] J. Lee, G.-H. Lee, H. Kim, and S. Cho, "An ultra-high input impedance analog front end using self-calibrated positive feedback," *IEEE Journal of Solid-State Circuits*, vol. 53, no. 8, pp. 2252–2262, 2018.

[91] C. Pochet, H. Jiang, and D. A. Hall, "Ultra-Low Leakage ESD Protection Achieving 10.5 fA Leakage," in *2021 IEEE International Symposium on Circuits and Systems (ISCAS)*, vol. 2021-May, IEEE, May 2021, pp. 1–5, ISBN: 978-1-7281-9201-7. DOI: 10.1109/ISCAS51556.2021.9401369. [Online]. Available: https://ieeexplore.ieee.org/document/9401369/.

[92] R. Gan, L. Lyu, G. Mu, and C.-J. R. Shi, "A Neural Recording Analog Front-End with Exponentially Tunable Pseudo Resistors and On-Chip Digital Frequency Calibration Loop Achieving 3.4% Deviation of High-Pass Cutoff Frequency in 5-to-500 Hz Range," in *2022 IEEE Custom Integrated Circuits Conference (CICC)*, vol. 2022-April, IEEE, Apr. 2022, pp. 1–2, ISBN: 978-1-6654-0756-4. DOI: 10.1109/CICC53496.2022.9772872. [Online]. Available: https://ieeexplore.ieee.org/document/9772872/.

[93] Y. Hao, M. Chen, W. Chen, Y. Zhao, and Y. Li, "An Active Electrode for Vital Signal Acquisition With Accurately-Tunable Sub-Hz High-Pass-Corner Frequency and 164-mVpp Linear-Input-Range," *IEEE Transactions on Circuits and Systems II: Express Briefs*, vol. 68, no. 5, pp. 1610–1614, May 2021, ISSN: 1549-7747. DOI: 10.1109/TCSII.2021.3065973. [Online]. Available: https://ieeexplore.ieee.org/document/9378812/.